

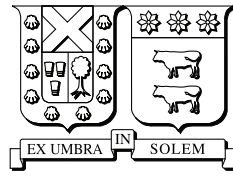
2021-01

HIGH VOLTAGE RATIO STEP-UP CONVERTERS FOR PHOTOVOLTAIC MICROINVERTERS

LOPEZ CAIZA, DIANA CAROLINA

<https://hdl.handle.net/11673/53386>

Repositorio Digital USM, UNIVERSIDAD TECNICA FEDERICO SANTA MARIA



UNIVERSIDAD TECNICA
FEDERICO SANTA MARIA

High Voltage Ratio Step-up Converters for Photovoltaic Microinverters

Tesis de Grado presentada por
Diana Carolina López Caiza
como requisito parcial para optar al grado de
Doctora en Ingeniería Electrónica

Profesor Guía
Dr. Samir Kouro Renaer

Valparaíso, Enero 2021

*Dedicado a las mujeres de mi familia: a mi abueli Luz, a mi madre Mercedes y a mi
hermana Sofía.*

AGRADECIMIENTOS

A través de estas líneas quiero agradecer a todas las personas que estuvieron durante todo este loco proceso, no solo en el interminable camino de la tesis sino también en el cambio de país.

Quiero partir con los agradecimientos a mi familia. A mis padres por mostrarme que todo se puede lograr con trabajo y esfuerzo, y a mi hermana por apoyarme en todo momento. Aunque estuvimos mucho tiempo separados, siempre sentí su cariño.

Es importante mencionar a quien confió en mí desde el primer día, y no solo fue mi supervisor de tesis, sino también un gran amigo. Gracias profesor Samir por creer en mí, por compartir conmigo todos sus conocimientos y experiencias durante este proceso, y por toda la motivación entregada. Además, quiero agradecer al profesor Marcelo por abrirme el espacio y por la confianza depositada en mí. Realmente, me siento muy afortunada por la tremenda oportunidad que tuve; trabajar y aprender junto a estas grandes personas y profesionales, cuya dedicación por llevar los conocimientos y capacidades de los estudiantes más allá de las salas de clases es enorme.

Muchas personas fueron importantes en varias etapas de este proceso, que estuvo marcado por una gran evolución personal y profesional. Nombrarlas a todas sería muy complicado, pero es necesario mencionar y agradecer a varias que estuvieron junto a mí. A Nicolás Müller por ser mi familia en Chile y por todos los consejos tan acertados en cada momento de este proceso. A Miguel López, Gonzalo Carrasco y Christian Rojas por compartir conmigo un poco de su gran pasión por la Electrónica. A Víctor Santana, Rodrigo Lanas, Matías Aguirre, Carolina Fuentes, Hugues Renaudineau y Williams Flores por toda la ayuda, apoyo y las innumerables conversaciones. A Víctor Narváez por continuar con nuestra amistad a pesar de la distancia. Y a mis grandes amigas Marcela y Marysol, con quienes comparto una gran pasión por la escalada, las locuras y las risas.

Finalmente, quiero agradecer a la Comisión Nacional de Investigación Científica y Tecnológica (CONICYT-PCHA/Doctorado Nacional/2018- 21181781) y a la Universidad Técnica Federico Santa María por el financiamiento otorgado durante el Doctorado.

Diana López Caiza.

ABSTRACT

The use of fossil fuels, such as coal, oil and gas, has caused considerable climate degradation. This has made that clean energy sources play an important role in the world's energy portfolio, where the photovoltaic (PV) technology has emerged as a reliable solution in the industrial and small scale applications.

Photovoltaic microinverters are being increasingly used in small-scale PV applications, particularly in houses, buildings and commercial facilities, where occur some obstructions due to different orientations of the structures, leaf, cloudy days, and close objects, which impact on the power generation of the panel. Moreover, this is, probably, one of the most competitive PV market segments where tens of companies develop and manufacture microinverters.

The main advantage of the PV microinverter configuration is that the tracking of the maximum power point is individual for each PV panel, reducing the partial shading, module mismatch and the impact of the orientation. Nevertheless, the efficiency is lower compared to other PV configurations due to a high voltage effort is necessary to connect a PV module into the grid, which is usually achieved by two-stage converter. A high frequency isolated DC-DC converter followed by an unfolding inverter is one of the most used concepts in the market.

On the other hand, during the last year, the single-stage topologies have been proposed in the literature, since only one power conversion stage is required to extract the maximum power of the PV module and inject the AC power into the grid, which could improve the efficiency of PV microinverter configuration. But, the main challenge of these topologies is their control because all variables of the converter are composed by AC waveform and DC-bias.

Therefore, the goal of this thesis is to analyze and develop three non-linear control strategies to regulate the single-stage topologies and evaluate the best alternative. These strategies are Finite Control Set-Model Predictive Control, flatness-based control and sliding mode control, which have been validated through simulations for a typical single-stage topology with differential connection. Based on the three non-linear control methods analysis, it will be selected one of them to validate through experimental tests.

Keywords: photovoltaic energy, PV microinverters, single-stage topologies, Finite Control Set-Model Predictive Control, flatness-based control, sliding mode control.

RESUMEN

El uso de combustibles fósiles, como el carbón, el petróleo y el gas, ha provocado una considerable degradación del clima. Esto ha hecho que las fuentes de energía limpia jueguen un papel importante en la cartera energética mundial, donde la tecnología fotovoltaica ha surgido como una solución confiable en aplicaciones industriales y de pequeña escala.

Los microinversores fotovoltaicos se utilizan cada vez más en aplicaciones fotovoltaicas a pequeña escala, particularmente en casas, edificios e instalaciones comerciales, donde varias obstrucciones ocurren debido a las diferentes orientaciones de las estructuras, hojas, días nublados y objetos cercanos que impactan en la generación de energía del panel. Además, este es quizás uno de los segmentos del mercado fotovoltaico más competitivos donde decenas de empresas desarrollan y fabrican microinversores.

La principal ventaja de la configuración microinversora es que el seguimiento del punto de máxima potencia es individual para cada panel fotovoltaico, lo que reduce el sombreado parcial, el desajuste del módulo y el impacto de la orientación. Sin embargo, la eficiencia es baja en comparación con las otras configuraciones fotovoltaicas debido a que el rango de elevación de voltaje para conectar un módulo fotovoltaico a red es alto, generalmente logrado por un convertidor de dos etapas. Uno de los conceptos más utilizados en el mercado consiste en un convertidor DC-DC aislado de alta frecuencia seguido de un inversor unfolding.

Por otra parte, las topologías de una etapa se han propuesto en la literatura en los últimos años debido a que solo se requiere una etapa de conversión de energía para extraer la potencia máxima del módulo fotovoltaico e inyectar energía alterna a la red, los cuales podrían mejorar la eficiencia de la configuración microinversora. Pero, el principal desafío de estas topologías es su control porque todas las variables del convertidor están compuestas por una componente AC y otra DC. Por lo tanto, el enfoque de esta tesis es analizar y desarrollar tres estrategias de control no lineales para regular las topologías de una etapa y evaluar la mejor alternativa. Estas estrategias son: control predictivo, control basado en la planitud y control en modo deslizante, que se han validado mediante simulaciones para una topología típica de una sola etapa de conversión con conexión diferencial. A partir del análisis de los tres métodos de control no lineales, se determinará la mejor alternativa para ser validada mediante pruebas experimentales.

Palabras claves: energía fotovoltaica, microinversores, topologías de una sola etapa, control predictivo, control basado en planitud, control en modo deslizante.

CONTENTS

Agradecimientos	v
Abstract	vii
Resumen	viii
Contents	ix
List of Figures	xii
List of Tables	xvi
Acronyms	xvii
1 INTRODUCTION	1
1.1 Overview of photovoltaic energy	1
1.2 Overview of grid-connected PV system	2
1.2.1 PV Configurations	3
1.2.1.1 Centralized configuration	3
1.2.1.2 Multi-String configuration	3
1.2.1.3 String configuration	3
1.2.1.4 Microinverter configuration	5
1.3 Microinverter context	5
1.4 Motivation	7
1.5 Goals and contribution of the thesis	8
1.6 Outline of the thesis	9
2 MICROINVERTER TOPOLOGIES	11
2.1 Single-stage topologies	12
2.1.1 Differential mode connection	12
2.1.1.1 Non-isolated single-stage converters	13
2.1.1.2 Isolated single-stage converters	14
2.1.2 Bypass mode connection	15
2.2 Two-stage topologies	17
2.2.1 Unfolding inverter	17
	ix

2.2.1.1	Unfolding inverter with non-isolated DC-DC converters	18
2.2.1.2	Unfolding inverter with isolated DC-DC converters	18
2.2.2	High switching frequency inverter topologies	21
2.2.2.1	High switching frequency inverter with non-isolated DC-DC converters	21
2.2.2.2	High switching frequency inverter with isolated DC-DC con- verters	23
2.3	Multi-stage topologies	25
2.3.1	Summary and discussion	27
3	CONTROL TECHNIQUES FOR DBI	30
3.1	Overview of control techniques for DBI.....	30
3.1.1	Description and model of dual boost inverter	33
3.2	Linear control for DBI.....	37
3.2.1	Maximum power point algorithm	37
3.2.2	Control of the input capacitor energy	38
3.2.3	Output voltage reference calculation.....	39
3.2.4	Control of each boost converter	41
3.2.5	Simulation results of the linear control for DBI.....	42
3.2.6	Discussion.....	47
3.3	Control strategy based on Finite Control Set-Model Predictive Control for DBI	48
3.3.1	Control of the input capacitor energy	48
3.3.2	FCS-Model Predictive Control for DBI	49
3.3.2.1	Predictive model of DBI	49
3.3.2.2	Algorithm of FCS-Model Predictive Control for DBI	50
3.3.2.3	Optimization algorithm	52
3.3.3	Simulation results of FCS-MPC for DBI.....	53
3.3.4	Discussion.....	58
3.4	Flatness-based control for DBI.....	60
3.4.1	Output voltage reference calculation.....	61
3.4.2	Flatness-based control of the individual DC-DC converter.....	61
3.4.3	Simulation results of the flatness-based control for DBI	63
3.4.4	Discussion.....	69
3.5	Sliding mode based control for DBI	70
3.5.1	Control of the boost current	73
3.5.1.1	Sliding surface selection	74
3.5.1.2	Equivalent control	74
3.5.1.3	Existence condition.....	74
3.5.2	Control of the grid current	75
3.5.2.1	Linearization	75
3.5.2.2	Outer control design	77
3.5.3	Simulation results with sliding mode control for DBI	78
3.5.4	Discussion.....	80
3.6	Comparison	85
4	EXPERIMENTAL VALIDATION	94
4.1	Simulation results with fixed input source	95

4.1.1	Steady-state operation in simulation.....	96
4.1.2	Dynamic tests in simulation.....	98
4.2	Experimental setup	103
4.2.1	Power stage.....	103
4.2.2	Control section.....	104
4.3	Experimental results.....	105
4.3.1	Steady-state operation.....	106
4.3.2	Dynamic tests.....	107
4.3.3	Discussion	109
5	CONCLUSIONS	110
5.1	Future work	111
A	PUBLICATIONS DERIVED FROM THIS RESEARCH	113
A.1	Journal publications	113
A.2	Part of book	113
A.3	International conference publications.....	113
	REFERENCES	115

List of Figures

1.1	Solar PV global capacity since 2009 to 2019 [1].	1
1.2	Generic grid-connected PV system.....	2
1.3	Europe solar microinverter and power optimizer market size (MW) by application between 2013 and 2024 [6].....	6
1.4	General structure of the main architectures of PV microinverters topologies: (a) High switching frequency inverter with DC-DC stage, (b) unfolding inverter with DC-DC stage, (c) single-stage differential mode connection, and (d) single-stage bypass mode connection.	7
2.1	Classification of PV microinverter topologies with galvanic isolation and without galvanic isolation.	11
2.2	The generic concept of a single-stage step-up differential mode inverter.	12
2.3	Dual boost inverter topology.....	13
2.4	Dual boost inverter with coupled inductors.....	14
2.5	Dual flyback inverter topology.....	14
2.6	Dual Ćuk inverter topology.	15
2.7	The generic concept of a single-stage step-up bypass mode inverter.	15
2.8	Dual buck-boost inverter topology with bypass connection.....	16
2.9	Dual boost inverter topology with configurable CL filter.	16
2.10	Flyback inverter topology.....	17
2.11	General structure of the unfolding inverter with DC-DC stage.	17
2.12	Topologies of the unfolding inverter with non-isolated DC-DC stage.	19
2.13	Topologies of the unfolding inverter with galvanic isolated DC-DC stage.	20
2.14	General structure of the high switching frequency (HSF) inverter with DC-DC stage.....	21
2.15	High step-up DC-DC converter with coupled inductor.	22
2.16	High step-up DC-DC converter with coupled inductor and intermediate energy storage capacitor.	23
2.17	High step-up DC-DC converter with coupled inductor and HSF inverter.....	23
2.18	Flyback converter with HSF inverter.	23
2.19	Flyback converter and voltage-doubler circuit with active clamp circuit and HSF inverter.	24
2.20	Boost-half bridge DC-DC converter with HSF inverter.....	25
2.21	High step-up converter based on push-pull topology with HSF inverter.	25

2.22	High step-up converter based on resonant full-bridge converter with HSF inverter.	26
2.23	High step-up converter based on full-bridge converter and buck converter in cascaded with unfolding inverter.....	26
3.1	Classification of control strategies for DBI.	32
3.2	Dual boost inverter topology.....	34
3.3	DBI switching states: (a) case 1, (b) case 2, (c) case 3, and (d) case 4.	35
3.4	DBI conduction states when (a.1) $S_1 = 0$, $S_3 = 1$ and $i_s > 0$, (b.1) $S_1 = 0$, $S_3 = 0$ and $i_s > 0$, (c.1) $S_1 = 1$, $S_3 = 1$ and $i_s > 0$, (d.1) $S_1 = 1$, $S_3 = 0$ and $i_s > 0$, (a.2) $S_1 = 0$, $S_3 = 1$ and $i_s < 0$, (b.2) $S_1 = 0$, $S_3 = 0$ and $i_s < 0$, (c.2) $S_1 = 1$, $S_3 = 1$ and $i_s < 0$, and (d.2) $S_1 = 1$, $S_3 = 0$ and $i_s < 0$	36
3.5	Equivalent model of the DBI with grid connection.	36
3.6	Linear control scheme of the grid-connected DBI.	37
3.7	Flow diagram of P&O MPPT algorithm [68].....	38
3.8	Input circuit of the grid-connected DBI.	39
3.9	(a) Equivalent model of the DBI without resistance, and (b) phasor diagram. .	40
3.10	Steady-state results of linear control for DBI at 216 W of PV power: (a) Capacitor voltage of each boost converter, (b) inductor current of each boost converter, and (c) grid voltage and current.	44
3.11	Grid current spectrum of DBI with linear control at 216 W of PV power.....	44
3.12	Steady-state results of linear control for DBI at 150 W of PV power: (a) Capacitor voltage of each boost converter, (b) inductor current of each boost converter, and (c) grid voltage and current.	45
3.13	Grid current spectrum of DBI with linear control at 150 W of PV power.....	45
3.14	Dynamic results of linear control for DBI: (a) PV voltage, (b) PV current, and (c) PV power.....	46
3.15	Dynamic results of linear control for DBI: (a) Capacitor voltages, (b) inductor currents, and (c) grid voltage and current.....	47
3.16	Operating principle of FCS-MPC [71].	48
3.17	The control scheme of the FCS-MPC for the grid-connected DBI.	49
3.18	Flow diagram for the inductor currents, and the capacitor voltages control.	51
3.19	Steady-state results of FCS-Model Predictive Control for DBI at 216 W of PV power: (a) Capacitor voltage of each boost converter, (b) inductor current of each boost converter, and (c) grid voltage and current.	55
3.20	Grid current spectrum of DBI with FCS-Model Predictive Control at 216 W of PV power.....	55
3.21	Steady-state results of FCS-Model Predictive Control for DBI at 150 W of PV power: (a) Capacitor voltage of each boost converter, (b) inductor current of each boost converter, and (c) grid voltage and current.	56
3.22	Grid current spectrum of DBI with FCS-Model Predictive Control at 150 W of PV power.....	56
3.23	Dynamic results of FCS-Model Predictive Control for DBI: (a) PV voltage, (b) PV current, and (c) PV power.	57
3.24	Dynamic results of FCS-Model Predictive Control for DBI: (a) Capacitor voltage of each boost converter, (b) inductor current of each boost converter, and (c) grid current and voltage.....	58
3.25	General concept of flatness system by Levine [77].....	60

3.26	Control scheme of the flatness-based control for DBI.	61
3.27	Control scheme of flatness-based control for boost converter 1.	63
3.28	Steady-state results of flatness-based control for DBI at 216 W of PV power: (a) Capacitor voltage of each boost converter, (b) inductor current of each boost converter, and (c) grid voltage and current.	65
3.29	Grid current spectrum of DBI with flatness-based control at 216 W of PV power.	65
3.30	Steady-state results of flatness-based control for DBI at 150 W of PV power: (a) Capacitor voltage of each boost converter, (b) inductor current of each boost converter, and (c) grid voltage and current.	66
3.31	Grid current spectrum of DBI with flatness-based control at 150 W of PV power.	66
3.32	Simulations results of the tracking of the capacitor voltages with flatness-based control for DBI at 216 W of PV power: a) Capacitor voltage of the boost converter 1, and b) capacitor voltage of the boost converter 2.	67
3.33	Dynamic results of flatness-based control for DBI: (a) PV voltage, (b) PV current, and (c) PV power.	68
3.34	Dynamic results of flatness-based control for DBI: (a) Capacitor voltage of each boost converter, (b) inductor current of each boost converter, and (c) grid current and voltage.	69
3.35	(a) Eigenvalues of substructure I, (b) eigenvalues of substructure II, and (c) sliding mode behaviour [80].	70
3.36	General diagram of sliding mode control [82].	71
3.37	Dual boost inverter topology with other considerations.	72
3.38	Equivalent model of the DBI with grid connection (global control).	73
3.39	The cascaded control scheme of the grid-connected DBI, with external PR controller and internal sliding mode controller.	73
3.40	Bode diagrams of the plant and phase compensator.	77
3.41	Bode diagrams of closed-loop without and with the phase compensator.	78
3.42	Steady-state results of sliding mode control for DBI at 216 W of PV power: (a) Capacitor voltage of each boost converter, (b) inductor current of each boost converter, and (c) grid voltage and current.	81
3.43	Grid current spectrum of DBI with sliding mode control at 216 W of PV power.	81
3.44	Steady-state results of sliding mode control for DBI at 150 W of PV power: (a) Capacitor voltage of each boost converter, (b) inductor current of each boost converter, and (c) grid voltage and current.	82
3.45	Grid current spectrum of DBI with sliding mode control at 150 W of PV power.	82
3.46	Dynamic results of sliding mode control for DBI: (a) PV voltage, (b) PV cur- rent, and (c) PV power.	83
3.47	Dynamic results of sliding mode control for DBI: (a) Capacitor voltages, (b) inductor currents, (c) control signals, (d) measurement and reference of grid current, and (e) grid current and voltage.	84
3.48	The four diagram control of the DBI: (a) Linear control, (b) FCS-MPC, (c) flatness-based control, and (d) sliding mode control.	86
3.49	Capacitor voltages with: (a) Linear control, (b) FCS-Model Predictive Control, (c) flatness-based control, and (d) sliding mode control.	88
3.50	Inductor currents with: (a) Linear control, (b) FCS-Model Predictive Control, (c) flatness-based control, and (d) sliding mode control.	89
3.51	Zoom of the inductor currents of the DBI with FCS-Model Predictive Control.	90

3.52	Grid current spectrum of DBI at nominal power with: (a) Linear control, (b) FCS-Model Predictive Control, (c) flatness-based control, and (d) sliding mode control.	92
4.1	Dual boost inverter topology with 70 V input.	96
4.2	The cascaded control scheme of the grid-connected DBI with 70 V input.	96
4.3	Bode diagrams: (a) plant and phase compensator, (b) closed-loop without and with the phase compensator of the DBI with 70 V input.	97
4.4	Simulation results: Grid current spectrum of sliding mode control for DBI with 70 V input.	98
4.5	Simulations results of sliding mode control for DBI with 70 V input: a) Capacitor voltages, b) inductor currents, c) control signals, and d) grid current and voltage.	99
4.6	Dynamic simulation results of sliding mode control for DBI with 70 V input under variations in the grid current reference: a) Capacitor voltages, b) inductor currents, c) control signals, d) reference and measurement of grid current, and e) grid current and voltage.	101
4.7	Dynamic simulation results of sliding mode control for DBI with 70 V input under grid perturbation: a) Capacitor voltages, b) inductor currents, c) control signals, d) reference and measurement of grid current, and e) grid current and voltage.	102
4.8	Experimental diagram of dual boost inverter.	103
4.9	Analog circuit for control stage, where $R = 20 \text{ k}\Omega$, $R_1 = 10 \text{ k}\Omega$, $V_{CC1} = 2.5 \text{ V}$, $V_{CC2} = 5 \text{ V}$ and $C_1 = 0.1 \text{ }\mu\text{F}$	106
4.10	Experimental results with grid connection and input voltage of 70 V: (a) reference and measurement of grid current, difference of the inductor currents and output of outer control loop (k_2), (b) voltage of the capacitors (v_{c1} , v_{c2}) and current through the inductors (i_{L1} , i_{L2}), (c) voltage of the capacitors (v_{c1} , v_{c2}), voltage of the line filter, output voltage (v_o) and (d) v_{c1} , i_{L1} , grid voltage and current.	107
4.11	Grid current spectrum with 70 V of input voltage.	108
4.12	Experimental results under variations in the output current reference (voltage of the capacitor C_1 (v_{c1}), current through the inductor L_1 (i_{L1}), reference (i_s^*) and measurement (i_s) of grid current): (a) Step-down in the output current reference, and (b) Step-up in the output current reference.	108
4.13	Experimental dynamic performance under grid perturbation (from 20 % voltage dip to nominal voltage): voltage of the capacitor C_1 (v_{c1}), current through the inductor L_1 (i_{L1}), measurement of grid current (i_s), and grid voltage (v_s)...	109

List of Tables

1.1	Summary of grid-connected PV configurations.	4
1.2	Examples of microinverters.....	10
2.1	Summary of the microinverter topologies.....	29
3.1	Summary of the control strategies for the DBI.	31
3.2	Review of the independent control strategies for the dual boost inverter.	33
3.3	Dual boost inverter switching and conduction states.....	34
3.4	Simulation parameters of the linear control of DBI.....	43
3.5	Simulation parameters of the FCS-Model Predictive Control of DBI.	53
3.6	Simulation parameters of the flatness-based control of DBI.	64
3.7	Simulation parameters of the sliding mode control for DBI.	79
3.8	Main parameters of comparison.....	91
3.9	Summary of the control strategies for DBI.....	93
4.1	PV modules with high voltage at maximum power.	95
4.2	Simulation parameters of the sliding mode control for DBI with 70 V input.	98
4.3	Main parameters of the experimental setup.	104
4.4	Main parameters of the sliding mode control strategy.	105
4.5	The main parameters of MicroLabBox.....	105

ACRONYMS

AC	Alternating Current
ADC	Analog-to-Digital Converter
DBI	Dual Boost Inverter
DAC	Digital-to-Analogue Converter
DSP	Digital Signal Processor
DC	Direct Current
DCM	Discontinuous Conduction Mode
FPGA	Field Programmable Gate Array
FCS-MPC	Finite Control Set-Model Predictive Control
HF	High Frequency
HSF	High Switching Frequency
HMI	Human Machine Interface
HPWM	Hybrid Pulse Width Modulation
MPPT	Maximum Power Point Tracking
PV	Photovoltaic
PI	Proportional Integral
PR	Proportional Resonant
PWM	Pulse Width Modulation
SiC	Silicon Carbide
SOGI-PLL	Second Order Generalized Integrator-Phase Locked Loop
SPWM	Sinusoidal Pulse Width Modulation
THD	Total Harmonic Distortion

INTRODUCTION

1.1 Overview of photovoltaic energy

The use of fossil fuels to solve the electricity demand generates an important amount of greenhouse gas emissions, which contributes directly in the climate crisis. To help reduce these emissions, renewable energy sources have emerged as a reliable solution, where solar photovoltaics and wind play a significant role in this energy revolution.

Over the last decade, the solar PV has become the fastest-growing energy, due to decreasing cost of the solar panels and technological advancements together with stable initiatives to incorporate the renewable energies in the power sector. For example, around 115 GW of PV power capacity was added in 2019, as shown in Fig. 1.1 [1].

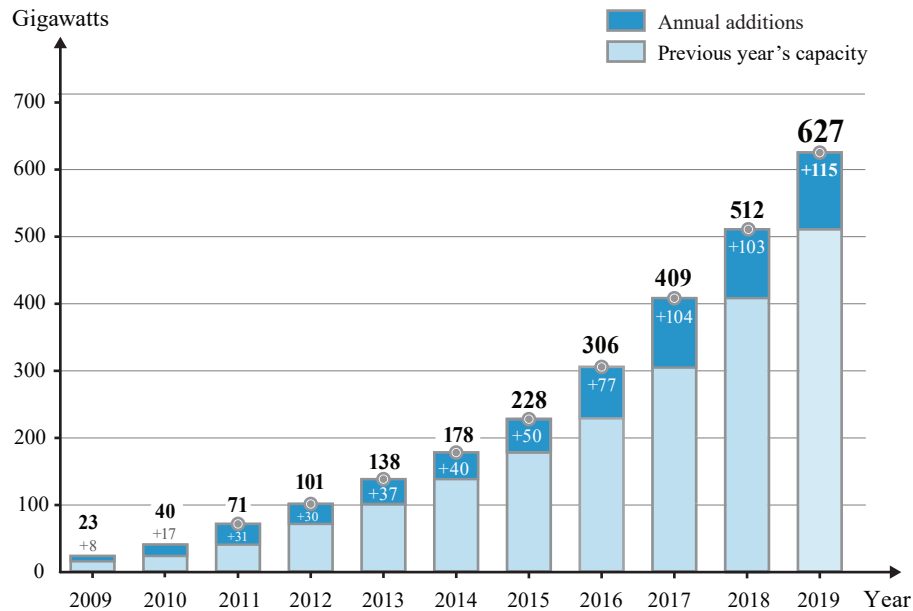


Figure 1.1. Solar PV global capacity since 2009 to 2019 [1].

For electricity generation, the most competitive option in several countries is the solar market. During 2018, eleven countries installed at least one GW of solar photovoltaic capacity. The annual installation in Latin America have presented a fast expansion, because of the solar source is abundance, the number of residential and commercial facilities are increasing, and several industries are investing and installing solar PV plants to energize their activities. Among these industries, the Chilean copper mine industry installed 200 MW of solar PV and wind power capacity in 2018 [2].

1.2 Overview of grid-connected PV system

In order to connect the PV modules into the grid, a PV inverter is used, which extracts the maximum power from the PV system and injects a sinusoidal current into the grid. The generic structure of the grid-connected PV system is shown in Fig. 1.2.

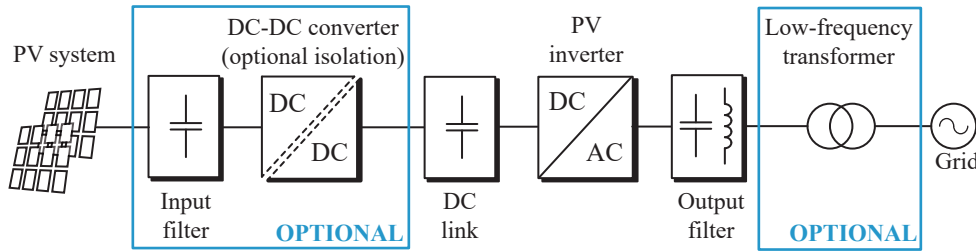


Figure 1.2. Generic grid-connected PV system.

In the PV system, the PV modules can be organized in strings (series connected modules) or in arrays (parallel connected strings), and even a single module can be used.

In most of the cases, the PV system is followed by a passive filter, as a capacitor DC-link, which allows decoupling the input voltage and current from the other stages. Then, a PV inverter is employed to perform the DC-AC conversion from the PV side to the grid. Also, the PV inverter is connected to the grid through an output filter (commonly an inductor, or LC or LCL) to reduce the harmonics.

A DC-DC stage can be integrated in the system, which is used to match the voltage and incorporate the maximum power point tracking (MPPT) of the PV system. In some cases, this stage provides the galvanic isolation through a high-frequency transformer. Also, an input filter (usually a capacitor) is required to fulfill the same function of the DC-link capacitor, which was explained in the previously paragraph. In this case, the DC-link capacitor is used to connect the DC-DC converter with the PV inverter.

Notice that, if the DC-DC converter does not provide isolation, a low-frequency transformer can be employed.

The generic structure presented previously is a basic approach of grid-connected PV systems. However, this structure can change depending on size, power and configuration of the PV plant, and the grid requirements of each country. Therefore, the application establishes different configurations of the PV systems.

1.2.1 PV Configurations

The level of the installed PV power capacity is a factor to define the configuration of grid-connection of the PV systems. These configurations can be divided into four groups, which can be from a single PV module around 200-300 W to a PV plant with more than 500 GW. The main features, advantages and disadvantage of each PV configuration are presented in the next subsections.

1.2.1.1 Centralized configuration

In the 1980s, the first PV plant based on a central configuration was introduced in the grid [3]. This architecture is widely used for large-scale plants (from tenths of a MW installed to unit sizes of 100-1000 kW). The PV modules are connected in strings (PV connected in series), which are connected in parallel through string diodes to achieve the high power level. Then, these groups of the PV modules are connected to the grid through a single inverter, as depicted in Fig. (a) of the Table 1.1.

The central structure is simple, because only one control set is implemented. However, several limitations, such as, the power losses under partial shading or non-uniform conditions due to a single MPPT, the power losses in the string diodes, high voltage DC cables and non-flexible design can be identified [4].

1.2.1.2 Multi-String configuration

The general structure of the multi-string configuration is shown in Fig. (b) of the Table 1.1. Each PV strings is connected to the central inverter through independent DC-DC converter. The main functions of the DC-DC stage are to introduce a separate MPPT for each string, match the input voltage level and provide galvanic isolation.

The introduction of several DC-DC converters is an advantage compared to the centralized configuration, allowing the decouple between the PV systems and the inverter, the integration of different module technologies in the same PV system (flexible design), and the individual control of each string.

Multi-string configuration is popular in small and medium scale PV plants. Nowadays, this configuration has been incorporated in the large scale market.

1.2.1.3 String configuration

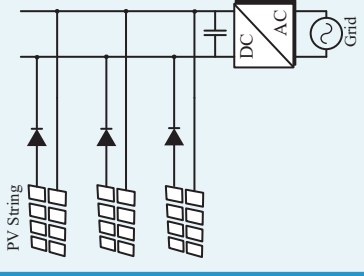
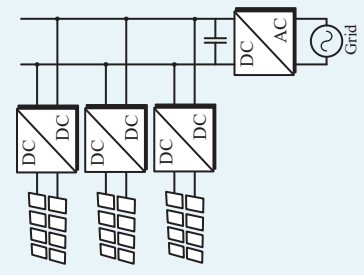
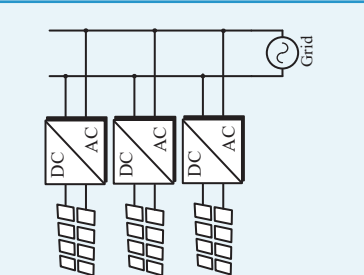
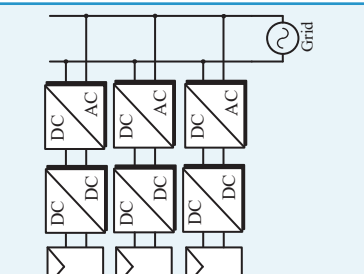
The string configuration is composed by a single series connection (string) of PV modules, which is connected to the grid through an inverter (one-stage). This approach is a reduced version of the centralized configuration with an independent MPPT for each string. The general structure of the string configuration is depicted in Fig. (c) of the Table 1.1.

If the PV string voltage is low, a DC-DC stage can be incorporated in the architecture to increase this voltage for grid-connection. In some countries, DC-DC converter with a high frequency transformer is used to provide the galvanic isolation.

The advantages of this configuration are the elimination of the losses associated with the string diodes and the modular structure due to the individual MPPT.

In addition, the string configuration is widely used for small and medium scale, specially for rooftop applications.

Table 1.1. Summary of grid-connected PV configurations.

	CENTRALIZED	MULTISTRING	STRING	AC-MODULE
Power range	< 1.6 MW	< 500 kW	< 10 kW	< 300 W
Advantages	<ul style="list-style-type: none"> Simple structure Reliable 	<ul style="list-style-type: none"> High MPPT performance Modular/flexible 	<ul style="list-style-type: none"> Modular/flexible Good MPPT performance 	<ul style="list-style-type: none"> Modular/flexible High MPPT performance Easy installation
Disadvantages	<ul style="list-style-type: none"> Blocking diodes Poor MPPT performance Not flexible 	<ul style="list-style-type: none"> More complex (two-stage is mandatory) 	<ul style="list-style-type: none"> High component count 	<ul style="list-style-type: none"> Higher losses Higher cost per watt
Architectures	 <p>(a)</p>	 <p>(b)</p>	 <p>(c)</p>	 <p>(d)</p>

1.2.1.4 Microinverter configuration

In traditional microinverter configuration or AC-module configuration, a single PV module is connected to the grid through a two-stage converter composed by a DC-DC converter and an inverter, as shown in Fig. (d) of the Table 1.1.

The main advantage of the microinverter configuration is that the maximum power point tracking (MPPT) is individual for each module in the PV system, reducing the impact of orientation, partial shading, and module mismatch. However, the power converter efficiency is lower regarding other PV configurations, because a single module to grid connection requires a high voltage step-up effort by the converter, usually achieved by the DC-DC stage with high frequency (HF) isolation [5].

In addition, microinverters have a higher cost per kW compared to other PV system configurations, since the power electronics are distributed among all modules, and each one needs dedicated controllers, sensors, heat sink, housing etc. For that reason, the microinverter configuration is implemented for rooftop applications.

1.3 Microinverter context

The demand for solar energy has expanded rapidly in the last years, which has turned it into the most competitive option in electricity generation. The large-scale projects are the mainstream market which provide important percentage of the annual PV power capacity installed. Also, the residential, commercial, and industrial rooftop solar PV systems are growing in the PV market, as reported in the latest analysis by Global Market Insights Inc, where the global microinverter and power optimizer market was valued at USD 550 million in 2015, and it is expected to exceed USD 1.4 billion by 2024 [6]. For example, the Europe market in 2015 was expanded over 10% regarding last year, as shown in Fig. 1.3. In this figure, it is also possible to observe the expected growth of the residential, commercial and utility market during the forecast period (2016-2024).

Moreover, the favorable government policies for use of renewable energy promote the installation of the solar panels in rooftops. Several countries such as Spain, Indonesia, Romania and Malaysia introduced new incentives programs for small-scale solar energy consumption. An example of this initiative is the rising penetration of rooftop systems in Australia's grid, where around 2 million Australian homes and companies generated their electricity by rooftop solar systems in 2018 [2]. Another example is the U.S microinverter market, which is predicted to grow at 15 % from 2016 to 2024.

In the commercial sector, several companies invest and develop microinverter technologies as Enphase, Hoymiles, ReneSola, Chilicon Power, LeadSolar and others. The main products of these companies are given in Table 1.2.

In the academic literature and in the commercial products, it is possible to identify four main architectures for grid-connection of a single PV panel, as shown in Fig. 1.4. The high switching frequency inverter was the classical solution to implement in the commercial products, which is composed by two stages of power conversion: a DC-DC converter followed by a DC-AC converter, as it can be observed in Fig. 1.4(a). The DC-DC converter elevates the PV voltage to peak voltage of the grid, tracks the maximum power point of the panel, and in some cases provides the galvanic isolation, while the inverter stage injects a sinusoidal current into the grid. This architecture presents a low efficiency due to the power devices of the DC-AC converter which are operated at high frequency.

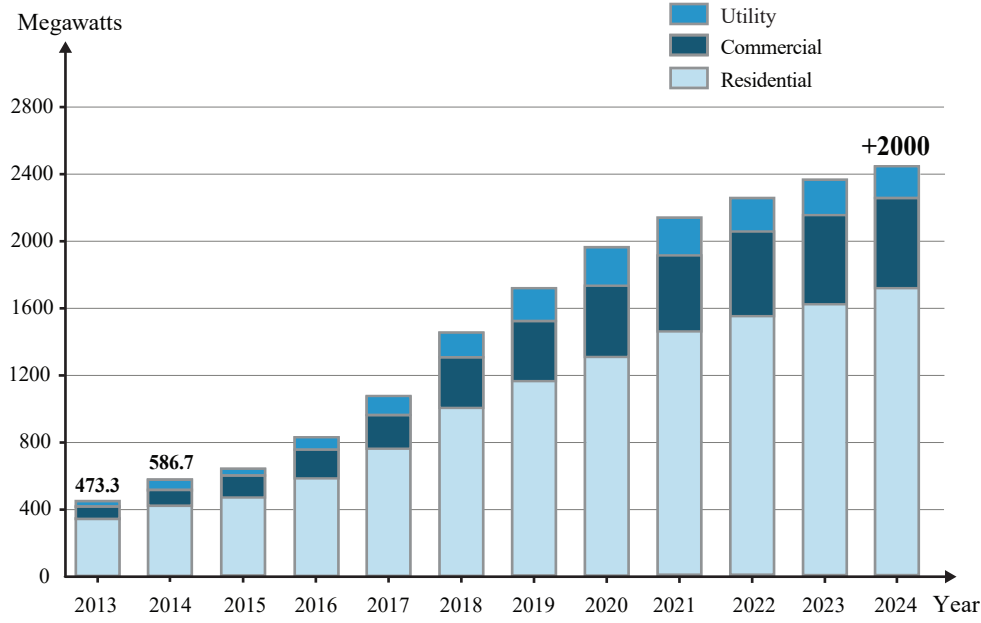


Figure 1.3. Europe solar microinverter and power optimizer market size (MW) by application between 2013 and 2024 [6].

In order to increase the overall efficiency, the unfolding inverter is proposed, its structure is presented in Fig. 1.4(b). This inverter has the same number of the stages that the previous architecture. The DC-DC converter is performing the MPPT (and optional galvanic isolation). The output current is controlled to follow a rectified sinusoidal waveform. Then, the inverter is switching at line frequency to unfold the current into a full sinusoidal waveform. Therefore, a high efficiency can be reached with this solution, because only the semiconductors of the DC-DC converter are switched at high frequency.

In the last years, some researches have focused on single-stage topologies since only one power stage is necessary to perform MPPT and control the grid current. The efficiency could be increased. The most common solution is the differential mode connection of two DC-DC converters, which shared the input source, as seen in Fig. 1.4(c). The output of each DC-DC converter is composed by a sinusoidal waveform and a DC-bias, which is canceled through the differential connection, obtaining only the AC component at the output. However, the efficiency of these converters is not high enough to compete in the microinverter market. In order to solve this, another single-stage architecture is proposed, which are based in bypass mode connection, as illustrated in Fig. 1.4(d). These topologies are also composed by two DC-DC converters, where each converter operates in the half cycle of the line frequency.

The typical solution with differential connection is the dual boost inverter, which is composed by two bidirectional boost converters. In the literature, few studies of efficiency of this inverter are found, where the maximum efficiency achieved in experimental results is around 85 %, as shown in [7]. One alternative to increment the efficiency is to use coupled inductors,

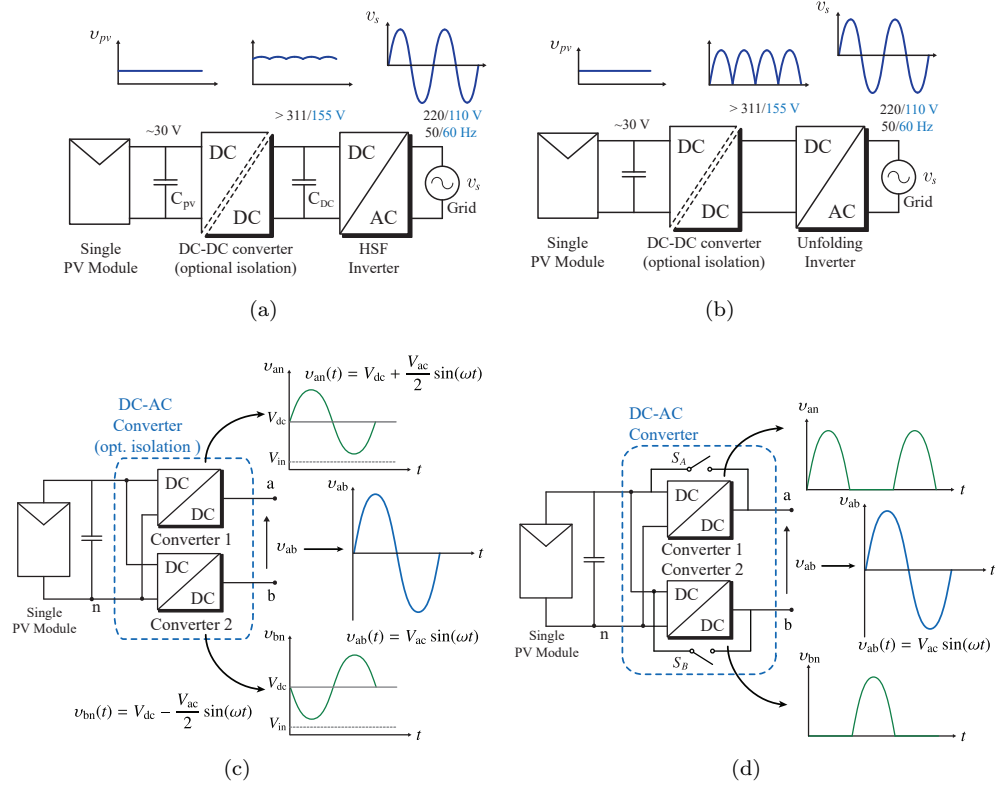


Figure 1.4. General structure of the main architectures of PV microinverter topologies: (a) High switching frequency inverter with DC-DC stage, (b) unfolding inverter with DC-DC stage, (c) single-stage differential mode connection, and (d) single-stage bypass mode connection.

which increases the voltage ratio of the inverter. The efficiency estimated for this topology is 95.6 % in [8]. Also, one work reported that the efficiency with this structure is 97.5 % [9]. On the other hand, the efficiency reported for the inverter in the bypass connection is around 85 %, as shown in [10]. In another work [11], the efficiency of the inverter with configurable filter is 93.82 %. And, the isolation alternative for this architecture presented an efficiency of 89 % [12].

Therefore, it is possible to observe that this technology is still under development considering that new topologies have been proposed to improve the efficiency in the last years. But, a challenge of the differential connection inverters is their control strategies.

1.4 Motivation

As mentioned in the previous section, the high switching frequency inverters were the initial solution to implement in the PV microinverter applications. However, the efficiency is the main disadvantage of these topologies since the DC-AC stage operates at high switching

frequency. The unfolding inverter was proposed to solve this issue. In this case, the power devices of the AC-DC stage are switched at the grid frequency, improving the overall efficiency of the system. The unfolding approach is the mainstream technology used in the available commercial products.

Also, there are several researches about the single-stage topologies. In this case, the efficiency could be improved since the power conversion is achieved in only one stage and it could exhibit potentially fewer losses. However, this technology is in the early stage of development. Despite several progressive improvements have been done in new topologies, the efficiency is still very low.

Nevertheless, the biggest underlying problem for single-stage topologies is not only new circuit with more efficiency, but also restrictions and challenges arise from the control perspectives. In fact, these topologies are very difficult to control, because the operation point of each DC-DC converter presents large variations making the linearization process a difficult task. It is important to note that, each variable of the converter including the duty cycle is composed by DC and AC components. Thus, the main objective of this thesis is to solve the control issues of the single-stage topologies.

The control of the single-stage topologies is a great challenge since the inverter is not a conventional switching converter. In this case, the output of the converter is composed by a sinusoidal waveform with a DC-bias, and then all the variables of the converter have DC and AC components. Therefore, the design parameters used in the cascaded linear control scheme are not easy to apply. Also, the duty cycles of the converters are not regarded to the grid current, which generates an indirect control of the system.

In several works, a cascaded linear control strategy is used to regulate the output sinusoidal voltage of each DC-DC converter in the single-stage topologies. The scheme proposed is composed by an outer control loop for the capacitor voltage and an inner control loop for the inductor current, where proportional-integral controllers are used for both loops. In [7, 13, 14], this control scheme was validated experimentally in a laboratory prototype for a non-linear load. For the grid connection of the inverter, few works with experimental prototype are found in the literature. In these cases, the proportional resonant controllers have been used in the cascaded control loops. In [15] and [16], a set-up transformer is used to achieve the grid connection.

1.5 Goals and contribution of the thesis

The work of this thesis focuses on the study of three non-linear control strategies for the single-stage topologies for PV microinverter configuration.

Three non-linear control strategies are proposed and developed in this research. The first method is based on the predictions of the behavior of the system variables. This technique is known as Finite Control Set-Model Predictive Control. The second method is flatness-based control, which is based on a property of the differential algebra to regulate the system through a flat variable. Finally, sliding mode approach is proposed to connect the inverter into the grid. This approach has already been reported for a single-stage topology, where a voltage control is implemented for the inverter with resistance load, but the grid connection is not presented. Consequently, three goals are proposed:

- The Finite Control Set-Model Predictive control is based on the model of the power converter. Thus, the first objective is to propose a discrete model of the system, considering

the individual control of each DC-DC converter.

- In the flatness-based control, the objective is to analyze and develop a control strategy, which regulates the output voltage of each DC-DC converter through the stored energy in the components of the inverter (inductors and capacitors) and its derivatives.
- In the sliding mode approach, the goal is to develop a current control to regulate the grid current of the inverter and the difference between the current of the inductors.

Finally, the contribution of this research is to determine the most appropriate control strategy for the single-stage architectures, complementing the study and development of new topologies.

1.6 Outline of the thesis

The thesis presents a detailed analysis of the non-linear control strategies for single-stage topologies in PV microinverter configuration. Therefore, the main issues found in the microinverter topologies are described in order to explain the main motivation, goals and contribution of the investigation, which are presented in Chapter 1.






Chapter 2 shows a review of the microinverter topologies found in the academic and industrial field, and a classification of these topologies are proposed, where four main architectures are identified. Also, a short comparison of these architectures is presented at the end of the chapter.

In Chapter 3, the analysis of the three non-linear controls used to regulate a single-stage topology is presented. Simulation results are also shown to validate the proposed strategies. Furthermore, a comparison between the linear control and the three non-linear control methods is performed to determine the control strategy, which will be validated in the experimental prototype.

In order to validate the non-linear proposed control, the experimental results are shown in Chapter 4. Moreover, the discussion about behavior of the converter with the proposed control strategy is also presented.

Finally, the conclusions and comments derived from this research are included in Chapter 5.

Table 1.2. Examples of microinverters.

INPUT DATA (DC)	ENPHASE IQ - 7 MICRO	HOYMILES MI-250/300/350	RENESOLA REPLUS - 240A	CHILICON POWER CP - 250E	LEAD SOLAR Microinverter LS250
	235 - 350 60 cell PV panel 48 15	Up to 310/380/440 60 or 70 cell PV panels 22 10.5/10.5/11.5	250 N. S* 55 14	190 - 355 60 or 70 cell PV panels 47 12	230 - 300 60 or 70 cell PV panels 60 9.7
	208 or 240 60	208 or 240 60	208 or 240 60	208 or 240 60	208 or 240 60
	97.6 %	96.7 %	96.3 %	96.6 %	96.2 %
OUTPUT DATA (AC)	Nominal L-L voltage range (V)	208 or 240	208 or 240	208 or 240	208 or 240
	Nominal frequency (Hz)	60	60	60	60
	Peak efficiency	97.6 %	96.7 %	96.6 %	96.2 %
MECHANICAL DATA	Dimensions (WxHxD) (mm)	175 x 212 x 30.2	178 x 153 x 28	230 x 138 x 35	163 x 163 x 31
	Weight (Kg)	1.08	1.98	2.0	2.0
Microinverter photo	 (a)	 (b)	 (c)	 (d)	 (e)

MICROINVERTER TOPOLOGIES

The AC-module configuration is composed of the DC-AC converter, which connects a PV module to the grid. As mention before, the main advantages are that the maximum power point tracking is implemented for each PV module, reducing the partial shading and module mismatch. Also, other advantage is the modularity, allowing to increase the installed power.

Although the AC-module configuration presents several advantages, the power converter efficiency is the main challenges of this configuration due to it is lower regarding to the other PV configurations. In order to solve this issue, a large amount of topologies have been proposed in the academic and industrial field. Therefore, a detailed review of the existing PV microinverter topologies is provided in this chapter.

A classification of the main PV microinverter topologies found in the literature is proposed in Fig. 2.1. The proposed categorization considers the number of stages of power converters, the types of inverter topologies, and the presence or absence of galvanic isolation in the global architecture.

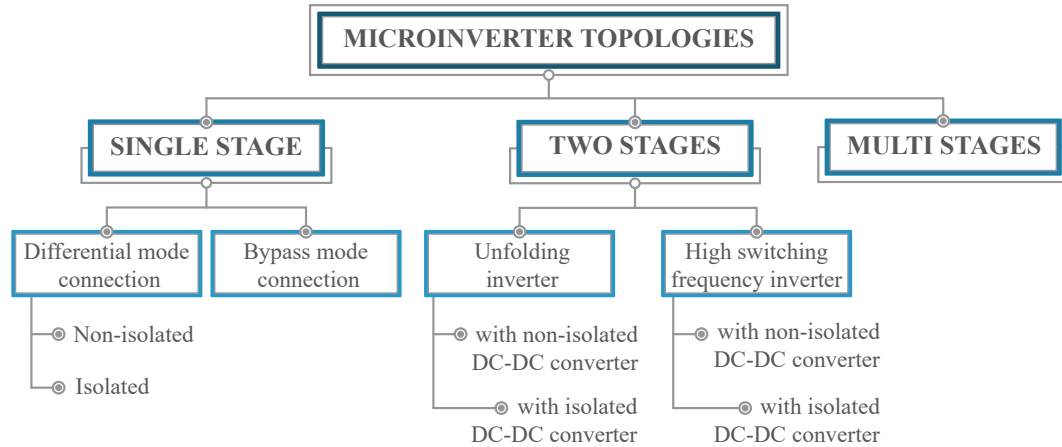


Figure 2.1. Classification of PV microinverter topologies with galvanic isolation and without galvanic isolation.

2.1 Single-stage topologies

In small scale applications, a photovoltaic module is generally connected to the grid through two stages converters. The input voltage is boosted beyond the peak voltage of the grid by the first stage, a DC–DC converter, which is then converted to AC by the second stage, the grid–tie inverter [5]. However, the efficiency of a two-stage conversion system, particularly when a high step-up voltage DC–DC stage is required, is the main disadvantage of such architecture. Size, cost, and reliability are other factors to take into account. In this context, single-stage power converters have been proposed to improve the overall efficiency, by reducing the number of components in the system.

The main challenge of single-stage topologies is to fulfill two functions with a single converter: step-up the input voltage and accomplish the grid connection.

In this section, single-stage PV microinverter topologies based on the differential and bypass mode connection are presented and detailed.

2.1.1 Differential mode connection

The generic concept of voltage step-up single-stage differential inverter is shown in Fig. 2.2. The inverter is composed of two bidirectional DC–DC converters, which share the same input source, while their output voltages are connected in differential mode. Each DC–DC converter presents a sinusoidal output voltage with a DC-bias (V_{DC}), as shown below

$$v_{an}(t) = V_{DC} + \frac{v_{AC}(t)}{2} \quad (2.1.1)$$

$$v_{bn}(t) = V_{DC} - \frac{v_{AC}(t)}{2} \quad (2.1.2)$$

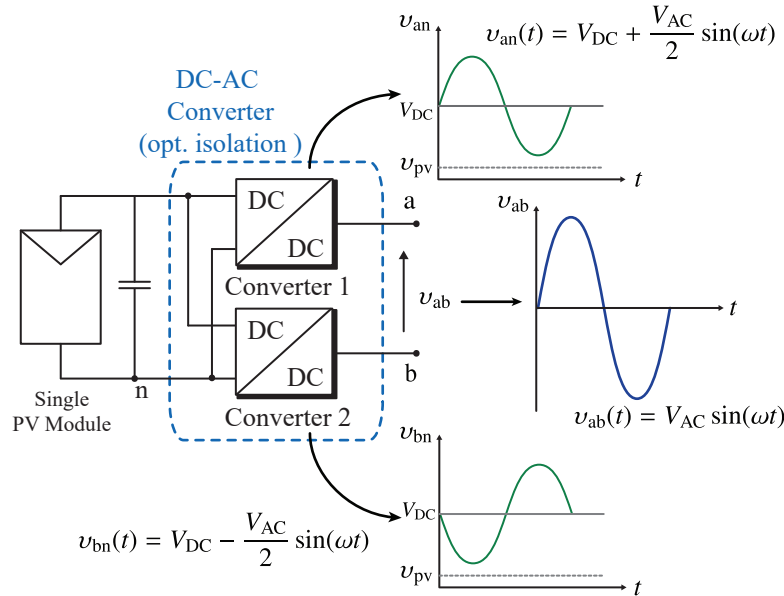


Figure 2.2. The generic concept of a single-stage step-up differential mode inverter.

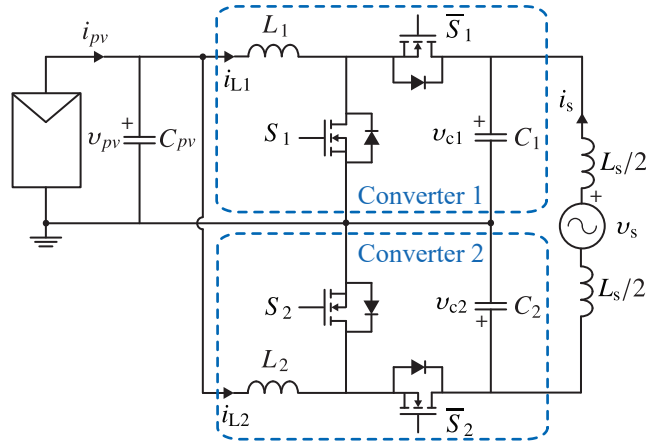


Figure 2.3. Dual boost inverter topology.

The AC component of the output signal of each converter is in the opposite phase regarding the other converter. Thus, considering the same DC component for both converters, the output voltage of the inverter is given by

$$v_{ab}(t) = v_{an}(t) - v_{bn}(t) = V_{AC} \sin(\omega t) \quad (2.1.3)$$

where V_{AC} is the amplitude of the output voltage of the inverter. By generating opposite phase AC signals, the total converter output voltage doubles the individual converter AC amplitude.

In the literature, several bidirectional DC–DC converters have been used, e.g., boost [7, 13–15, 17–19], flyback [20, 21] and ĉuk [22–24]. The bidirectional converters are necessary due to a circulating current is presented between the inductors.

2.1.1.1 Non-isolated single-stage converters

i) Dual boost inverter: One of the most popular topologies in this group is the dual boost inverter (DBI) originally introduced in [17]. The power circuit of the DBI consists of two bidirectional DC–DC boost converters, as shown in Fig. 2.3 for a grid-connected application. Notice that the outputs of the two DC–DC converters are connected to the grid through a symmetrically divided inductive filter L_s .

ii) Dual boost inverter with coupled inductors: One disadvantage of DBI is that a high voltage ratio is not possible to achieve. An interesting solution to solve this issue is employed DC–DC converters with coupled inductors presented in [9] and [8]. The DBI with coupled inductors is shown in Fig. 2.4. The output voltage depends of the duty cycle and number of turns of the coupled inductors.

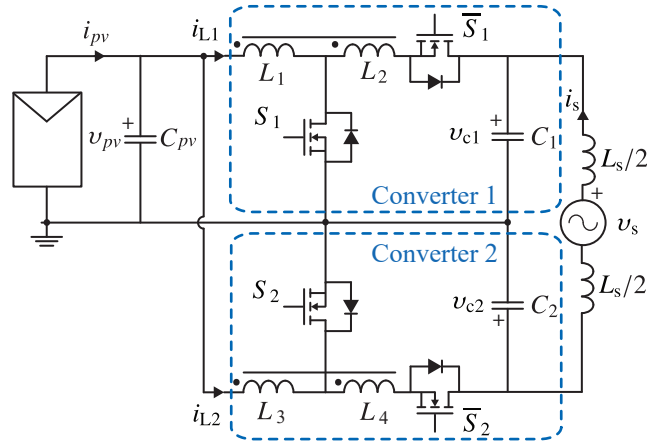


Figure 2.4. Dual boost inverter with coupled inductors.

2.1.1.2 Isolated single-stage converters

i) **Dual flyback inverter:** A single-stage topology with galvanic isolation is presented in Fig. 2.5, which is composed by two bidirectional flyback converters. In [21], a dual flyback inverter of 160 W is simulated. Notice that, four power semiconductors and two high-frequency transformers are necessary to generate the sinusoidal output voltage, which can increase the size of the inverter.

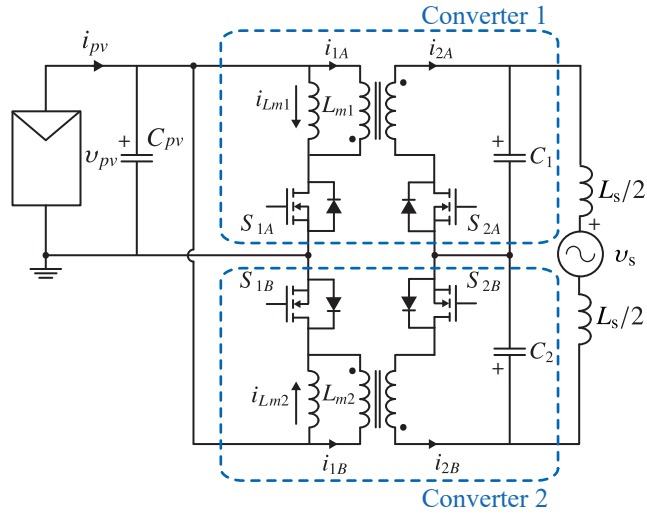


Figure 2.5. Dual flyback inverter topology.

ii) **Dual Ćuk inverter:** The inverter in Fig. 2.6 is composed by two DC-DC isolated Ćuk converters, which was outlined in [22]. The original modulation scheme is based on

continuous switching of semiconductors, which generates the circulating power. Mehrnami and Mazumder proposed a discontinuous modulation scheme for dual Ćuk inverter. In this approach, each DC-DC converter is activated in alternated half of line cycle, as shown in [23] and [24]. The efficiency with the discontinuous modulation scheme improves significantly, because the circulating power is eliminated in the inverter.

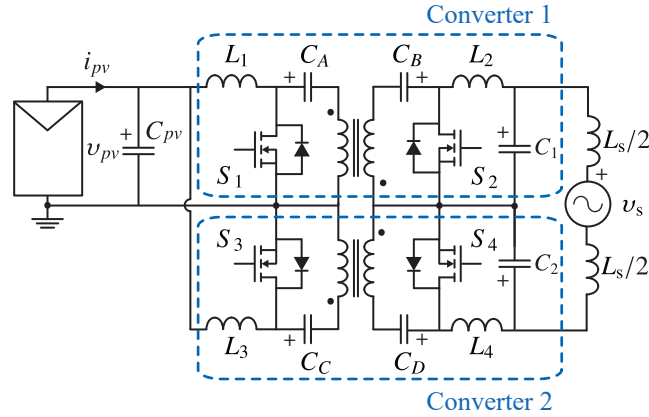


Figure 2.6. Dual Ćuk inverter topology.

2.1.2 Bypass mode connection

The general concept of the single-stage inverter with bypass connection is presented in Fig. 2.7. The power circuit is composed by two DC-DC converters, which are connected in parallel at the input voltage source. Each DC-DC converter is activated in one half cycle of the fundamental grid voltage by the semiconductor devices (S_A and S_B).

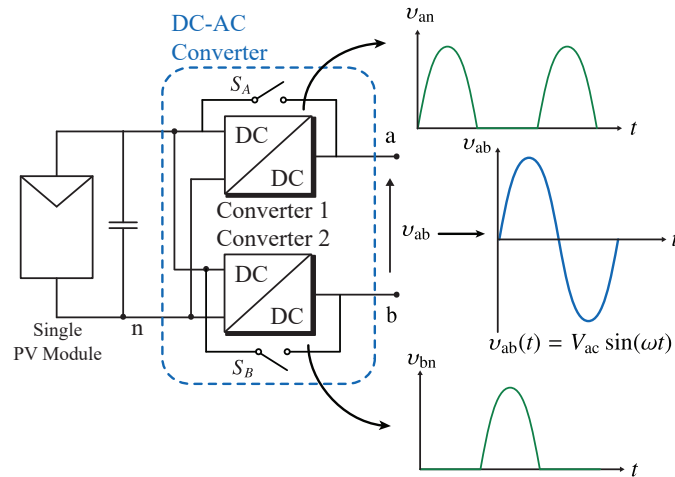


Figure 2.7. The generic concept of a single-stage step-up bypass mode inverter.

One bypass inverter topology has been proposed in [10], which is composed by two buck-boost converters. The topology is shown in Fig. 2.8. The semiconductors S_1 and S_2 are switched at high frequency. During the positive half cycle of the grid voltage, S_1 is turned ON and S_A is kept active. Meanwhile, S_2 is turned ON during the negative half cycle and S_B is kept active. The structure of this proposed topology is simple and symmetrical. Also, the switching and conduction losses are reduced due to only one semiconductor is switched at high frequency in each half cycle. For this reason, the bidirectional DC-DC converter is not necessary.

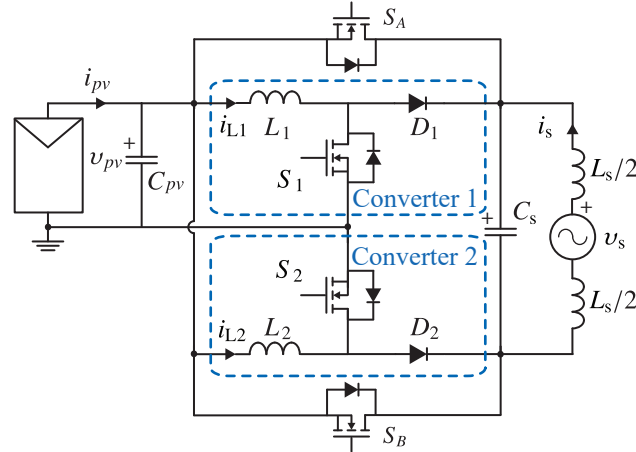


Figure 2.8. Dual buck-boost inverter topology with bypass connection.

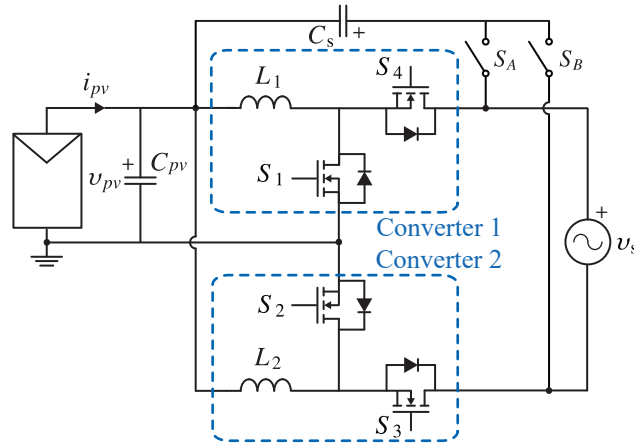


Figure 2.9. Dual boost inverter topology with configurable CL filter.

On the other hand, the bypass mode connection concept is used in [11]. The power circuit includes two buck-boost converters with a configurable CL filter circuit, as shown in Fig. 2.9. The main advantage of this inverter is that the grid inductor is omitted, because in each half

line cycle, one of the converters operates as a buck-boost, while the inductor of the other converter is part of the CL filter.

Another topology derived from the bypass concept is depicted in Fig. 2.10. The flyback inverter is composed by three power devices, two diodes and a transformer with center-tapped secondary winding, as presented in [12, 25, 26]. The main semiconductor S of the flyback inverter is operating at high frequency, which is connected to the primary winding of the transformer. Each secondary winding is activated during the half cycle of the grid frequency through the semiconductor S_A or S_B depending on the grid.

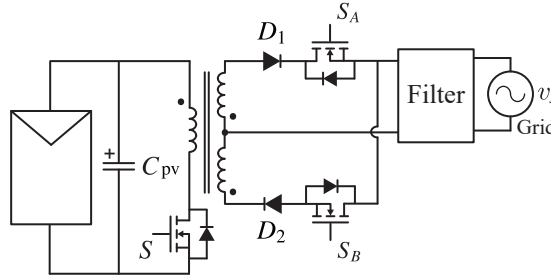


Figure 2.10. Flyback inverter topology.

2.2 Two-stage topologies

2.2.1 Unfolding inverter

Among all the alternatives of the microinverter topologies, one of the most used concepts considers a two-stage approach, as represented in Fig. 2.11. The first stage is a step-up DC-DC converter used for input voltage elevation and performing MPPT, followed by an unfolding inverter for the grid connection.

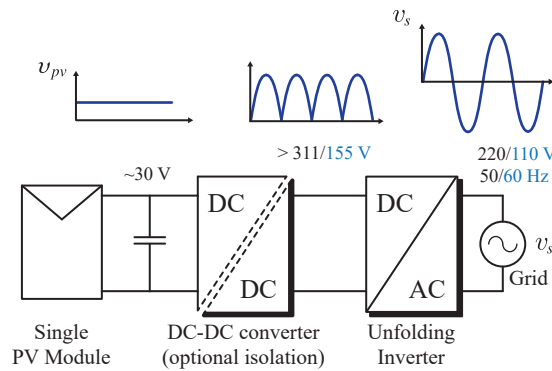


Figure 2.11. General structure of the unfolding inverter with DC-DC stage.

The main feature of these topologies is that the output current of the DC-DC stage is a rectified sinusoidal. Hence, the second stage unfolds the current into an AC waveform. In

this way the DC-link capacitor between the DC-DC and DC-AC stage is not necessary and only the DC-DC stage is operating at high frequency while the inverter stage is switching at fundamental frequency. Therefore, only the conduction losses are presented in the semiconductor devices, which allows the use of other type of semiconductor, as such TRIAC's or IGBT's, improving the efficiency.

For this topology, different DC-DC converters with or without galvanic isolation have been proposed, which are presented in the next subsections.

2.2.1.1 Unfolding inverter with non-isolated DC-DC converters

The topologies of this category are based on a buck-boost converter. Fig. 2.12(a) shows the basic topology, where only one power device is switched at high frequency. Also, the DC-DC converter is operated in discontinuous conduction mode without extra current controller as presented in [27].

In [28], a switched inductor is introduced in the buck-boost converter as shown in Fig. 2.12(b) to increment the gain of the topology.

The DC-DC stage in the topology of Fig. 2.12(c) is composed by a boost and buck converters in cascaded. The inverter operates in buck or boost mode depending on the grid voltage, but it never works in both modes [29,30]. If the input voltage is lower than the grid peak voltage, the inverter changes between buck or boost mode operation in function of the instantaneous grid voltage. However, if the input voltage is higher than the grid peak voltage, the inverter operates in buck mode. The inverter of the aforementioned topologies is an H-bridge, which the power devices operate at the fundamental grid frequency, as shown in Fig. 2.12(e).

On the other hand, several switched capacitor blocks are used in the DC-DC stage to increase the input voltage without magnetic components as shown in Fig. 2.12(d). In [31], the experimental setup presents four switched capacitor blocks, whose inputs and outputs are connected in parallel and series, respectively. The control scheme is based on sinusoidal pulse width modulation (SPWM) due to its ease implementation, but the large number of the power devices is the main disadvantage of this topology.

2.2.1.2 Unfolding inverter with isolated DC-DC converters

This section describes four isolated DC-DC converters, which are used in the unfolding topologies. The most popular converter with galvanic isolation used in the DC-DC stage of these topologies is the flyback converter, because its implementation and control are simple with high efficiency and reliability. In Fig. 2.13(a), the power circuit of the DC-DC flyback converter can be observed, in which a transformer is used to eliminate the electrical connection between the input and the output of the converter. This DC-DC converter together with an H-bridge unfolding inverter for PV microinverter is presented in [32]. In addition, a mainstream commercial topology is composed of two interleaved flyback converters followed by an H-bridge unfolding inverter [33–35]. This solution was adopted by Enphase, which has been a successful product in the market released in 2008 (Enphase M175). The interleaved-flyback converter connected in parallel at the input and output of two flyback converters, as observed in Fig. 2.13(b). The interleaved connection allows to reduce the size of the high-frequency transformer since the power is divided by the number of DC-DC converters, and the input voltage ripple is also reduced.

Another DC-DC isolated converter for PV applications is composed of a PWM inverter

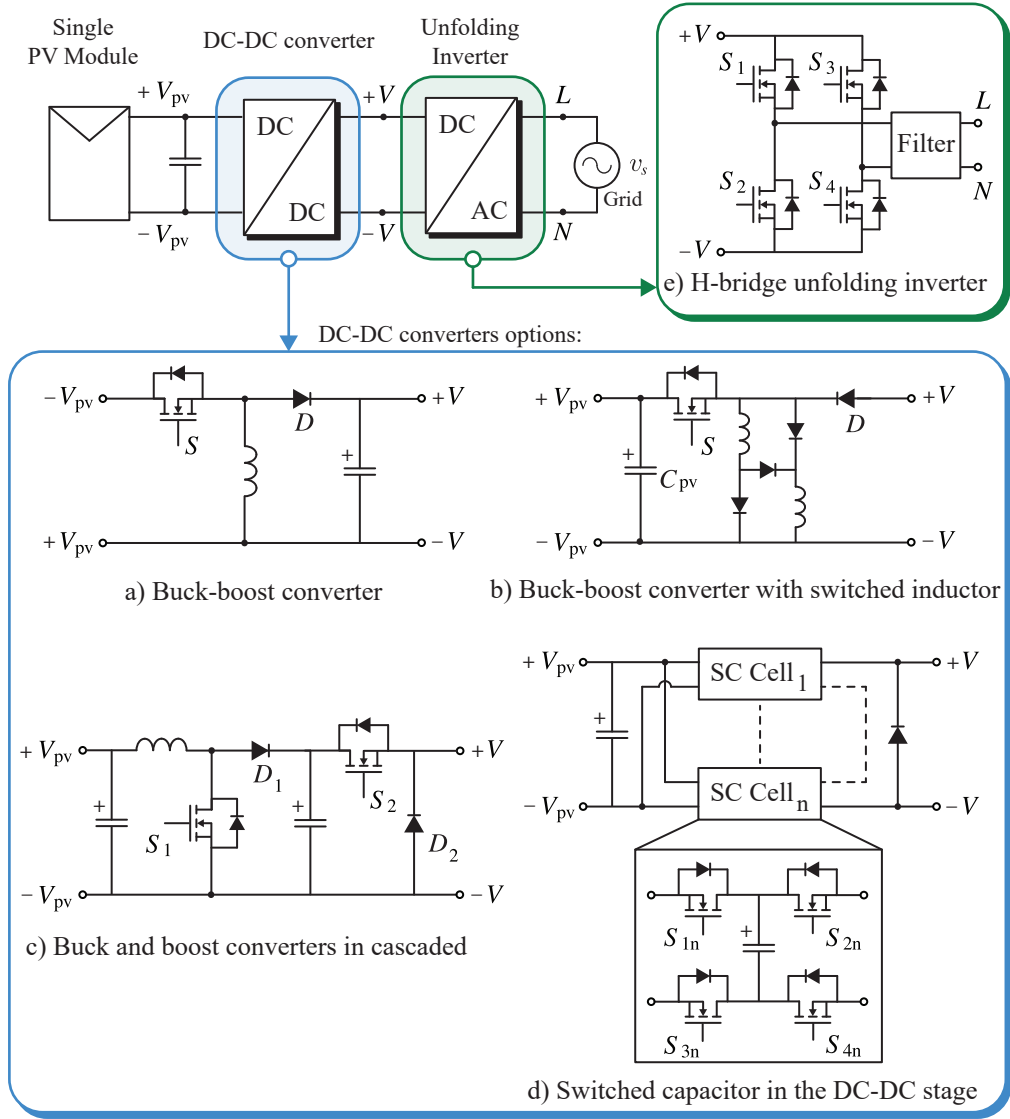


Figure 2.12. Topologies of the unfolding inverter with non-isolated DC-DC stage.

and a full-bridge rectifier. The inverter contains four power devices and a high-frequency transformer, which together with the full-bridge rectifier generates the rectified sinusoidal current [36]. A similar approach is presented in [37] and [38], in which a resonant circuit is introduced in the primary side of the transformer, as shown in Fig. 2.13(c). These DC-DC converters are followed by an H-bridge inverter, whose main function is to unfold the output current, therefore the power devices S_1 and S_4 of Fig. 2.13(e) are turned on during the positive half-cycle of the grid voltage, while S_2 and S_3 remained on during the negative

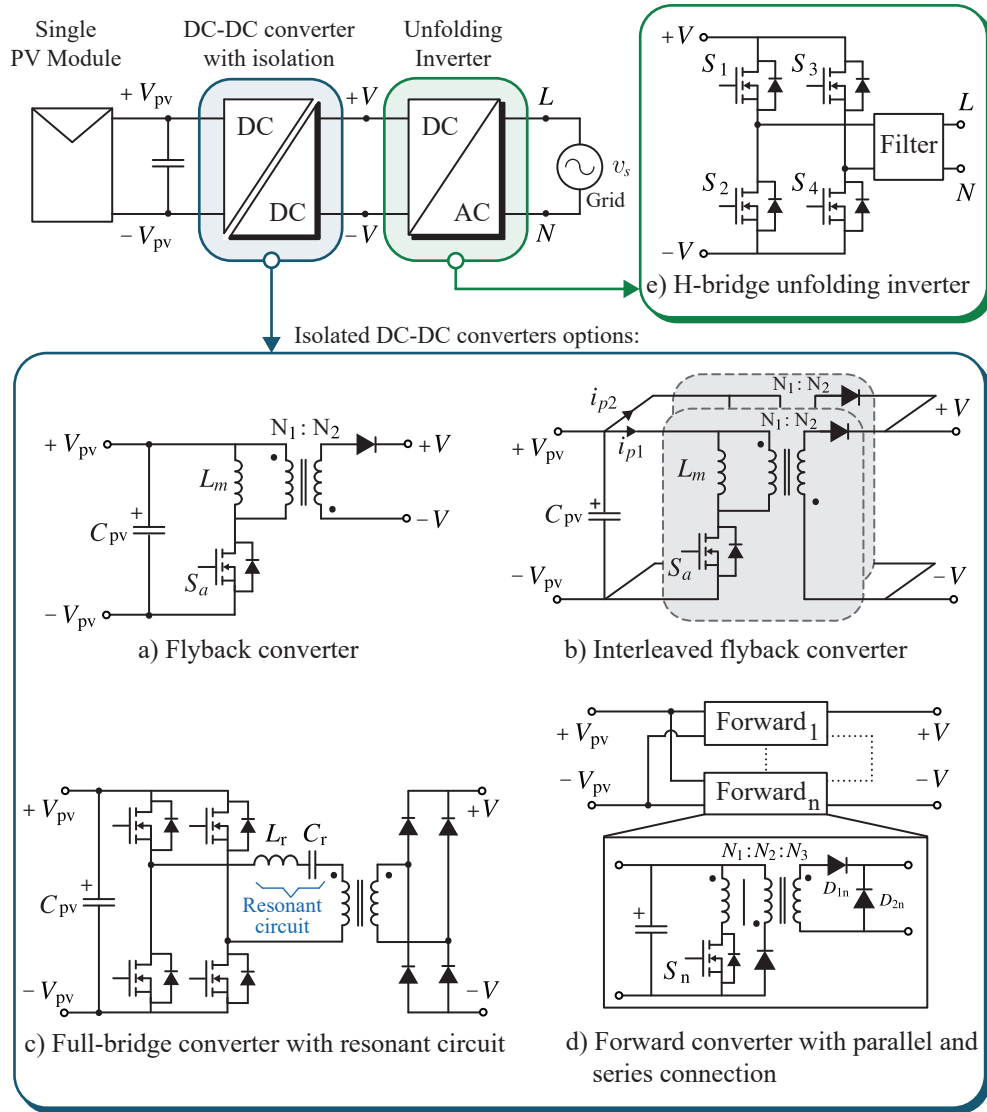


Figure 2.13. Topologies of the unfolding inverter with galvanic isolated DC-DC stage.

half-cycle. The topology presented in Fig. 2.13(d) is based on a forward DC-DC converter. The experimental prototype presents eight multicore forward converters, whose inputs of the converters are connected in parallel and whose outputs are connected in series [39]. The parallel connection allows to reduce the current stress in the power devices in the primary side, and the other advantage of this topology is that the series connection of the outputs of the forward converters allows to reduce the number of the transformer turns ratio. These eight DC-DC forward converters are operated in discontinuous conduction mode (DCM) to produce a rectified sinusoidal current, which is finally unfolded by the current source inverter (second

stage).

Other interesting topologies for the DC-DC stage are the Ćuk [40] and zeta converters [41]. The output current of these converters is a rectified sinusoidal waveform, which is unfolded by a current source inverter for grid connection.

2.2.2 High switching frequency inverter topologies

Another solution for grid connection of the PV panel is presented in Fig. 2.14. These topologies are composed by two power converter stages, similar to the unfolding inverters. However, the main difference between these two architectures is that a DC-link capacitor (C_{DC}) is necessary to decouple the DC-DC stage and DC-AC stage. Also, the semiconductors of the inverter (second stage) operate with high switching frequency (HSF), which constitutes another difference.

In addition, other capacitor is used in this solution. The input capacitor (C_{PV}) of the architecture decouples the PV voltage and PV current from the power stages.

In this subsection, a topologies review is presented for DC-DC stage and DC-AC stage.

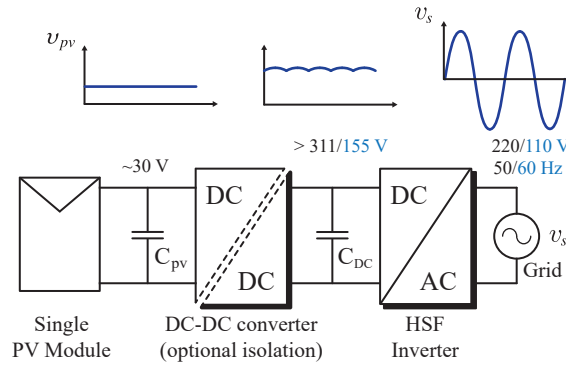


Figure 2.14. General structure of the high switching frequency (HSF) inverter with DC-DC stage.

2.2.2.1 High switching frequency inverter with non-isolated DC-DC converters

As mentioned previously, it is necessary to elevate the voltage of the PV module around 20% over the peak grid voltage, namely that voltage conversion ratio in the DC-DC stage should be ten times approximately in the 50 Hz grid. Thus, the high step-up converters are analyzed below.

A detailed classification of DC-DC converters with widely elevation ratio is proposed by Li *et al.*. This classification based on the power circuit structure is divided in five categories: high step-up converters with coupled inductors, high step-up converters with switched capacitor, high step-up converters with switched inductor and capacitor, high step-up converters with coupled inductor and switched capacitor, and high step-up interleaved boost converters. Also, a category of the high step-up interleaved converters with winding cross coupled inductors is introduced in this summary, as shown in [42]. It is worth mentioning that several DC-DC converters analyzed in this review are not originally focused on PV applications. However,

some topologies can be used for grid connection of a PV panel, as the DC-DC converters with coupled inductors.

The coupled-inductor approach is widely used in the applications, in which the high voltage conversion ratio is necessary, as it is in this case. A wide analysis of the coupled-inductor converters is given in [43]. The topologies based on coupled inductors in this review are classified in five categories: cascaded coupled-inductor boost converter, stacked coupled-inductor boost converter, multiwinding coupled-inductor boost converter, integrated coupled-inductor boost converter, and interleaved coupled-inductor boost converter. The main features are high step-up voltage gain without extreme duty ratio, low switch voltage stress, the possibility of recycling the leakage energy of the coupled inductor with an appropriate clamp circuit, thus the switch voltage spikes can be reduced, and the input current ripple can be reduced with interleaved techniques. The boost converters with coupled inductor are considered to be a promising solution for PV microinverters. In this context, a high set-up DC-DC converter has been proposed in [44]. The Fig. 2.15 presents the power circuit of this solution. The high voltage conversion ratio is obtained through the connection of the capacitor, diode and pairs of inductor. The experimental results indicate that the maximum efficiency achieved is 95.3 % at 40 % of full load. The input voltage used in the tests is 15 V and the output voltage is 200 V. Therefore, the voltage gain of this DC-DC converter is 13 times with a turns ratio of five and 55 % of duty ratio.

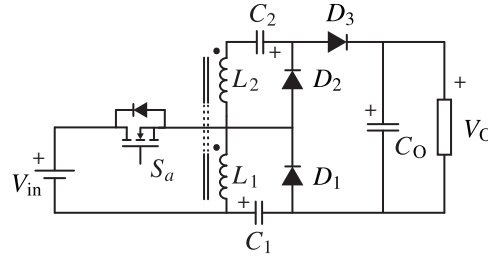


Figure 2.15. High step-up DC-DC converter with coupled inductor.

Another solution based on coupled inductor is shown in Fig. 2.16. The topology presents one passive clamp network (C_1 , D_1) and an intermediate energy storage capacitor (C_2), together with the coupled inductor (L_1 , L_2). To validate the DC-DC converter, a laboratory prototype of 400 W was proposed in [45], in which the input and output voltages reported were 40 V and 400V, respectively, and the turns ratio of the coupled inductor was four. Under full load, the efficiency of the converter was 96 % due to the leakage energy is recycled by the clamp circuit.

In the Fig. 2.17 it can be seen another high step-up converter, which includes two pairs of switched capacitors and coupled inductors. This topology is employed as part of the DC-DC conversion stage in the PV microinverter presented in [46]. The next stage is composed by a full-bridge inverter. This is controlled using a hybrid pulse width modulation (HPWM). In the experimental validation, the maximum efficiency of the converter is 96 % at 100 W. The input voltage of the PV microinverter is from 20 V to 40 V and the grid voltage is 220 V_{rms} . Therefore, the elevation ratio of the DC- DC converter is about ten times.

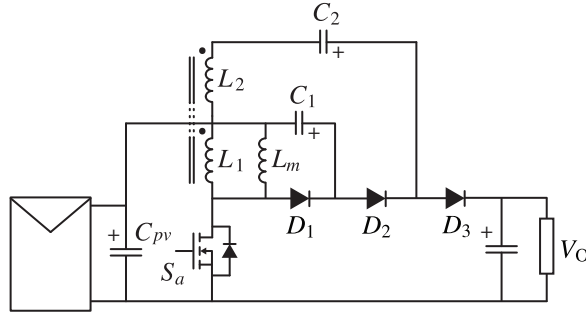


Figure 2.16. High step-up DC-DC converter with coupled inductor and intermediate energy storage capacitor.

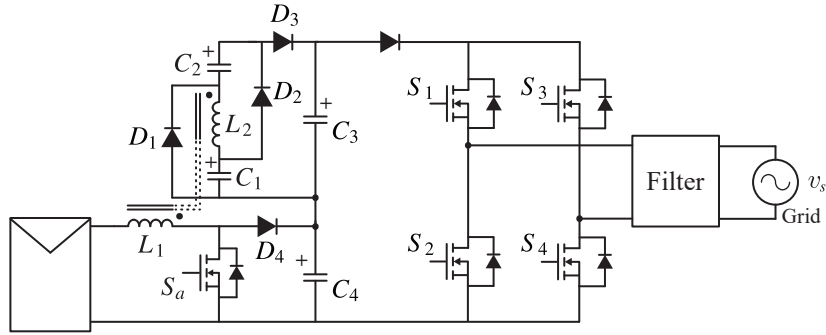


Figure 2.17. High step-up DC-DC converter with coupled inductor and HSF inverter.

2.2.2.2 High switching frequency inverter with isolated DC-DC converters

As for the isolated unfolding inverters, the topologies based on flyback converter are widely employed to achieve galvanic isolation between the PV panel and grid, elevate the PV voltage, and perform MPPT. In [47], a flyback converter is proposed as the DC-DC stage, followed by a full-bridge voltage inverter. The power circuit of these topologies are shown in Fig. 2.18.

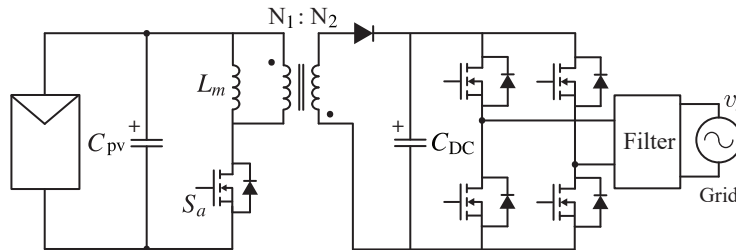


Figure 2.18. Flyback converter with HSF inverter.

The DC-DC converter operates in continuous conduction mode, while the inverter is controlled with carrier based PWM to generate two levels of output voltage. One disadvantage of this topology is that the efficiency can decrease, if the turn ratio of the transformer is high due to the leakage inductance increases. To overcome this issue, some solutions have been proposed, one of such topologies is based on an active resonant-clamp circuit and a voltage-doubler circuit, as shown in Fig. 2.19. The clamp circuit is composed by a capacitor (C_r) and a power device (S_b) to reduce the voltage stress in the central power device S_a and recycle the energy stored in the leakage and magnetizing inductances. On the other hand, the voltage-doubler circuit consist of two resonant capacitors and two diodes to achieve the turn-off zero-current switching of the diodes, as shown in [48] and [49]. Thus, the power losses are reduced. One variation of this topology has been proposed by Choi, in which the secondary side of the transformer is composed by only one resonant capacitor in the voltage-doubler rectifier. This high step-up DC-DC converter is part of the first stage of PV microinverter topology presented in [50], and the second stage is an H-bridge inverter with a sinusoidal pulse-width modulation. The efficiency in both DC-DC topologies based on flyback converter approach is around 97 %.

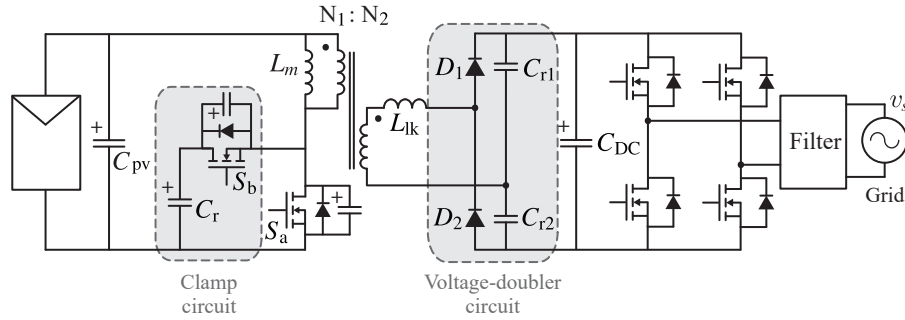


Figure 2.19. Flyback converter and voltage-doubler circuit with active clamp circuit and HSF inverter.

Fig. 2.20 shows an alternative solution for PV microinverter. The first stage consists of the boost-half bridge converter proposed in [51] and [52]. The topology is based on the conventional boost converter and the dual half-bridge converter. The primary side of the transformer includes a structure similar to the boost converter, in which two capacitors are incorporated at the output of this converter (C_a and C_b). A voltage-doubler circuit is part of the secondary side of the transformer. It is composed by two diodes and two capacitors. The power devices (S_a and S_b) of this stage are controlled using complementary duty cycles. The second stage of this microinverter is a full-bridge inverter modulated with synchronized PWM. A 210 W experimental prototype is used to verify the operation of topology and its control. The tests show that the maximum efficiency achieved is between 97-98.2 %, and the total harmonic distortion is between 0.9-2.87 %. In [53] and [54], a modification in the DC-DC stage of the previous topology is presented, where the interleaved approach is used in the primary stage of the converter to reduce the input ripple current and increase the capacitors lifetime.

In [55], another topology based on full-bridge resonant converter is presented to connect a PV panel to the grid. The primary side of the transformer of this topology presents the same

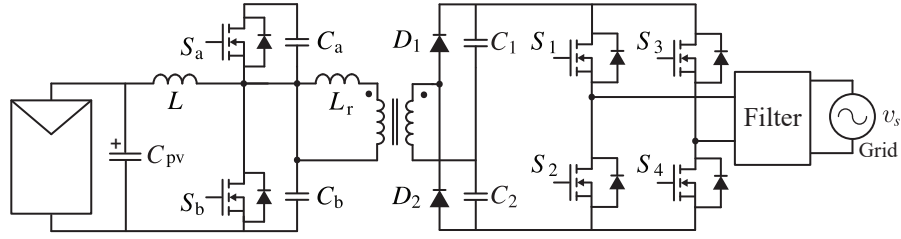


Figure 2.20. Boost-half bridge DC-DC converter with HSF inverter.

structure that in Fig. 2.13(c). However, a voltage-doubler circuit is connected in the second side of the transformer to generate the output DC voltage, as shown in Fig. 2.20. The main advantage of this DC-DC converter is that the resonant capacitor avoids introduction of the DC voltage to the transformer. A similar topology is also proposed in [56], the difference is that a bidirectional AC switch is incorporated in the secondary winding of the transformer to obtain high efficiency. This additional switch allows direct power transfer to the load for a wide range of the duty cycle.

The topologies based on push-pull converter are another attractive solution to increment the voltage gain of the DC-DC conversion stage. An input inductor (boost inductor), an LC resonant circuit and a voltage-doubler circuit is introduced in the conventional push-pull topology, as presented in Fig. 2.21. The soft switching technique is implemented in this converter to reduce the losses in the power devices. In order to validate the operation of the proposed topology, a 250 W laboratory prototype is used. An efficiency of 96.6 % has been presented in [57] for a grid of 220 V_{rms} .

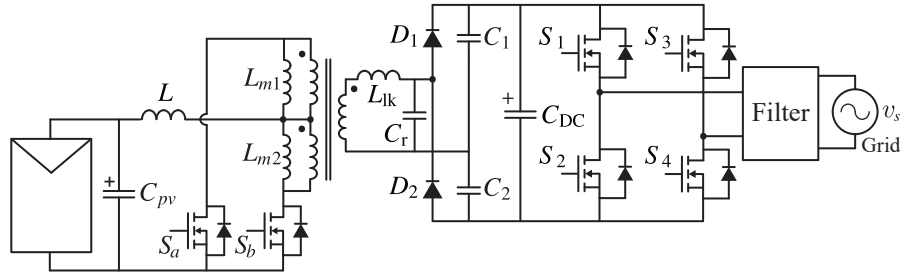


Figure 2.21. High step-up converter based on push-pull topology with HSF inverter.

2.3 Multi-stage topologies

The last category of the global classification of the microinverter topologies is the converters with several stages of conversions. In the multi-stage topologies, the tendency is to use galvanic isolation in the DC-DC stage [58]. The high step-up DC-DC converter based on resonant full-bridge topology has been proposed by Vinnikov. Fig. 2.22 presents the topology for PV applications. The DC-DC topology is composed of two conversion stages. The first

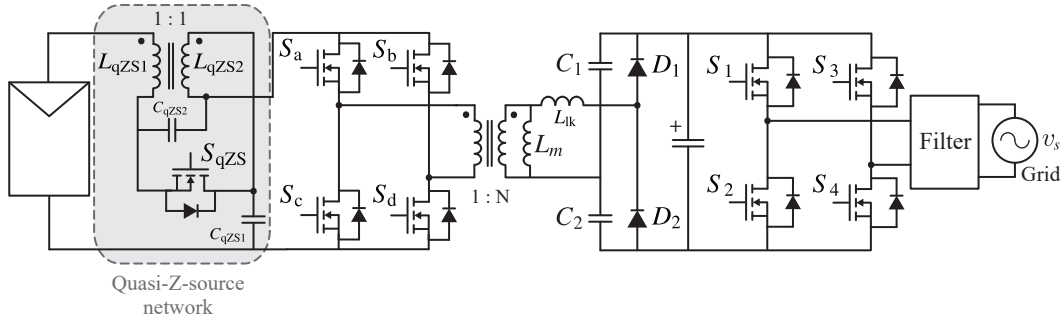


Figure 2.22. High step-up converter based on resonant full-bridge converter with HSF inverter.

section is an improved quasi-Z-source network, which includes a power device (MOSFET) and a coupled inductor to reduce the conduction losses and the current ripple in the input of the converter. A variation of the resonant full-bridge converter is connected in series with the previous section. The resonant circuit is located in the second winding of the transformer. The leakage inductance of the transformer and the capacitors of the voltage doubler-circuit integrate the resonant network. Then, the DC-AC converter is a full-bridge topology, where an asymmetrical unipolar PWM is employed [59].

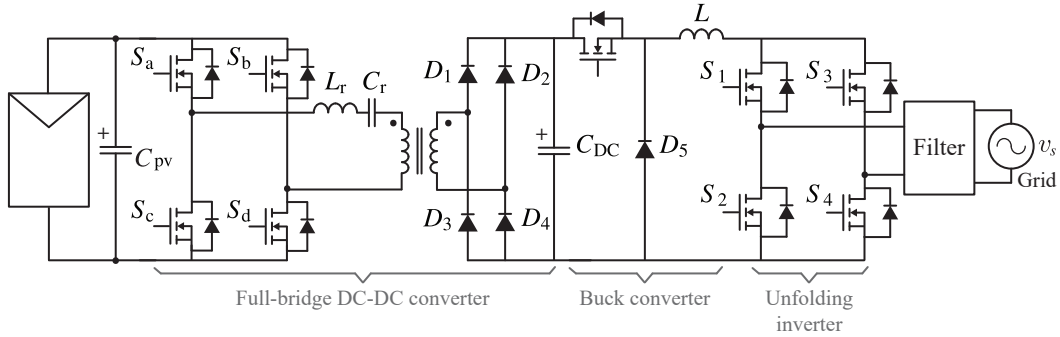


Figure 2.23. High step-up converter based on full-bridge converter and buck converter in cascaded with unfolding inverter.

Other topologies with three conversion stages are presented in [60] and [61], which use the unfolding concept for DC-AC stage. In [60], the full-bridge DC-DC converter and buck converter are used in the DC-DC converter. The main function of the full-bridge converter is to elevate the input voltage to 475 V. This DC-DC converter is controlled using phase-shift pulsewidth-modulation. Then, a buck boost is connected in series with the output of the bridge diode, as shown in Fig. 2.23. A current-mode control is employed in this stage to generate a rectified sine-wave output current. In this case, the maximum efficiency is 89 % with a THD of around 5 %. Also, a detailed reliability analysis is presented for this topology to evaluate the life time of the inverter. In [61], a similar approach of the previously mentioned topology is used. One difference is in the first stage, because a push-pull converter is employed in this case instead of the full-bridge DC-DC converter.

2.3.1 Summary and discussion

In this chapter, a review of different inverter topologies for AC-module configuration is presented. According to the number of the stages, the topologies can be classified into three arrangements: single stage, two stages and multi stages, as shown in the Table 2.1. Based on the type of the inverter and the isolation these arrangements are divided in differential mode connection, bypass mode connection, unfolding inverter and high switching frequency inverter.

The single-stage topologies are based on two connection modes: differential mode connection and bypass mode connection, which elevate the input voltage of the PV panel, track the maximum power point of the PV panel, and connect the PV panel to the grid with only one power stage. The topologies in the differential mode connection are composed by two bidirectional DC-DC converters, whose inputs are connected in parallel to the PV panel and their outputs are connecting to the grid differentially. The output voltage of each DC-DC converter presents a DC-biased and an AC component. Topologies based on DC-DC boost converter are the most popular architecture within the differential mode connection inverter. Also, some topologies with isolated converters are found in the literature, as flyback and \hat{c} uk converters. It is worth mentioning that DC-DC converters must be bidirectional because a power circulating is generated in the inverter due to the differential connection.

On the other hand, the single-stage inverter with bypass mode connection is also composed by two buck-boost DC-DC converters, which are shared the input source. In this case, each DC-DC converter operates on half cycle of the grid voltage. The DC-DC converters are activated in the positive or negative cycle of the grid voltage through the semiconductor devices. This approach is used in the flyback inverter, where each secondary winding is kept active during each half cycle of the grid voltage through the semiconductors present in each secondary winding. Note that, the power decoupling in the single-stage topologies is realized at the input capacitor.

The two-stage architecture is mainly classified in terms of the DC-AC stage. In the two-stage microinverters, the DC-DC stage amplifies the PV voltage to a level compatible with the grid voltage and it also extracts the maximum power of the PV module. The second stage (inverter) injects the sinusoidal current to the grid (grid connection). The first category of this architecture is the unfolding inverter. In this solution, the DC-DC converter generates a rectified sinusoidal current, which is unfolded by the inverter. In this case, several DC-DC converters with isolated and without isolated galvanic have been proposed. The most popular converters are buck-boost converter and flyback converter, respectively. One feature of the unfolding inverters is that the power decoupling is also made in the input capacitor C_{pv} .

The second category of the two-stage topologies are the high switching frequency inverter, where the DC-DC converter elevates the PV voltage to over the peak grid voltage. Then, a step-down inverter on the second stage operated at high switching frequency injects AC power to the grid. The power decoupling in these topologies is performed at the DC-link side.

The last arrangement is the multi-stage category, in which two DC-DC converters in cascaded are used before the unfolding inverter or high switching frequency inverter.

The most popular architecture used in the academic and industrial fields is based on the two-stage approach. One option to inject a PV module into the grid is the topology composed by a step-up DC-DC converter followed to a step-down inverter. In this arrangement, the decoupling power between the input and output is done through a electrolytic DC-link capacitor, which presents low capacitance. However, the main drawback is the implementa-

tion of its control since this inverter operates at high frequency. Thus, the gate drive of the semiconductors should be able to produce fast turn-on and turn-off transients.

In order to solve this, the unfolding inverter is introduced, where the second stage operates at fundamental frequency. Thus, a simple control can be employed and the switching losses can be reduced. However, a bulky capacitor in parallel with the PV panel is used to the power decoupling.

Another challenge of the microinverters is high voltage boost required to interface the PV module to the grid. The use of a transformer in the DC-DC converters is an option to solve this issue, where the flyback converter and full-bridge converter with resonant circuit are the most used topologies for the isolated solution. However, the used of a transformer increases the size of the microinverters. On the other hand, the DC-DC converter with high step-up converters based on the coupled inductors is a practical solution implemented for the transformerless topologies.

Another important parameter to the comparison is the grid voltage. The voltage gain for inverters to connect at the European grid is double than at the American grid. For this reason, the topologies without isolation are generally connected to the American grid, to avoid issues in the implementation, such as high duty cycles.

To improve the efficiency, several single-stage topologies in the last years have been proposed, which are based on the hypothesis that less conversion stages provide better efficiency. One solution is the dual boost inverter originally introduced in 1995 by Caceres *et. al* [17].

As mentioned earlier, to obtain a sinusoidal output voltage, each DC-DC boost converter generates a sinusoidal output (with opposite phase between each other), relative to a substantial DC-bias (equal for both converters) which is canceled through the differential connection, leaving only the AC component at the output. Thus, each converter works around an operating point (the DC-bias) but with a large variable output voltage range (the AC component). Additionally, the product between the control and state variables, present in the averaged model of the conventional DC-DC boost converter, shows the high non-linearity of the system [18]. Consequently, the main challenge of DBI is in the design of a control strategy. Thus, some non-linear strategies are proposed in the next chapter.

Table 2.1. Summary of the microinverter topologies.

General Concept	SINGLE STAGE		TWO STAGES		MULTI STAGES
	Differential mode connection	Bypass mode connection	Unfolding inverter	High switching frequency inverter	
# Cap.	One - C_{pv}	One - C_{pv}	One - C_{pv}	Two ($C_{pv} - C_{DC}$)	Two ($C_{pv} - C_{DC}$)
# Conv.*	2 DC-DC	2 DC-DC	1 DC-DC	1 DC-DC and 1 DC-AC	2 DC-DC and 1 DC-AC
Features	<ul style="list-style-type: none"> Medium switching losses Complex control 	<ul style="list-style-type: none"> Low switching losses Easy control 	<ul style="list-style-type: none"> Low switching losses Easy control 	<ul style="list-style-type: none"> High switching losses Difficult control 	<ul style="list-style-type: none"> Medium switching losses Difficult control
Examples	No commercial product	No commercial product	 Enphase M250	 SPARQ's 215	 UBIK S350 Opti'Verter

* Number of converters with high switching frequency

CONTROL TECHNIQUES FOR DBI

In power electronics, a widely used strategy to control is the linear approach, which is based on the averaged model of power converters. The standard control scheme presents one or more commonly proportional-integral (PI) regulators and a modulation stage. The fast response, easy implementation, and simple design are some advantages of this control strategy. For these reason, the linear controller is part of this work. However, the dual boost inverter is not an easy system to linearize due to its singular operation. Hence, the non-linear control strategies were proposed and developed in this chapter to regulate the DBI.

These control strategies are Finite Control Set-Model Predictive Control (FCS-MPC), flatness-based control and sliding mode control. The main features, advantages and disadvantages of the linear control and the three non-linear control strategies are summarized in Table 3.1.

Simulations results are shown in order to validate the control strategies and the converter for grid-connected PV applications. The last section gives a comparison between the linear control and these three non-linear control methods .

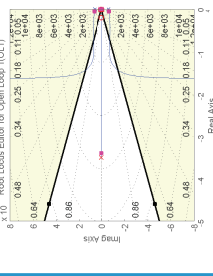
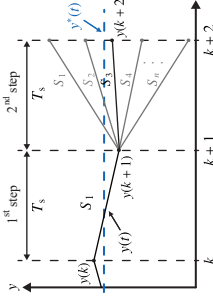
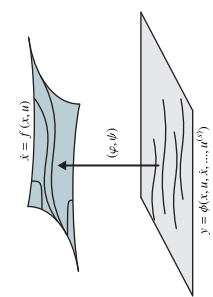
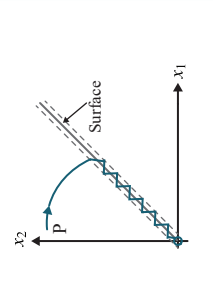
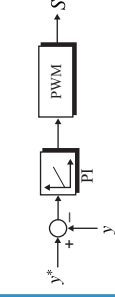
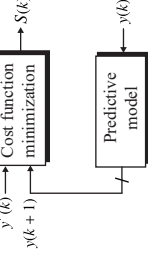
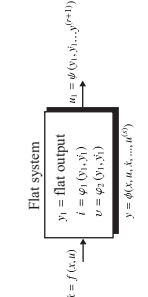
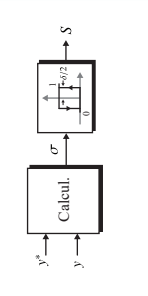
3.1 Overview of control techniques for DBI

From the introduction of the DBI, several control techniques have been proposed in the literature, which can be classified into two main groups of control strategies: independent and global, as shown in Fig. 3.1.

In the first group, each boost converter is controlled individually to generate its respective sinusoidal output voltage employing linear and non-linear methods. In most cases, a cascaded linear control scheme is used, with a slower outer control loop for the capacitor voltage, and a faster (higher bandwidth) control loop for the inductor current. Examples of this control strategy can be found in [7, 13, 14], where proportional-integral (PI) controllers are employed in both loops. However, PI controllers can lead to steady-state errors and phase shifts when used to control sinusoidal signals. For this reason, proportional resonant (PR) controllers have been proposed in [15, 19], as an alternative to overcome these issues. One common condition for these control strategies is to ensure that the minimum DC-bias is composed of the input DC voltage and half of the amplitude of the output AC voltage to achieve the proper operation of each DC-DC converter.

Also, some non-linear techniques can be found in the group of independent control strate-

Table 3.1. Summary of the control strategies for the DBI.

	LINEAR CONTROL	FCS-MPC	FLATNESS-BASED CONTROL	SLIDING MODE CONTROL
Main approach				
Features	<ul style="list-style-type: none"> Linear model PI/PR parameters adjustment 	<ul style="list-style-type: none"> Discrete time model Cost function definition 	<ul style="list-style-type: none"> Differentially flat system (flat output) 	<ul style="list-style-type: none"> Sliding surface
Control scheme				
Advantages	<ul style="list-style-type: none"> Simple design Fixed switching frequency 	<ul style="list-style-type: none"> Non-linear controller No modulation Easy to include nonlinearities and constraints 	<ul style="list-style-type: none"> No differential equations Robust against model uncertainties and disturbances 	<ul style="list-style-type: none"> Non-linear controller No modulation Robust against model uncertainties and disturbances
Disadvantages	<ul style="list-style-type: none"> Less robust for non-linear systems Not easy to include nonlinearities and constraints Requires modulator 	<ul style="list-style-type: none"> Variable switching frequency High computational requirements 	<ul style="list-style-type: none"> High computational requirements Complex theory Requires modulator 	<ul style="list-style-type: none"> Variable switching frequency Digital implementation requires high sample time Complex theory

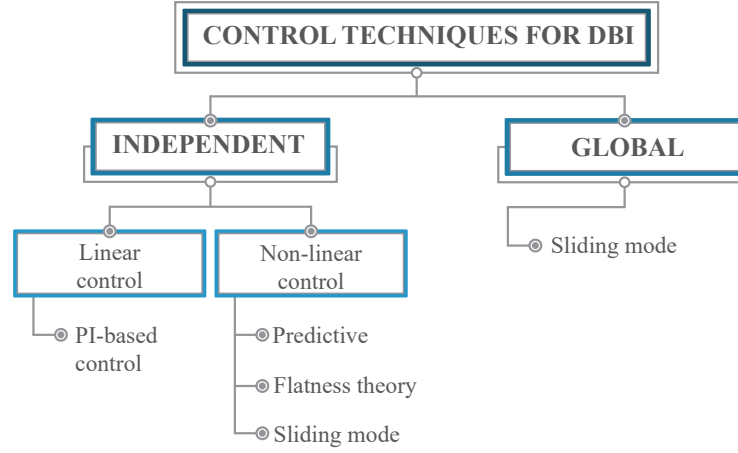


Figure 3.1. Classification of control strategies for DBI.

gies. Among them: sliding mode control, with a switching surface composed by the error in the voltage of the capacitor and the inductor current is presented in [62]; a dynamic linearizing modulator used to control the capacitor voltage is presented in [63]; the differential flatness propriety, as shown in [64], where the individual control of the output voltage is indirectly accomplished through the regulation of energy stored in each boost converter; and Finite Control Set-Model Predictive Control, where a non-linear discrete model of the DBI is used to predict and optimize the behavior of each converter, as introduced in [65]. Also, a short summary of the independent control strategy is presented in Table 3.2

In contrast, in the global control strategy group, the differential output AC voltage of the DBI is considered to be the main control objective. This type of control was introduced for the first time in [18], where a cascaded control diagram based on the sliding mode approach is applied to achieve the sinusoidal output voltage. The external control loop regulates the output voltage error of the inverter using a PI controller. The inner control loop corresponds to a switching surface, synthesized from the difference between the current of the inductors and the external controller output. One advantage of this strategy is the reduction of control loops, which leads to a decrease in the number of required sensors. An extended analysis of the equilibrium point for this control strategy is presented in [66], where the DC component of the capacitor voltages is automatically adjusted to the two-folds of the input voltage.

In most cases, the control strategies have been tested for passive loads (R and RL loads). Although good performances under perturbations have been achieved, the grid connection has not been thoroughly analyzed. This is mainly because it is difficult to find a relationship between the output current and the control variables of the inverter. Nevertheless, experimental validations of grid-connected DBI can be found in [15, 19]. In both cases, the cascaded linear strategy is used to control individually each boost converter, including an additional control loop based on active and reactive power. Therefore, five control loops in total are necessary to connect the DBI to the grid, making the design and implementation of the control system a complex process. This is particularly an issue for the DBI, which is intended for low power applications, such as grid-connected photovoltaic microinverters, for which low cost control

platforms are usually used.

Table 3.2. Review of the independent control strategies for the dual boost inverter.

Author and publication year	Type of load	Control strategy	Control objectives - Surface	Ref
Caceres, 1999	R, L and non-linear load	Sliding mode control	$\sigma = k_1(i_{L1} - i_{L1}^*) + k_2(v_{c1} - v_{c1}^*)$	[62]
Sanchis, 2005	R and non-linear load	Classic control (PI's)	Capacitor voltage and inductor current	[14]
Jang, 2011	R and non-linear load	Classic control (PI's)	Capacitor voltage and inductor current	[13]
Jang, 2013	Grid-connection	Classic control (PR's)	Capacitor voltage and inductor current	[19]
Zhu, 2013	R and RC	Classic control (PI's)	Capacitor voltage and inductor current	[7]
Kapil, 2015	Resistance	Dynamic linearizing modulator	Capacitor voltage	[63]
Abeywardana, 2016	Grid-connection	Classic control (PR+PI)	Capacitor voltage and inductor current	[16]

3.1.1 Description and model of dual boost inverter

To implement the linear control and the three non-linear control strategies for the DBI, it is necessary to define the main features and model of the inverter.

The DBI is composed by two DC-DC bidirectional boost converters, sharing the input source (PV panel), as illustrated in Fig. 3.2. As it can be observed, the inverter presents four semiconductor devices, two inductors in the input, and two capacitors in the output. The grid is connected between the positive nodes of the boost converter outputs (differential connection). Notice that, MOSFETs are used as power devices.

In the case that an independent control strategy has been considered to regulate the inverter, two control signals are defined S_1 and S_3 for each boost converter. To avoid simultaneous conduction of the power devices (short-circuit) and for both switches to be open (open-circuit) on each leg, the logic complement is used i.e, the signal S_2 is the complementary of the control signal S_1 , and the signal S_4 is the complementary of the control signal S_3 . Hence, four switching states are defined, as listed in Table 3.3 and illustrated in Fig. 3.3. Also, there will be eight conduction states depending on the grid current polarity.

In Fig. 3.4, a qualitative example is shown to explain the operation of the inverter. The theoretical behavior of the inductor currents (i_{L1} and i_{L2}) are presented to illustrate the eight conduction states. For example, the circuit equivalent for case 1 of switching state for the positive and negative grid current is shown in Fig. 3.3(a). When the gate signal S_1 is zero, the inductor current through L_1 flows from the PV capacitor to the output capacitor C_1 , and the inductor current L_1 increases, while in the other boost converter, the gate signal S_3 is high. The inductor current i_{L2} flows through the PV capacitor, where the current decreases. As it

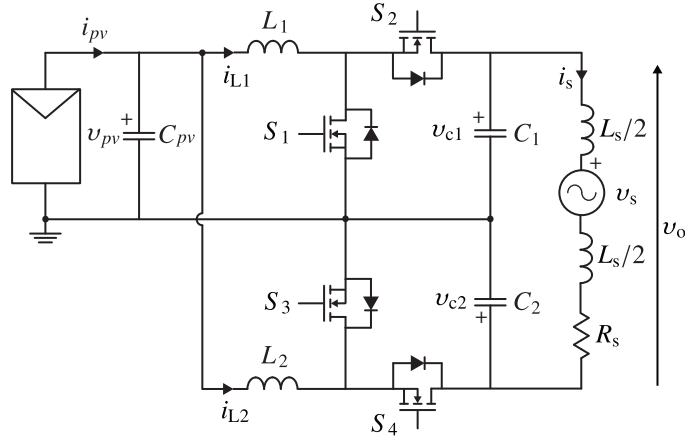


Figure 3.2. Dual boost inverter topology.

Table 3.3. Dual boost inverter switching and conduction states.

Switching state	S_1	S_2	S_3	S_4	Conduction state	Output current	Inductor currents
1	0	1	1	0	a.1	$i_s > 0$	$i_{L1} < 0, i_{L2} > 0$
					a.2	$i_s < 0$	
2	0	1	0	1	b.1	$i_s > 0$	$i_{L1} < 0, i_{L2} < 0$
					b.2	$i_s < 0$	
3	1	0	1	0	c.1	$i_s > 0$	$i_{L1} > 0, i_{L2} > 0$
					c.2	$i_s < 0$	
4	1	0	0	1	d.1	$i_s > 0$	$i_{L1} > 0, i_{L2} < 0$
					d.2	$i_s < 0$	

can be seen in the case a.1 from Fig. 3.4. Note that, the analysis for the other conduction states are similar, which can be observed in Fig. 3.4.

Considering the operation of the inverter, the averaged switched model is described by ,

Boost converter 1

$$L_1 \frac{di_{L1}(t)}{dt} = v_{pv} - v_{c1}(t) \cdot (1 - d_1(t)) \quad (3.1.1)$$

$$C_1 \frac{dv_{c1}(t)}{dt} = (1 - d_1(t)) \cdot i_{L1}(t) - i_s(t) \quad (3.1.2)$$

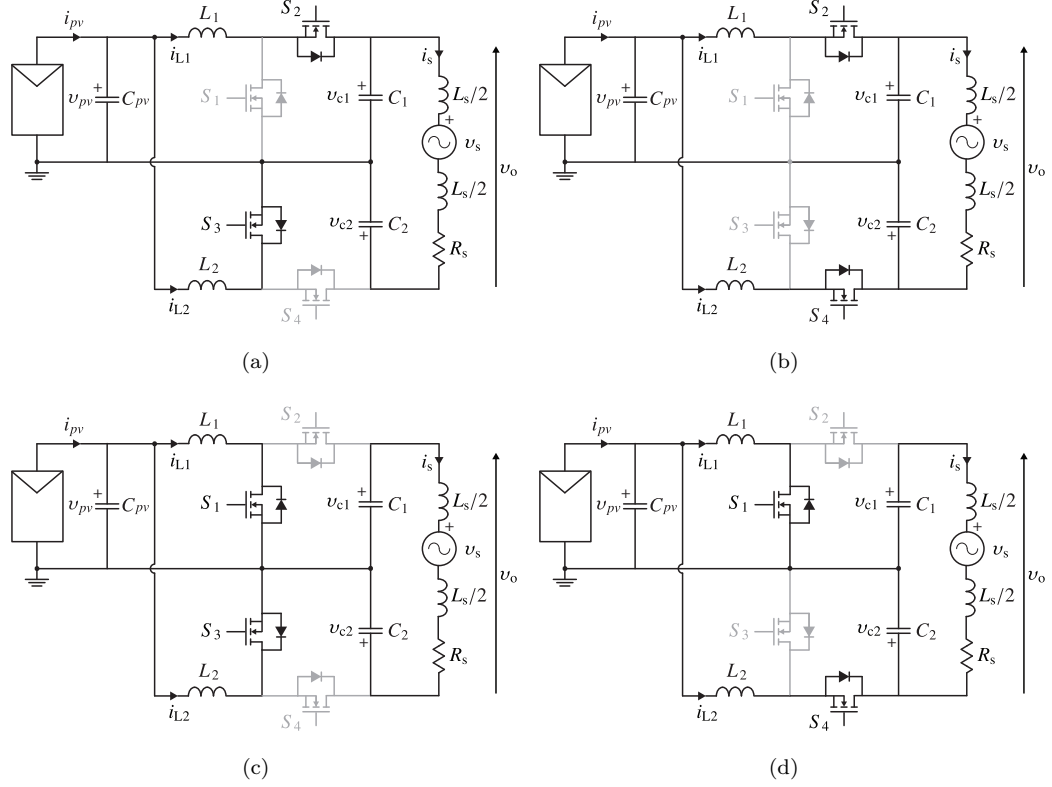


Figure 3.3. DBI switching states: (a) case 1, (b) case 2, (c) case 3, and (d) case 4.

Boost converter 2

$$L_2 \frac{di_{L2}(t)}{dt} = v_{pv} - v_{c2}(t) \cdot (1 - d_2(t)) \quad (3.1.3)$$

$$C_2 \frac{dv_{c2}(t)}{dt} = (1 - d_2(t)) \cdot i_{L2}(t) + i_s(t) \quad (3.1.4)$$

where i_{L1} and i_{L2} are the currents through the inductors L_1 and L_2 , i_s is the grid current, v_{c1} and v_{c2} are the voltage of the capacitors, v_{pv} is the input voltage, $d_1(t)$ is the duty cycle of boost converter 1, and $d_2(t)$ is the duty cycle of boost converter 2. Moreover, the DBI is integrated to the grid through an inductive filter L_s (R_s represents the resistance of the inductive filter and grid), as shown in the equivalent circuit of Fig. 3.5, and the voltage equation can be obtained by

$$L_s \frac{di_s(t)}{dt} = v_o(t) - i_s(t)R_s - v_s(t) \quad (3.1.5)$$

where the output voltage of the inverter is defined as,

$$v_o(t) = v_{c1}(t) - v_{c2}(t) \quad (3.1.6)$$

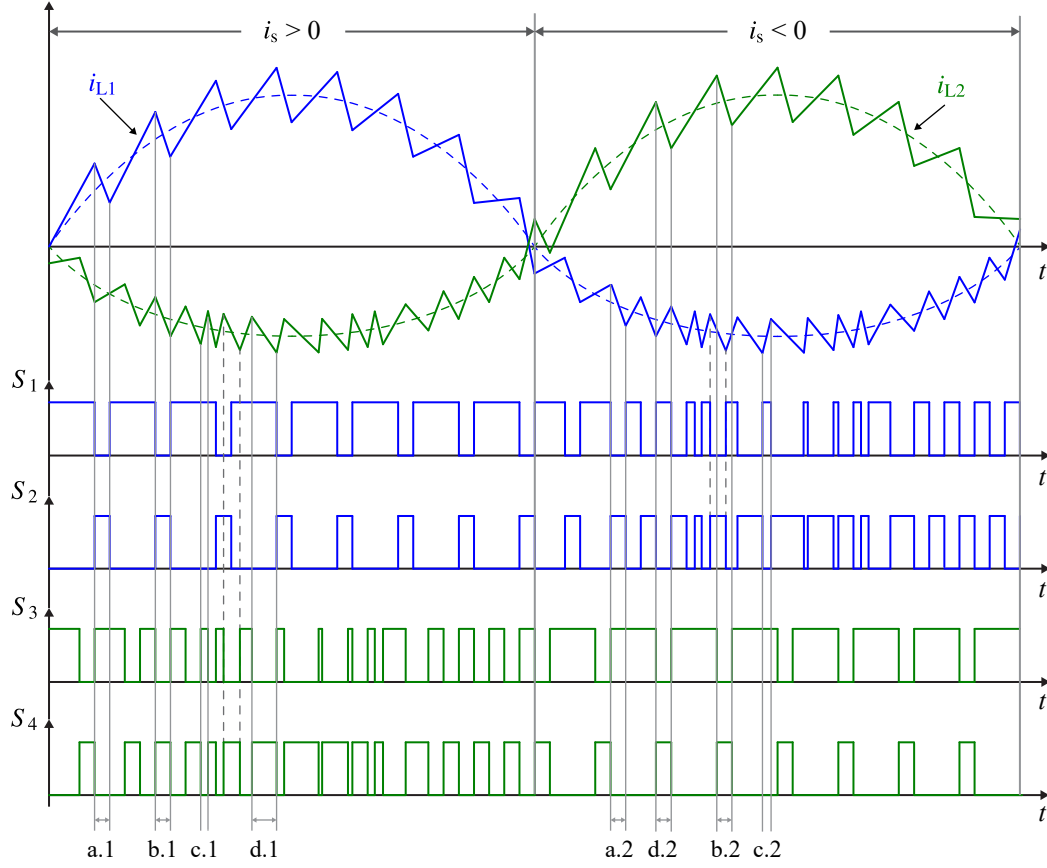


Figure 3.4. DBI conduction states when (a.1) $S_1 = 0$, $S_3 = 1$ and $i_s > 0$, (b.1) $S_1 = 0$, $S_3 = 0$ and $i_s > 0$, (c.1) $S_1 = 1$, $S_3 = 1$ and $i_s > 0$, (d.1) $S_1 = 1$, $S_3 = 0$ and $i_s > 0$, (a.2) $S_1 = 0$, $S_3 = 1$ and $i_s < 0$, (b.2) $S_1 = 0$, $S_3 = 0$ and $i_s < 0$, (c.2) $S_1 = 1$, $S_3 = 1$ and $i_s < 0$, and (d.2) $S_1 = 1$, $S_3 = 0$ and $i_s < 0$.

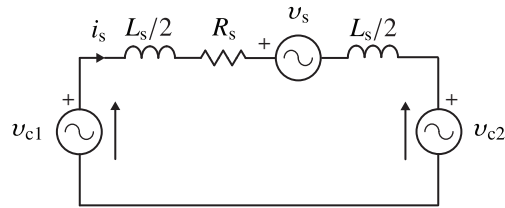


Figure 3.5. Equivalent model of the DBI with grid connection.

In order to obtain the maximum power output of the PV panel, the conventional perturb and observe (P&O) algorithm is implemented in the four control schemes due to its simplicity and effective tracking [68]. The search of the MPP in this algorithm, as its name indicates, is based on perturbing the reference voltage and observing the PV panel behavior to select

the direction of the next perturbation. The flow diagram is shown in Fig. 3.7 to explain this approach. First, the voltage and current measurements of the PV panel are obtained to calculate the PV power. Then, the power is compared with the last measurement $P_{pv}(k-1)$ to know if the power decreased or increased. In the case that, the voltage reference increases by the algorithm and the PV panel is operating on the left side of the MPP, the power should increase. Considering the same perturbation, but the PV panel is operating on the right side of the MPP, the power should decrease. When the voltage reference decreases, the opposite behavior in regard to the increased perturbation is obtained. Also, the amplitude of the perturbation in the reference voltage (Δv) is the same in all cases, but its direction is selected through the power variation. When the power measurement is higher than the last iteration, the perturbation in the voltage reference will continue in the same direction. But if the power measurement is lower than the last iteration, the direction of the perturbation in the voltage reference will change.

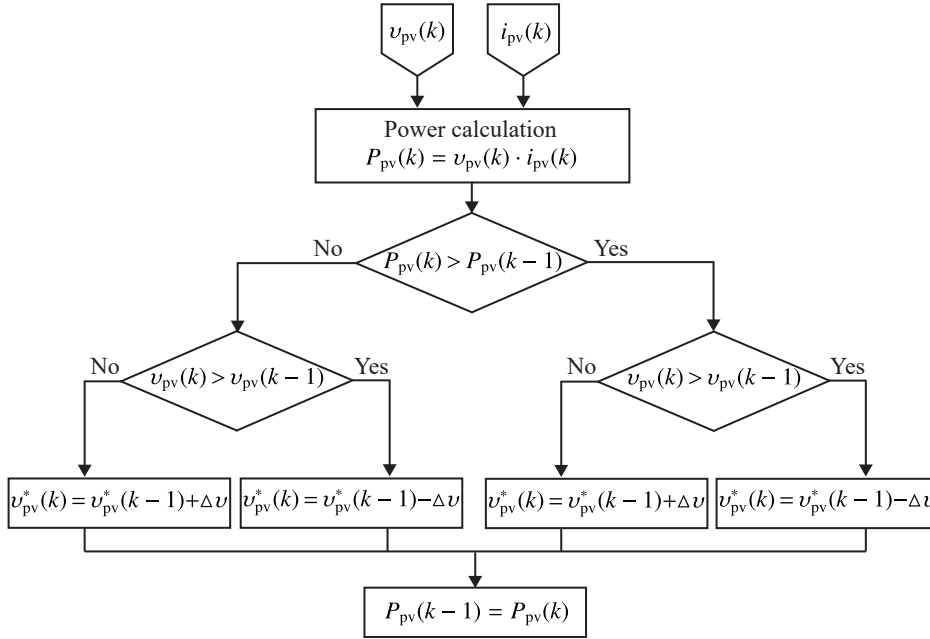


Figure 3.7. Flow diagram of P&O MPPT algorithm [68].

3.2.2 Control of the input capacitor energy

In order to regulate the input voltage of the capacitor, i.e the output voltage of the PV panel, an indirect control is used, which is based on the regulation of the input capacitor C_{pv} energy. The transfer function for this control loop is defined through the power balance of the inverter, which is expressed as,

$$v_{pv}i_{in} = v_{s,rms}i_{s,rms} \quad (3.2.1)$$

where i_{in} is the input current of the inverter, as shown in Fig. 3.8. This current is possible to determine as,

$$i_{in} = i_{pv} - i_{Cpv} \quad (3.2.2)$$

Considering the PV current i_{pv} as a perturbation, and the negative sign of the current through the PV capacitor i_{Cpv} as part of the plant, the expression in (3.2.1) can be written as,

$$\frac{C_{pv}}{2} \frac{dv_{pv}^2}{dt} = \frac{\widehat{V}_s \widehat{I}_s}{2} \quad (3.2.3)$$

As a result of these considerations, the transfer function expressed in Laplace domain can be defined as,

$$\frac{v_{pv}^2(s)}{P(s)} = \frac{2}{C_{pv} \cdot s} \quad (3.2.4)$$

Finally, the PI controller is used to regulate the energy of the input capacitor C_{pv} . The reference of the PV voltage v_{pv}^* is obtained from the MPPT algorithm as previously mentioned and explained. Then, the measurement of the PV voltage v_{pv} is filtered with a notch filter to reduce the second harmonic. The transfer function PI controller can be expressed as,

$$C_{PI}(s) = k_p \left(1 + \frac{k_i}{s} \right) \quad (3.2.5)$$

where k_p is the proportional gain and k_i is the integrative gain.

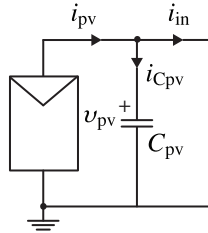


Figure 3.8. Input circuit of the grid-connected DBI.

3.2.3 Output voltage reference calculation

The active and reactive power transfer between the DBI and the grid can be calculated through the model of the grid connection of the inverter and the complex phasor [3] and [69].

In this analysis, the resistance of the inductive filter and grid are not considered in the equivalent circuit of the grid-connected inverter, as seen in Fig. 3.9(a). Thus, the voltage equation can be rewritten as,

$$v_s(t) = v_{c1} - v_{c2} - L_s \frac{di_s(t)}{dt} \quad (3.2.6)$$

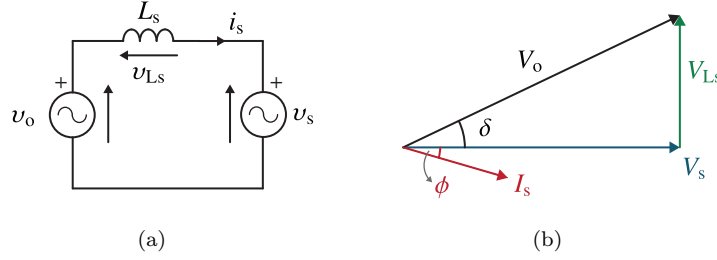


Figure 3.9. (a) Equivalent model of the DBI without resistance, and (b) phasor diagram.

Through the complex phasor diagram shown in Fig. 3.9(b), the active and reactive power can be expressed as,

$$P = \frac{V_s V_o}{2\omega L_s} \sin(\delta) \quad (3.2.7)$$

$$Q = \frac{V_s V_o}{2\omega L_s} \cos(\delta) - \frac{V_s^2}{2\omega L_s} \quad (3.2.8)$$

where V_s is the amplitude of the grid voltage, V_o is the amplitude of the inverter output voltage, and δ is the phase angle of the output voltage of the inverter regarding the grid voltage.

Considering small variations of the phase angle δ , the active and reactive power are calculated as,

$$P \approx \frac{V_s V_o}{2\omega L_s} \delta \quad (3.2.9)$$

$$Q \approx \frac{V_s (V_o - V_s)}{2\omega L_s} \quad (3.2.10)$$

Based on (3.2.9) and (3.2.10), the active and reactive power are regulated through the amplitude of the inverter output voltage (V_o) and its angle phase (δ) [69].

Since the main goal of the inverter is to inject current into the grid in phase with the grid voltage, the active power reference is considered. While the reactive power is not considered ($Q^* = 0$). Therefore, the capacitor voltage references can be calculated as,

$$v_{c1}^* = V_{DC} + \frac{V_s}{2} \sin \left(\omega_s t + \frac{2P^* \omega_s L_s}{V_s V_o} \right) \quad (3.2.11)$$

$$v_{c2}^* = V_{DC} - \frac{V_s}{2} \sin \left(\omega_s t + \frac{2P^* \omega_s L_s}{V_s V_o} \right) \quad (3.2.12)$$

where P^* is the active power reference obtained from the PI controller of the energy of the input capacitor C_{pv} . Also, the DC voltage reference is calculated as,

$$V_{DC} = k \times v_{pv} + \frac{V_s}{2} \quad (3.2.13)$$

where, k is a boost factor ($k > 1$), which ensures the minimum DC-bias. Because, the bottom waveform of the AC component must be greater than the input voltage in order to achieve the minimum elevation requirement.

3.2.4 Control of each boost converter

The proposed control scheme is based on the approach presented by Sanchis in [14] and [70], where each boost converter is regulated by two control loops, which include compensations in order to achieve the variable operation of the inverter. The inner control loop regulates the inductor current, while the external control loop regulates the capacitor voltage. Both control loops are composed by a proportional resonant (PR) controller since the references of capacitor voltages control loops are sinusoidal waveforms, and this type of controller achieves a stable operation under transients [19].

In order to design the parameters of the controller it is necessary to obtain the transfer function of the converter. Considering that the boost converters are symmetrical and the control strategy is independent for each converter, the analysis of the controller design is presented only for the boost converter 1.

The transfer function for the inner current control loop is based on (3.1.1) with two considerations. The first consideration is that the capacitor voltage v_{c1} in the variable operation can be considered as a variable gain, because the inductor current loop bandwidth is higher than the capacitor voltage loop bandwidth. Therefore, this voltage can be included as inverse gain in the current loop, as shown in Fig. 3.6. The second consideration is that the PV voltage can be interpreted as perturbation, which is eliminated through a gain with opposite value of PV voltage in the current control loop. As a result, the transfer function for the inner control loop is between the inductor current and the inductor voltage, which can be written as

$$\frac{i_{L1}(s)}{v_{L1}(s)} = \frac{1}{r_{L1} + L_1 s} \quad (3.2.14)$$

where, i_{L1} is the current through the inductor, v_{L1} is the inductor voltage and r_{L1} is the parasitic resistance in series with the inductor L_1 .

For the transfer function of the external voltage control loop, the same approach used for the inner current control loop is employed. In this case, the variable gain is $1 - d_1$, which can not be completely compensated since this variable is faster than the loop. Hence, a new expression is defined by (3.1.1) and (3.1.2), as follows

$$\left(v_{pv} - L_1 \frac{di_{L1}}{dt} \right) i_{L1} = \left(i_s + C_1 \frac{dv_{c1}}{dt} \right) v_{c1} \quad (3.2.15)$$

Note that the $1 - d_1$ is not presented in this equation. Also, the inductor voltage variations can be negligible in regard to the PV voltage and the voltage capacitor since the L is small. Thus, the inductor current can be written as

$$i_{L1} = (i_s + i_{c1}) \frac{v_{c1}}{v_{pv}} \quad (3.2.16)$$

In this case, the compensation is defined by the gain v_{c1}/v_{pv} . And the perturbation is the output current, which is introduced in the control loop to cancel its effect, as shown

in Fig. 3.6. Therefore, the transfer function for the external control loop is defined by the capacitor as follows

$$\frac{v_{c1}(s)}{i_{c1}(s)} = \frac{1 + r_{c1}C_1s}{C_1s} \quad (3.2.17)$$

where, i_{c1} is the current through the capacitor C_1 , and r_{c1} is the resistance parasitic in series with the capacitor C_1 . More details of the transfer functions used in the design of the linear control can be found in [70].

For both control loops, the PR controller is used since it is necessary a tracking of a sinusoidal with zero steady-state error. The transfer function of the PR controller is defined as

$$C_{PR}(s) = k_p + \frac{2k_i\omega_c s}{s^2 + 2\omega_c s + \omega_o^2} \quad (3.2.18)$$

where k_p is the proportional gain, k_i is the resonant gain, ω_c is the cut-off frequency, and ω_o is the fundamental frequency.

To summarize, the cascaded control loop for the boost converter is observed in Fig. 3.6. The voltage reference of voltage capacitor is obtained through (3.2.11). The capacitor voltage error is regulated using a PR controller. The output signal of this controller is the reference of the capacitor current. In order to calculate the inductor current reference i_{L1}^* , the output current i_s is added at the reference of the capacitor current. Then, the gain v_{c1}/v_{pv} is introduced in the output of the control loop. The inductor current error is also regulated by a PR controller. The output of this control loop is the reference of the inductor voltage, which is compensated to obtain the duty-cycle reference. The last stage is the modulation, where the duty-cycle is modulated with a carrier based on phase-shifted PWM. For the DBI, a 180° phase shift is introduced between the carrier signals of each boost converter.

3.2.5 Simulation results of the linear control for DBI

In order to validate the analysis of the linear control, the grid-connected dual boost inverter with the PV panel as input source is simulated in the PLECs software. The parameters of PV panel and the inverter are presented in Table 3.4. Notice that, the parameters of the inverter were selected in regards to the experimental prototype parameters.

The dynamic behavior of the dual boost inverter is evaluated with a variation in the solar irradiance from 1000 W/m² to 700 W/m², which is introduced at time $t = 2.0$ s. While, the steady-state operation is presented for the both operating points.

The figure 3.10 presents the simulation results of the steady-state behavior of the inverter for the nominal operation point, which is obtained with the solar irradiance is 1000 W/m². The references and measurements of the capacitor voltages are shown in Fig. 3.10(a), which are composed by DC component and a sinusoidal waveform. The DC components are around 112 V as expected. The amplitude of the capacitor voltages (v_{c1} and v_{c2}) is equal, and their phases are shifted 180°, as expected. Also, it is possible to identify that the output voltage tracking is achieved.

The figure 3.10(b) shows the behavior of the inductor current of each boost converter. The current waveforms are composed by a non-pure sinusoidal, where the positive and negative amplitudes are the same for both boost converters. The negative part of the inductor current is due to the differential connection of the boost converters.

Table 3.4. Simulation parameters of the linear control of DBI.

Symbol	Parameter	Value
PV Parameters		
V_{mpp}	PV voltage at MPP	29 V
P_{pv}	PV power	216 W
C_{pv}	Input capacitor	25 mF
Grid Parameters		
v_s	Grid voltage	110 V _{rms}
f_s	Grid frequency	60 Hz
L_s	Grid filter inductance	10 mH
Converter Parameters		
L_1, L_2	Boost converters inductors	55 μ H
C_1, C_2	Boost converters capacitors	5 μ F
Control Parameters		
f_{sw}	Switching frequency	80 kHz
k_p^{PV}	Proportional gain of PI (PV voltage control)	4
k_i^{PV}	Integral gain of PI (PV voltage control)	50
k_p^{PR1}	Proportional gain of PR (Voltage control)	0.25
k_i^{PR1}	Integral gain of PR (Voltage control)	0.0001
k_p^{PR2}	Proportional gain of PR (Current control)	0.4
k_i^{PR2}	Integral gain of PR (Current control)	0.1
ω_c	Cut-off frequency of PRs	10 rad/s

The grid voltage and current are illustrated in Fig. 3.10(c), where it is possible to identify that the current injected to the grid is sinusoidal and in phase with the grid voltage.

To validate the power quality of the DBI, the grid current spectrum and its total harmonic distortion (THD) are obtained, as shown in Fig. 3.11. Also, the IEEE standard 1547 is introduced in this figure to determine the limits of each harmonic. Note that the odd harmonics such as the third, fifth, seventh are presented. However, these harmonics are within of the range of the standard. Moreover, the THD of the grid current is 3.85 %, which fulfills with the standard (THD < 5 %).

In addition, the positive and negative peaks of the capacitor voltages and inductor currents present some oscillations, which are reflected in the grid current. Therefore, in the spectrum of the grid current is possible to identify harmonics at high frequencies. However, the THD is within of the standard limits and this harmonics content also complies with the standard.

The simulation results in steady-state for the 150 W at input power are shown in Fig. 3.12. The capacitor voltages and inductor currents waveforms present the same behavior regarding the nominal power case. The DC and AC component of the capacitor voltage are equal in the previous case. On the other hand, the positive amplitude of the inductor current is around 13 A, which is lower than the nominal case since the input power is reduced.

Also, the grid current is sinusoidal and in phase with the grid voltage as shown in Fig. 3.12(c). The harmonic content and the THD of the grid current are within accepted ranges by the standard, as presented in Fig. 3.13.

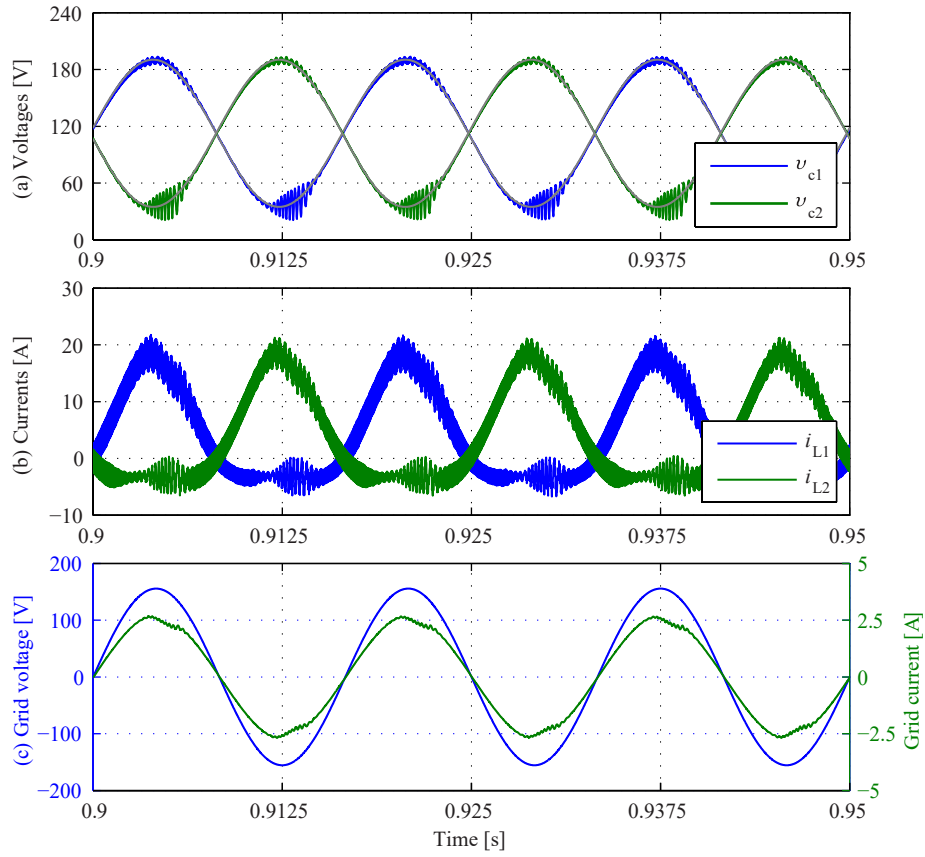


Figure 3.10. Steady-state results of linear control for DBI at 216 W of PV power: (a) Capacitor voltage of each boost converter, (b) inductor current of each boost converter, and (c) grid voltage and current.

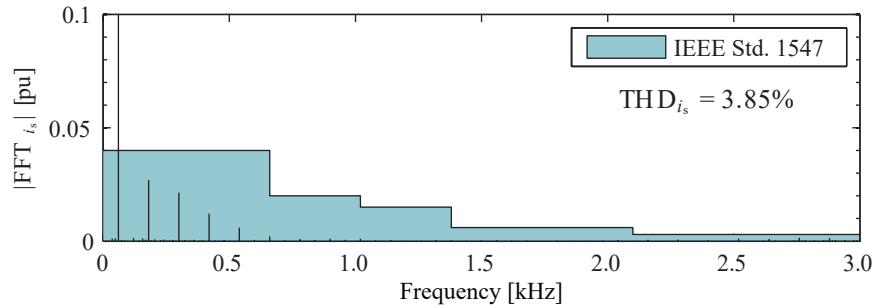


Figure 3.11. Grid current spectrum of DBI with linear control at 216 W of PV power.

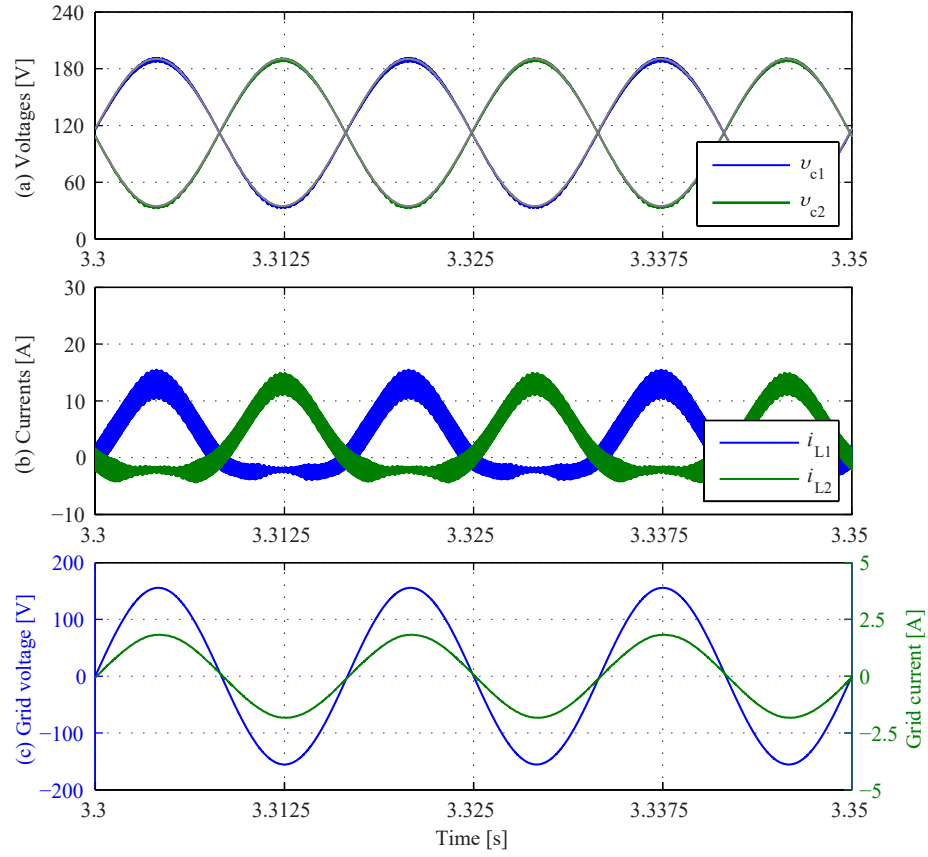


Figure 3.12. Steady-state results of linear control for DBI at 150 W of PV power: (a) Capacitor voltage of each boost converter, (b) inductor current of each boost converter, and (c) grid voltage and current.

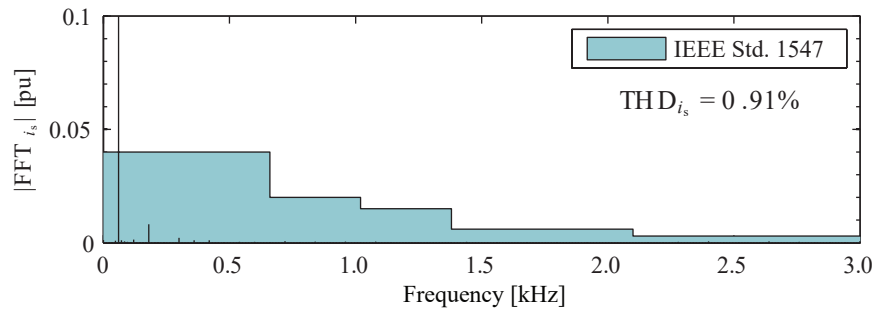


Figure 3.13. Grid current spectrum of DBI with linear control at 150 W of PV power.

The dynamic behavior of the DBI is presented in Fig. 3.14. The solar irradiance step is introduced at time $t = 2$ s. The reference of the PV voltage and its measurement are observed in Fig. 3.14(a), where the three voltage levels around the maximum power point can be identified when the PV panel is operating under uniform solar irradiance. Furthermore, the PV current decreases when the solar irradiance step is introduced, as shown in Fig. 3.14(b). Therefore, the input power is also reduced as illustrated in Fig. 3.14(c).

In addition, the behavior of the inverter during this solar irradiance change is presented in Fig. 3.15. Note that the capacitor voltages are kept constant when the input power decreases. While the amplitude of the output currents is reduced. This effect is reflected in the inductor currents, which also are reduced.

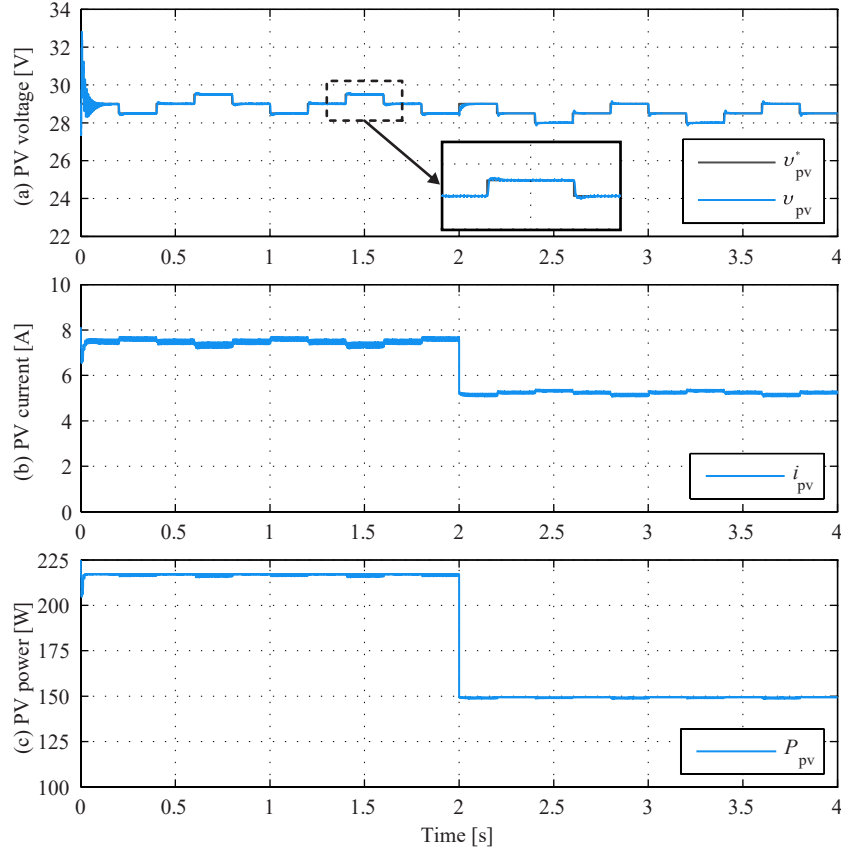


Figure 3.14. Dynamic results of linear control for DBI: (a) PV voltage, (b) PV current, and (c) PV power.

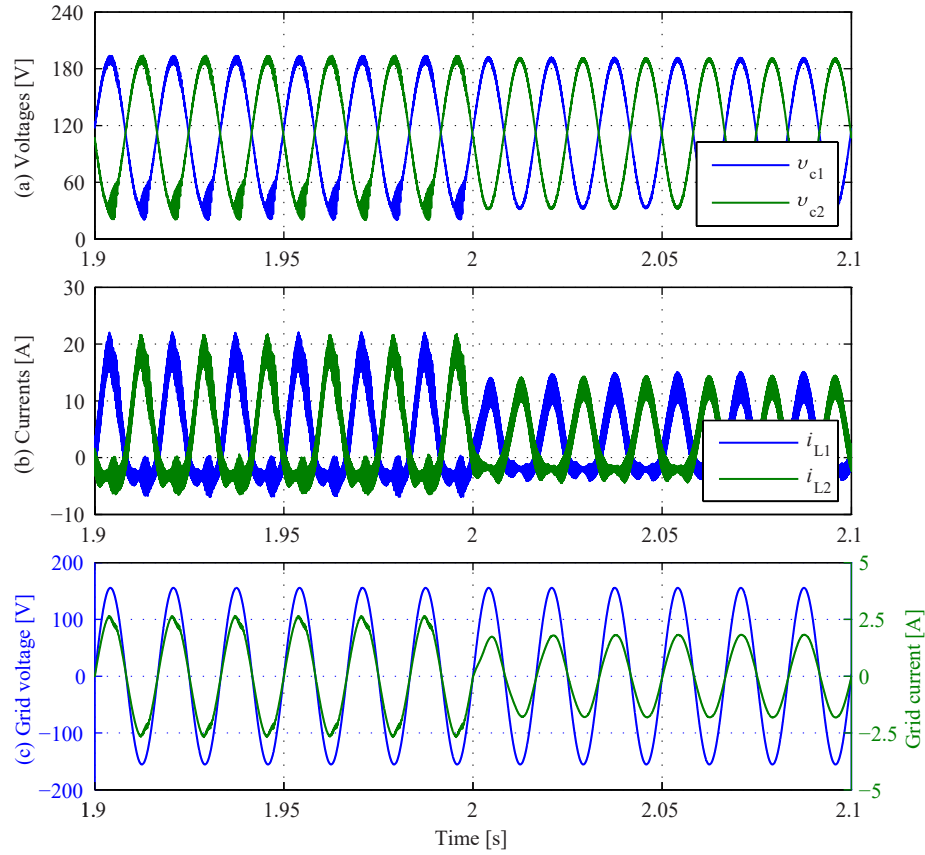


Figure 3.15. Dynamic results of linear control for DBI: (a) Capacitor voltages, (b) inductor currents, and (c) grid voltage and current.

3.2.6 Discussion

The linear control for the DBI based on the approach presented by Sanchis [70] was validated. In this case, the PR controllers are used in the control scheme to regulate the capacitor voltage and the current inductor for each boost converter. The linear control strategy is based on the averaged model of the boost converter considering a variable operation of the inverter. For this reason, several considerations and compensations are introduced in the cascaded control scheme. Despite the fact that good tracking of the capacitor voltages and inductor currents are achieved, the design and the adjust of parameters of the PR controller are not easy tasks. Also, the capacitor voltages and inductor currents present some oscillations around the positive and negative peaks of the waveforms at nominal power. However, the THD and the harmonics of the grid current are within the standard ranges.

3.3 Control strategy based on Finite Control Set-Model Predictive Control for DBI

One non-linear technique employed to control the DBI is based on Finite Control Set-Model Predictive Control (FCS-MPC) algorithm. The main advantages of this strategy are the easy inclusion of non-linearities, and that cascade control loops in specific cases or modulation techniques are not required. In power converters, the main approach of FCS-MPC is to determine a suitable control action S , which moves the variables of interest $y(t)$ to a desired reference $y^*(t)$, considering the future behavior of these variables [67]. Therefore, the discrete model of the power converter and an optimization process are needed.

In the ideal case, the model of the system is used to predict the behavior of the interest variables in a finite prediction horizon, and the control actions are determined through the cost function in each sampling period T_s . However, measurements of the variables, computations of the future behavior and control actions can not be done in the same period of time. To solve this issue, a two-step prediction model has been proposed, as shown in Fig. 3.16, in which the control action is applied in the second sampling period. For further details, see [71].

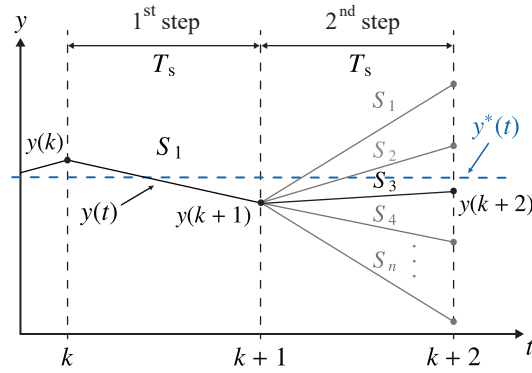


Figure 3.16. Operating principle of FCS-MPC [71].

The general control diagram of the DBI is based on two cascaded control loops, as shown in Fig. 3.17. The first control loop is composed by the maximum power point tracking (MPPT) method of the PV panel and PI regulator for the energy of the input capacitor. Then, the Model Predictive Control strategy is employed in the second control loop for the inductor currents and capacitor voltages.

3.3.1 Control of the input capacitor energy

The first stage of the control scheme based on FCS-MPC consists of the perturb and observe (P&O) algorithm to extract the maximum power from the PV panel and generate the PV voltage reference. Also, a notch filter is implemented to eliminate the second harmonic from the PV voltage feedback, which could enter the control loop, generating a third harmonic component in the reference current. Then, the output of the input capacitor energy controller is the active power reference which is used in the next loop.

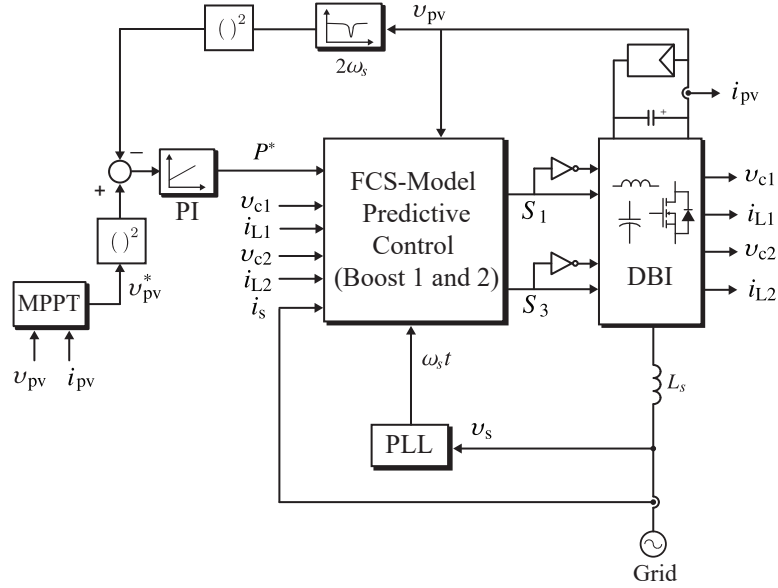


Figure 3.17. The control scheme of the FCS-MPC for the grid-connected DBI.

3.3.2 FCS-Model Predictive Control for DBI

To control the current inductor, and voltage capacitor of each DC-DC converter, the FCS-Model Predictive Control is implemented. For this purpose, three different approaches are analyzed; predictive model of DBI, implemented algorithm and optimization algorithm (cost function).

3.3.2.1 Predictive model of DBI

In order to obtain the discrete model of the inverter, Taylor series truncated at the second degree are used. For simplification, the control equations are given only one boost converter (notations with subscript 1). The other boost converter will be similar with the difference in the sign of the output current as it can be observed in (3.1.2) and (3.1.4). Therefore, the discrete model of one boost converter can be written as

$$i_{L1}(k+1) = i_{L1}(k) + T_s \left. \frac{di_{L1}}{dt} \right|_k + \frac{T_s^2}{2} \cdot \left. \frac{d^2 i_{L1}}{dt^2} \right|_k \quad (3.3.1)$$

$$v_{c1}(k+1) = v_{c1}(k) + T_s \left. \frac{dv_{c1}}{dt} \right|_k + \frac{T_s^2}{2} \cdot \left. \frac{d^2 v_{c1}}{dt^2} \right|_k \quad (3.3.2)$$

where, $i_{L1}(k)$ is the measurement of the inductor current L_1 , $v_{c1}(k)$ is the measurement of the capacitor voltage C_1 , and the first and second derivatives of each variable are obtained from (3.1.1) and (3.1.2).

$$\left. \frac{di_{L1}}{dt} \right|_k = \frac{1}{L_1} [v_{pv} - S_1 v_{c1}(k)] \quad (3.3.3)$$

$$\left. \frac{d^2 i_{L1}}{dt^2} \right|_k = -\frac{1}{L_1} S_1 \left. \frac{dv_{c1}}{dt} \right|_k \quad (3.3.4)$$

$$\left. \frac{dv_{c1}}{dt} \right|_k = \frac{1}{C_1} [S_1 i_{L1}(k) + i_s(k)] \quad (3.3.5)$$

$$\left. \frac{d^2 v_{c1}}{dt^2} \right|_k = \frac{1}{C_1} \left[S_1 \left. \frac{di_{L1}}{dt} \right|_k + \left. \frac{di_s}{dt} \right|_k \right] \quad (3.3.6)$$

Note that, the first derivative of grid current is obtained from (3.1.5).

3.3.2.2 Algorithm of FCS-Model Predictive Control for DBI

The flow diagram of the two-step prediction algorithm is shown in Fig. 3.18, which is described as follows:

- In the sampling time k , the switching states are obtained, and the measurements of the inductor currents, capacitor voltages and output current are made. Also, the previously computed control actions are applied.
- Then, the capacitor voltages and inductor currents references are calculated. The voltage references are obtained through the same analysis used in the linear control strategy, which is based on model of the grid connection of the DBI. Therefore, the voltage references are determined as following,

$$v_{c1}^* = V_{DC} + \frac{V_s}{2} \sin \left(\omega_s t + \frac{2P^* \omega_s L_s}{V_s V_o} \right) \quad (3.3.7)$$

$$v_{c2}^* = V_{DC} - \frac{V_s}{2} \sin \left(\omega_s t + \frac{2P^* \omega_s L_s}{V_s V_o} \right) \quad (3.3.8)$$

where, P^* is the active power reference, which is obtained from the output of the input capacitor energy controller, and the DC voltage component V_{DC} is calculated as (3.2.13). For more information, please see the section 3.2.3.

Furthermore, the inductor current references are derived from (3.1.2) and (3.1.4). Hence, the current references are calculated as,

$$i_{L1}^*(k) = \left[\left(\frac{V_s}{2} \right) C_1 \cdot \omega_s \cdot \cos(\omega_s k + \delta) + i_s^* \right] \cdot \frac{v_{c1}^*}{v_{pv}} \quad (3.3.9)$$

$$i_{L2}^*(k) = \left[- \left(\frac{V_s}{2} \right) C_2 \cdot \omega_s \cdot \cos(\omega_s k + \delta) - i_s^* \right] \cdot \frac{v_{c2}^*}{v_{pv}} \quad (3.3.10)$$

Notice that the control of each boost converter is coupled through the current and voltage references for grid-connected dual boost inverter.

- The derivatives of (3.3.3) - (3.3.6) are calculated in this section to find the first prediction ($k + 1$).

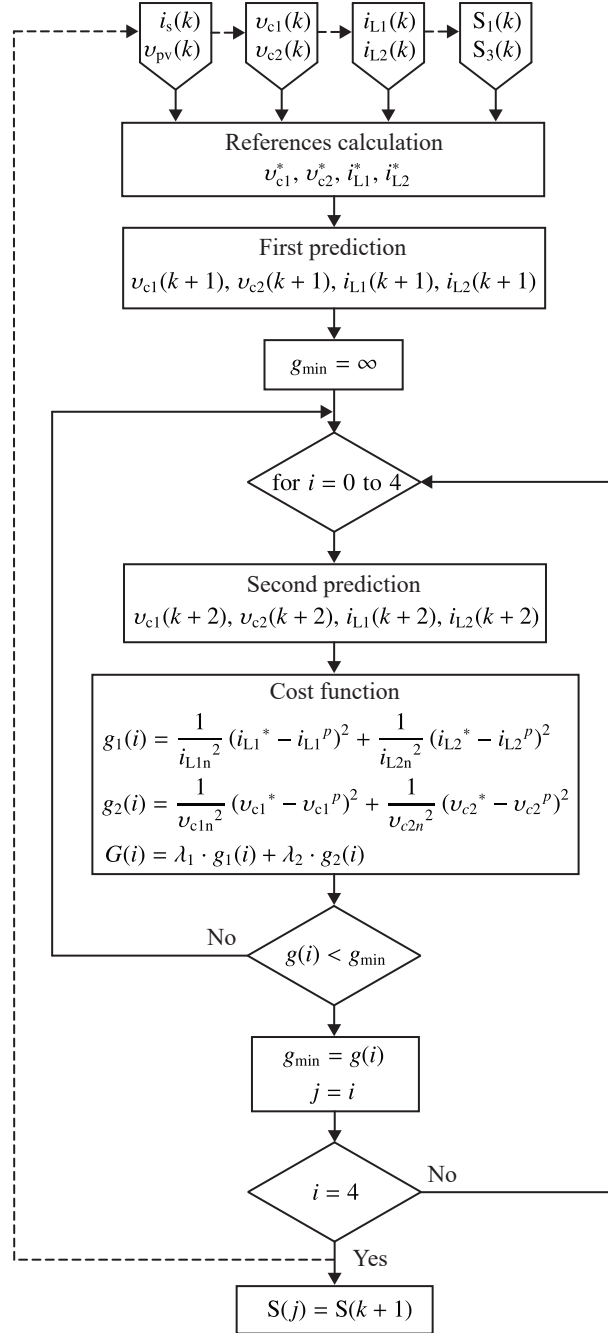


Figure 3.18. Flow diagram for the inductor currents, and the capacitor voltages control.

- Then, the current and voltage in the sampling time $k + 2$ are generated based on the first prediction. For one boost converter, the second predictions are

$$i_{L1}(k+2) = i_{L1}(k+1) + T_s \left. \frac{di_{L1}}{dt} \right|_{(k+1)} + \frac{T_s^2}{2} \left. \frac{d^2 i_{L1}}{dt^2} \right|_{(k+1)} \quad (3.3.11)$$

$$v_{c1}(k+2) = v_{c1}(k+1) + T_s \left. \frac{dv_{c1}}{dt} \right|_{(k+1)} + \frac{T_s^2}{2} \left. \frac{d^2 v_{c1}}{dt^2} \right|_{(k+1)} \quad (3.3.12)$$

- Finally, the predictions calculated in the previous stages are used in the minimization process. In this method, the current and voltage quadratic errors are employed. The predictions in $k + 2$ are compared to the references and the option that is closer to the reference is selected (Optimization process). This value becomes the next switching state to be applied during the interval between $(k + 1)$ and $(k + 2)$.

3.3.2.3 Optimization algorithm

In power systems, the most common optimization algorithm $G(k)$ based on the quadratic error between the predictions and references is used to evaluate the performance of the control strategy and to select the best control actions with a minimum cost, as shown in (3.3.13).

$$G(k) = \sum_{l=k}^{k+N-1} \|(l+1) - y^*(l+1)\|^2 \quad \text{for } l \in k, \dots, k+N-1 \quad (3.3.13)$$

For the DBI, the control targets are the inductor current and the capacitor voltage for each boost converter. The units of these variables are different, for this reason it is important to normalize the cost function with coefficients that are the nominal values of the variables [72]. Therefore, the global structure of the cost function has two components,

$$G = \lambda_1 \cdot g_1 + \lambda_2 \cdot g_2 \quad (3.3.14)$$

where,

$$g_1 = \frac{1}{i_{L1n}^2} (i_{L1}^* - i_{L1}^p)^2 + \frac{1}{i_{L2n}^2} (i_{L2}^* - i_{L2}^p)^2$$

$$g_2 = \frac{1}{v_{c1n}^2} (v_{c1}^* - v_{c1}^p)^2 + \frac{1}{v_{c2n}^2} (v_{c2}^* - v_{c2}^p)^2$$

g_1 is the quadratic error of the inductor currents, g_2 is the quadratic error of the capacitor voltages and, λ_1 and λ_2 are the weight factors, which can determine the degree of relevance of each variable in the process. In this case, the main goal is the capacitor voltage and the second goal is the inductor current. Therefore, the weight factor λ_2 is higher than λ_1 . The weight factors were obtained by empirical procedure, which are: $\lambda_1 = 1$ and $\lambda_2 = 75$.

3.3.3 Simulation results of FCS-MPC for DBI

In order to validate the FCS-Model Predictive Control, the DBI with PV panel as input source is simulated. The main parameters of the panel, the inverter and control are shown in the Table 3.5.

Table 3.5. Simulation parameters of the FCS-Model Predictive Control of DBI.

Symbol	Parameter	Value
PV Parameters		
V_{mpp}	PV voltage at MPP	29 V
P_{pv}	PV power	216 W
C_{pv}	Input capacitor	25 mF
Grid Parameters		
v_s	Grid voltage	110 V_{rms}
f_s	Grid frequency	60 Hz
L_s	Grid filter inductance	10 mH
Converter Parameters		
L_1, L_2	Boost converters inductors	55 μ H
C_1, C_2	Boost converters capacitors	25 μ F
Control Parameters		
T_s	Sampling time	5 x 10e-6 s
k_p^{PV}	Proportional gain of PI (PV voltage control)	4
k_i^{PV}	Integral gain of PI (PV voltage control)	50
k_p^P	Proportional gain of PI (Active power control)	1 x 10e-7
k_i^P	Integral gain of PI (Active power control)	1 x 10e-2
k_p^Q	Proportional gain of PI (Reactive power control)	5 x 10e-5
k_i^Q	Integral gain of PI (Reactive power control)	0.2

One important consideration is that the dynamic behavior of the converter was evaluated with a solar irradiance change. The initial solar irradiance is 1000 W/m², which is reduced to 700 W/m² at time $t = 2.0$ s.

The first simulation results present the steady-state behavior of the DBI for each solar irradiance case (1000 and 700 W/m²). Then, dynamic performance of the PV panel and inverter are presented when the solar irradiation change is made.

For the level of solar irradiances used in this section, the corresponding PV power values are 216 W and 150 W. The figures 3.19 and 3.21 show the capacitor voltages, inductor currents, and grid voltage and current of the inverter in steady-state for each PV power value.

For input power of 216 W, the voltage of the capacitors with their references are shown in Fig. 3.19(a), which are composed of DC and AC components. The DC component for these signals is the same (110 V). The amplitudes in the two converters are 77.79 V, and the phases are shifted 180°. The current of the inductors with their references are illustrated in Fig. 3.19(b), where it is possible to identify that the currents are not sinusoidal and present a negative part. The phases are shifted 180°, which is a similar effect observed in the voltage.

In order to show the same variables of the previous case in an appropriate scale, three cycles of each variable are presented in Fig. 3.21 for the input power of 150 W. The capacitor voltages are shown at the top of this figure, where it is possible to identify that the behavior

of these voltages is the same observed in the 210 W of input power. As it can be seen in Fig. 3.21(b), the amplitude of the inductor currents decreases because the input power is reduced.

The grid results are illustrated in Fig. 3.19(c) and 3.21(c), where the grid voltage and current are presented. In both cases, the grid voltage is a pure sinusoidal and the same at any period of time. However, the amplitude of the grid current is different for each PV power level. In the nominal operation, the amplitude of the current is 2.7 A, which is reduced at 1.8 A, when the solar irradiance changed. The waveform of the grid current is very close to a sinusoidal and in phase with the grid voltage.

The power quality of the DBI is analyzed through the spectrum and total harmonic distortion (THD) of the grid current. These results are shown in Fig. 3.20 and 3.22. Notice that, the limits of the IEEE standard 1547 are presented in another color in the figures to identify the ranges. As it can be observed, the harmonics of the grid current for both PV power level are within accepted ranges by the standard. THD for nominal power is 3.58 %, but this value increases at 3.73 %, when the PV power decreases, as expected. These are very good results, considering that the waveform of the currents has appreciable oscillations.

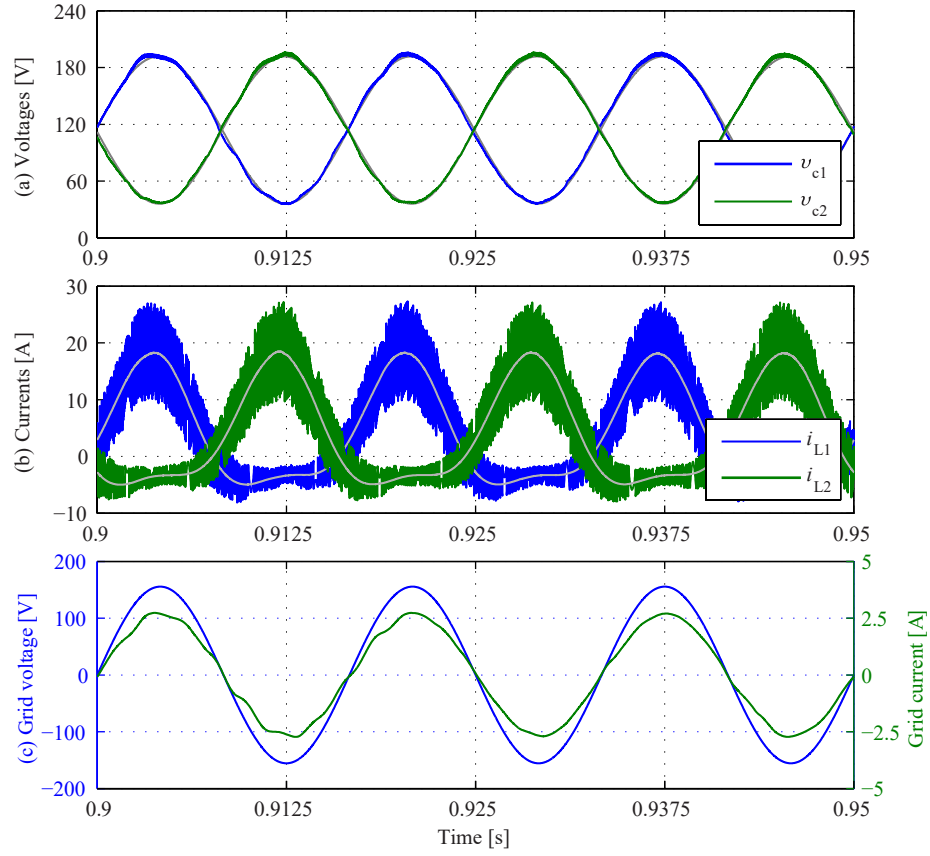


Figure 3.19. Steady-state results of FCS-Model Predictive Control for DBI at 216 W of PV power: (a) Capacitor voltage of each boost converter, (b) inductor current of each boost converter, and (c) grid voltage and current.

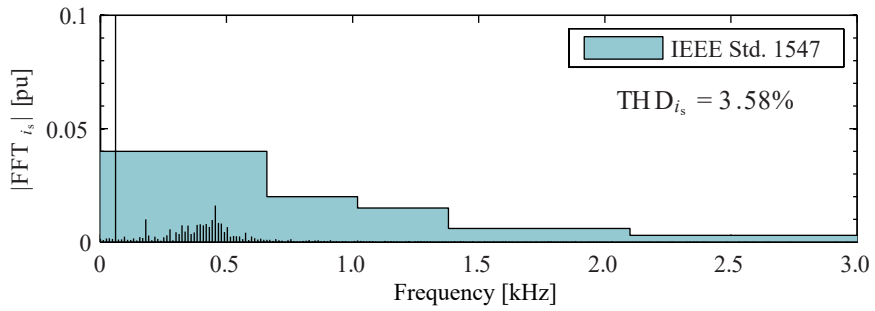


Figure 3.20. Grid current spectrum of DBI with FCS-Model Predictive Control at 216 W of PV power.

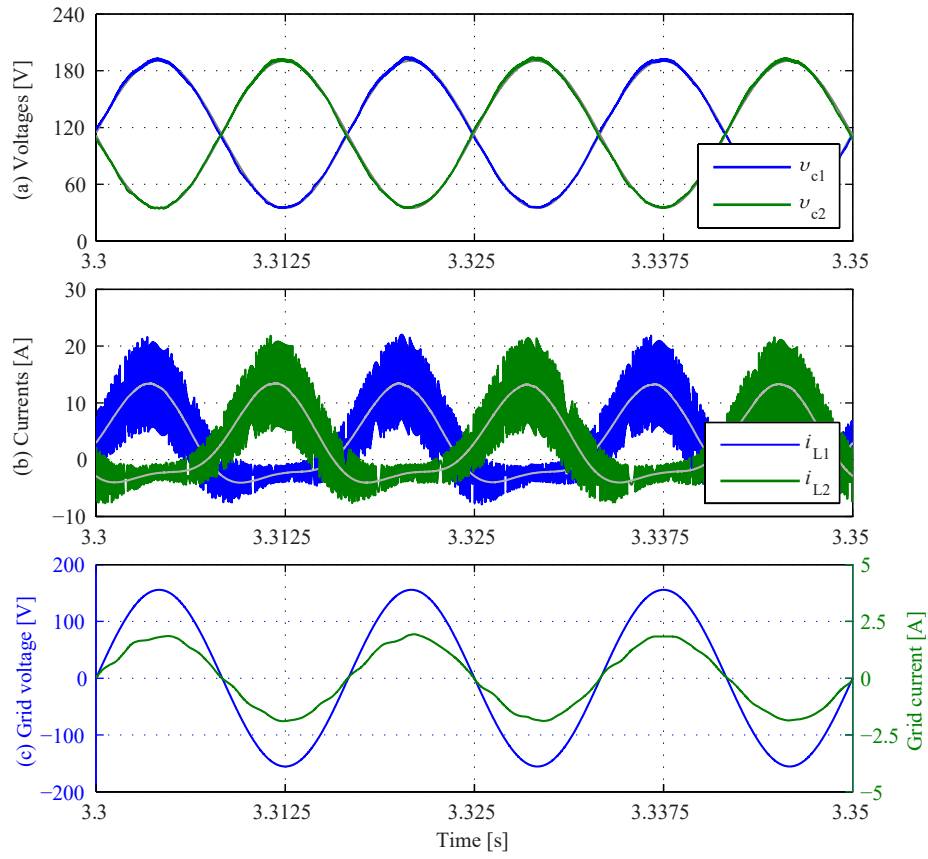


Figure 3.21. Steady-state results of FCS-Model Predictive Control for DBI at 150 W of PV power: (a) Capacitor voltage of each boost converter, (b) inductor current of each boost converter, and (c) grid voltage and current.

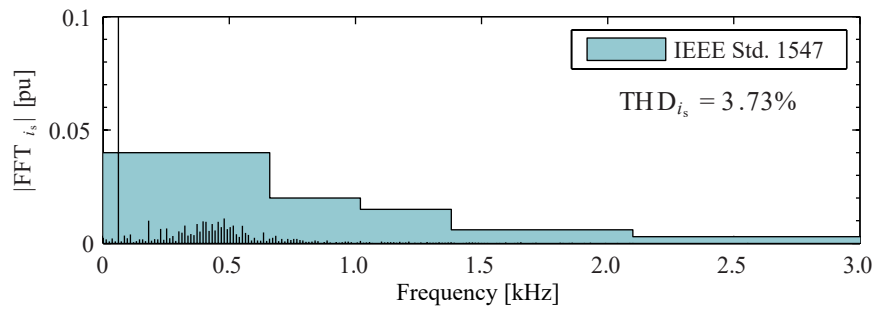


Figure 3.22. Grid current spectrum of DBI with FCS-Model Predictive Control at 150 W of PV power.

In order to evaluate the dynamic performance of the control, a step-down in the solar irradiance is made at time of 2.0 s. The PV side and the inverter results are illustrated in Fig. 3.23 and 3.24.

The PV voltage and its reference are shown in Fig. 3.23(a). In this figure, it is possible to identify the three voltage levels due to the MPPT algorithm. When the solar irradiance changes, the PV current decreases from 7.5 A to 5.23 A, as shown in 3.23(b). Note that, the input power also decreases, as observed in Fig. 3.23(c).

The capacitor voltages (v_{c1} and v_{c2}) are presented in Fig. 3.24(a). It can be observed that the voltage levels are kept constant in both input power. On the other hand, the amplitude of the inductor currents (i_{L1} and i_{L2}) is reduced when the step-down of solar irradiance is produced. As a result of this variation, the amplitude of the grid current also decreases (See Fig. 3.24). In these figures, it can be observed a quick transient response.

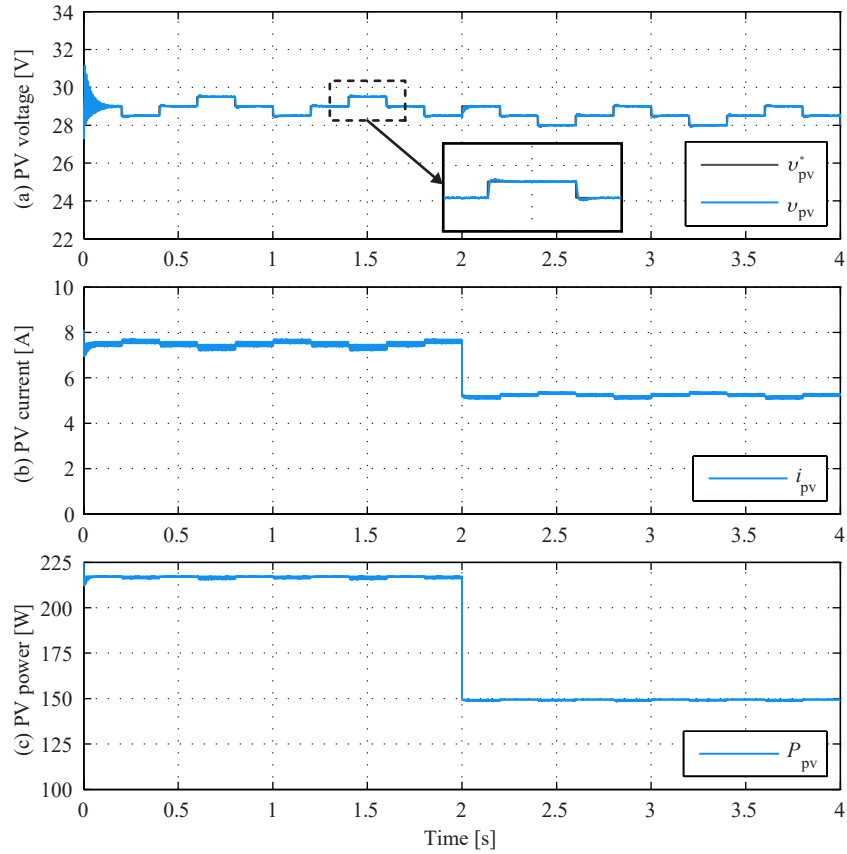


Figure 3.23. Dynamic results of FCS-Model Predictive Control for DBI: (a) PV voltage, (b) PV current, and (c) PV power.

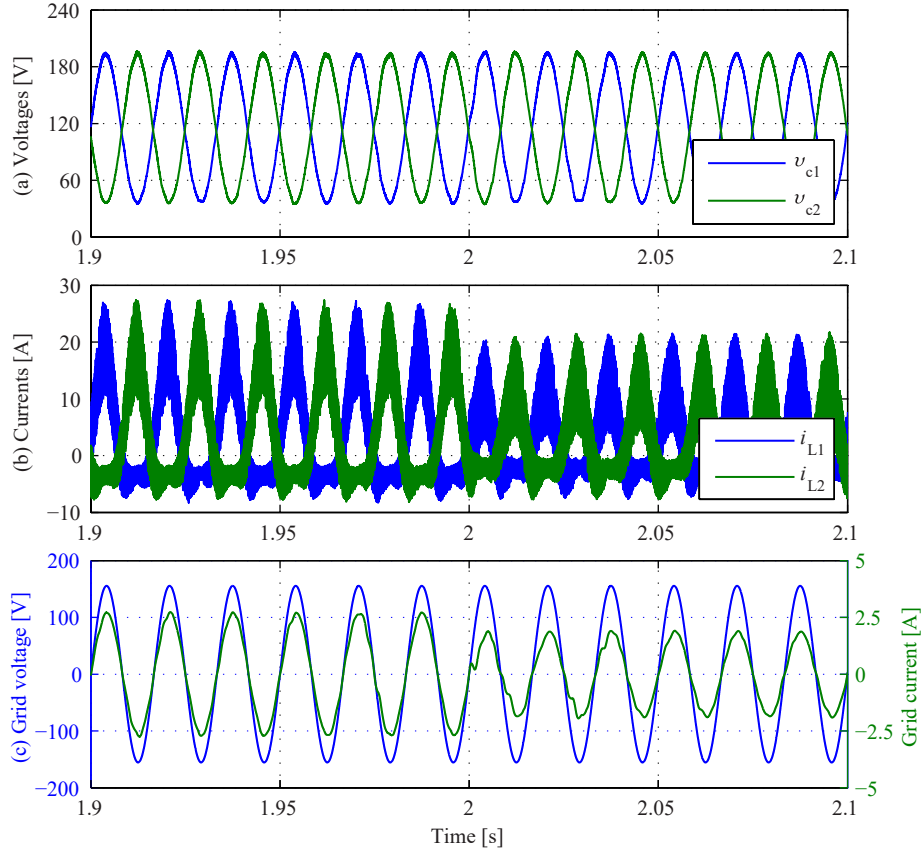


Figure 3.24. Dynamic results of FCS-Model Predictive Control for DBI: (a) Capacitor voltage of each boost converter, (b) inductor current of each boost converter, and (c) grid current and voltage.

3.3.4 Discussion

In this section, the FCS-Model Predictive Control for the grid-connection of the dual boost inverter is proposed. In this algorithm, the linearization process of the system is not necessary, because the control of the inductor currents and the capacitor voltages were made with predictions of these variables based on the inverter model. This feature allows to obtain a simple control structure.

However, the switching frequency of the semiconductor devices is variable, as it can be identified in the inductor currents. This confirms the main drawback of the FCS-MPC strategy, which generates high switching losses.

Another important aspect to mention is the selection of the weight factors. The control objectives of the DBI present different dynamics and variation range, which makes the determination of the weight factors a difficult task. In this case, the weight factor is selected

as the best trade off between the tracking of the capacitor voltage and the THD of the grid current. The tracking of the capacitor voltage presents some oscillations, but the harmonics and THD of the output current comply with the standard.

3.4 Flatness-based control for DBI

The flat systems have been introduced by Flies *et. al* [73], which are based on the differential algebra. A system is differentially flat, if the structure of the trajectories and their dynamics are completely represented through a fictitious variable, called flat output [74]. The main feature of differential flat system is that the state and input variables of the non-linear system can be expressed through a flat output and a finite number of its derivatives, without employing any differential equation [75].

The non-linear system as,

$$\dot{x} = f(x, u) \quad (3.4.1)$$

where $x \in R^m$, $u \in R^n$, is differentially flat, if there is a flat output y of dimension m , such as,

$$y = (y_1, y_2, \dots, y_m) = \phi(x, u, \dot{x}, \dots, u^{(s)}) \quad (3.4.2)$$

$$x = \varphi(y, \dot{y}, \dots, y^{(r)}) \quad (3.4.3)$$

$$u = \psi(y, \dot{y}, \dots, y^{(r+1)}) \quad (3.4.4)$$

where r and s are integers, $\varphi \in (R^m)^{r+1} \rightarrow R^m$, and $\psi \in (R^m)^{r+2} \rightarrow R^n$. Therefore, the dynamic behavior of the system is represented through its flat output mapping in the simple space, without integrating any differential equation, as shown in Fig. 3.25. More information of the flatness theory and its applications can be found in [76] and [77].

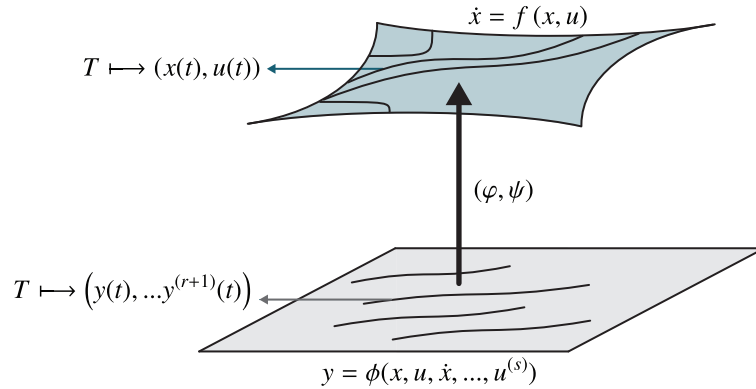


Figure 3.25. General concept of flatness system by Levine [77].

For the dual boost inverter, the control strategy is based on differential flatness theory. The control scheme is shown in Fig. 3.26, which is composed by two cascaded control loops. The voltage reference v_{pv}^* of the outer control loop is obtained from the classical perturb and observe P&O MPPT algorithm. The input capacitor energy error is regulated using a PI controller, as shown in section 3.2.2. Then, the active power reference obtained from the previous loop is employed to calculate the output voltage reference of each boost converter for the next control loop. The inner control loop, based on flatness theory, regulates the output voltage of each boost converter, which is indirectly accomplished through the regulation of energy stored. Finally, the switching signals are obtained through a PWM scheme.

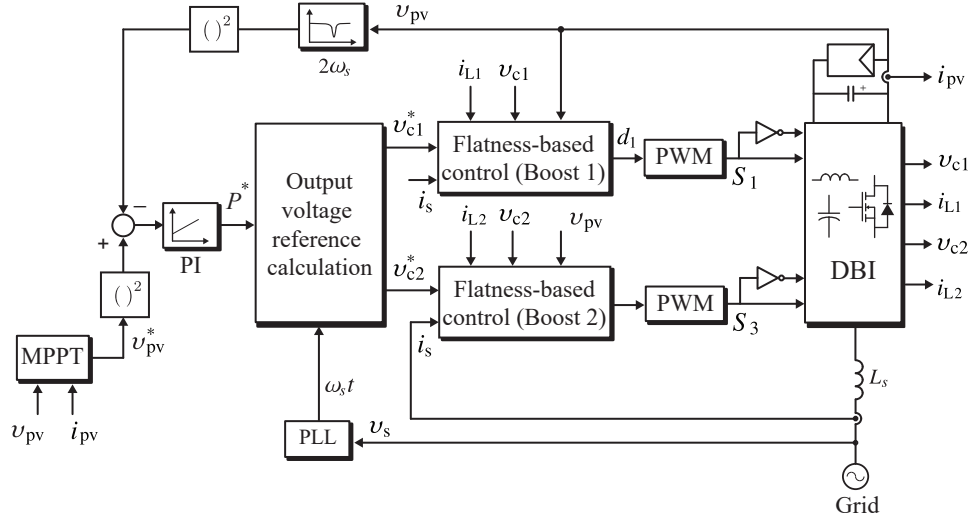


Figure 3.26. Control scheme of the flatness-based control for DBI.

3.4.1 Output voltage reference calculation

The voltage references are obtained through the complex phasor analysis shown previously in subsection 3.2.3. In this case, an indirect power control is proposed, where the phase angle calculation is based on the active power equation shown in (3.2.9). Hence, the capacitor voltage references are written as,

$$v_{c1}^* = V_{DC} + \frac{V_s}{2} \sin \left(\omega_s t + \frac{2P^* \omega_s L_s}{V_s V_o} \right) \quad (3.4.5)$$

$$v_{c2}^* = V_{DC} - \frac{V_s}{2} \sin \left(\omega_s t + \frac{2P^* \omega_s L_s}{V_s V_o} \right) \quad (3.4.6)$$

where the DC voltage V_{DC} reference is calculated with the same approach illustrated in the linear control section (see (3.2.13)). Note that, the reactive power flow is not considered.

3.4.2 Flatness-based control of the individual DC-DC converter

As mentioned before, the differential flatness theory is used to regulate the output voltage of each boost converter.

The proposed control scheme considers an independent control for each boost converter. Due to the symmetry of the inverter, detailed equations have been provided only for boost converter 1. To analyze the flatness propriety of the boost converter, the chosen candidate flat output is the stored energy through the converter [74, 78], it can be written as

$$y_1 = \frac{1}{2} L_1 i_{L1}^2 + \frac{1}{2} C_1 v_{c1}^2 = \phi(i_{L1}, v_{c1}) \quad (3.4.7)$$

Considering the system described in (3.1.1) and (3.1.2), the derivative of y_1 is

$$\dot{y}_1 = i_{L1} v_{pv} - i_s v_{c1} \quad (3.4.8)$$

In order to verify the flatness theory it is necessary to find the following conditions,

$$i_{L1} = \varphi_{i_{L1}}(y_1, \dot{y}_1) \quad (3.4.9)$$

$$v_{c1} = \varphi_{v_{c1}}(y_1, \dot{y}_1) \quad (3.4.10)$$

$$d_1 = \psi_1(y_1, \dot{y}_1, \ddot{y}_1) \quad (3.4.11)$$

Considering the flat output and its derivative, the inductor current i_{L1} can be calculated

$$i_{L1} = \frac{-\left(\frac{C_1 v_{pv} \dot{y}_1}{i_s^2}\right) + \sqrt{\left(\frac{C_1 v_{pv} \dot{y}_1}{i_s^2}\right)^2 - \left(L_1 + \frac{C_1 v_{pv}^2}{i_s^2}\right) \left(\frac{C_1 \dot{y}_1^2}{i_s^2} - 2y_1\right)}}{L_1 + \frac{C_1 v_{pv}^2}{i_s^2}} = \varphi_{i_{L1}}(y_1, \dot{y}_1) \quad (3.4.12)$$

In order to obtain the output voltage v_{c1} as function of the energy y_1 and its derivative, the equations (3.4.7) and (3.4.12) are considered. Therefore, the output voltage can be written as

$$v_{c1} = \sqrt{\frac{2y_1 - L_1 [\varphi_1(y_1, \dot{y}_1)]^2}{C_1}} = \varphi_{v_{c1}}(y_1, \dot{y}_1) \quad (3.4.13)$$

Finally, considering the second derivative of the energy \ddot{y}_1 , it is possible to calculate d_1 as

$$d_1 = \frac{\ddot{y}_1 - \frac{v_{pv}^2}{L_1} + \frac{v_{pv}}{L_1} \varphi_{v_{c1}}(y_1, \dot{y}_1) + \frac{i_s}{C_1} \varphi_{i_{L1}}(y_1, \dot{y}_1) - \frac{i_s^2}{C_1}}{\frac{i_s}{C_1} \varphi_{i_{L1}}(y_1, \dot{y}_1) + \frac{v_{pv}}{L_1} \varphi_{v_{c1}}(y_1, \dot{y}_1)} = \psi_1(y_1, \dot{y}_1, \ddot{y}_1) \quad (3.4.14)$$

From (3.4.12), (3.4.13), and (3.4.14), it is evident that all variables can be expressed as a function of the flat output and its derivatives without solving any differential equations. Then, the system is flat, and it is possible to indirectly control all the variables through a control of y_1 .

To ensure reference tracking, a third order control law is proposed:

$$k_1(y_1^* - y_1) + k_2 \int (y_1^* - y_1) dt + k_3(\dot{y}_1^* - \dot{y}_1) + k_4(\ddot{y}_1^* - \ddot{y}_1) = 0 \quad (3.4.15)$$

The constants k_1 , k_2 , k_3 and k_4 are calculated as following,

$$\begin{aligned} k_1 &= 2 \cdot \xi \cdot \omega_n \cdot p + \omega_n^2 \\ k_2 &= p \cdot \omega_n^2 \\ k_3 &= 2 \cdot \xi \cdot \omega_n + p \\ k_4 &= 1 \end{aligned}$$

where, ξ is the damping factor, ω_n is the pulsation and p is the value of one pole.

Solving (3.4.15), it is possible to find the second derivative of the energy as

$$\ddot{y}_1 = \ddot{y}_1^* + k_1(y_1^* - y_1) + k_2 \int (y_1^* - y_1) dt + k_3(\dot{y}_1^* - \dot{y}_1) \quad (3.4.16)$$

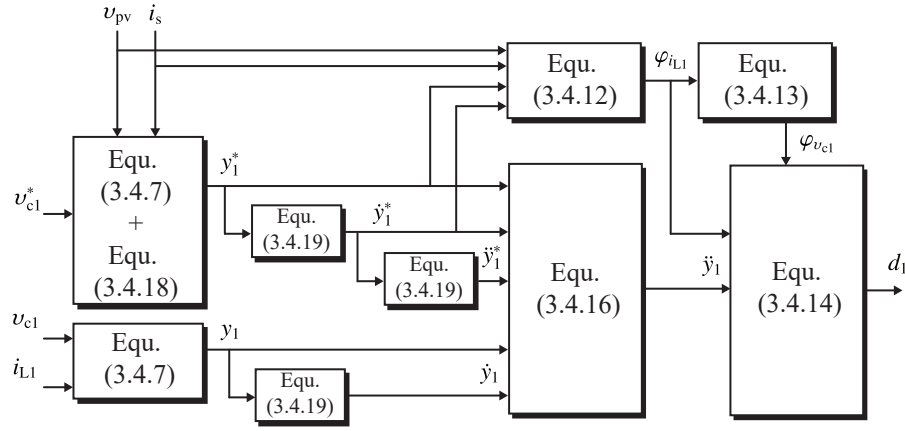


Figure 3.27. Control scheme of flatness-based control for boost converter 1.

The Fig. 3.27 illustrates the general implementation of the flatness-based control. The reference of the energy is based on (3.4.7) and the power balance between the input and output of each boost converter, as shown below

$$P_{in} = P_{out} \quad (3.4.17)$$

$$i_{L1}^* = \frac{v_{c1}^* \cdot i_s}{v_{pv}} \quad (3.4.18)$$

On the other hand, the derivative of the signals is calculated through the approximation shown in (3.4.19), where β is a constant between 10 to 20 [79]. Also, it is possible to observe that a pole is introduced in the transfer function of the derivative to avoid problems by measurement noise. Note that, the transfer function is expressed in Laplace domain for an easy description. However, the derivative is implemented by its discrete version.

$$G_D(s) = \frac{T_D s}{1 + \frac{T_D}{\beta} s} \quad (3.4.19)$$

3.4.3 Simulation results of the flatness-based control for DBI

In order to validate the flatness-based proposed control, the dual boost inverter with a PV panel as input source has been simulated. The main parameters of the DBI and its control are listed in the Table 3.6.

The steady-state operation of the grid-connected DBI is presented for two different input powers (two operation points), i.e the 216 W of nominal power and 150 W. The figures 3.28 and 3.30 show the capacitor voltage, the inductor current of each boost converter, and the grid voltage and current.

The capacitor voltages are shown in Fig. 3.28(a) and 3.30(a) for two operation points, respectively. For both cases, the capacitor voltages are composed of DC and AC components,

Table 3.6. Simulation parameters of the flatness-based control of DBI.

Symbol	Parameter	Value
PV Parameters		
V_{mpp}	PV voltage at MPP	29 V
P_{pv}	PV power	216 W
Grid Parameters		
v_s	Grid voltage	110 V _{rms}
f_s	Grid frequency	60 Hz
L_s	Grid filter inductance	10 mH
Converter Parameters		
C_{pv}	Input capacitor	25 mF
L_1, L_2	Boost converters inductors	55 μ H
C_1, C_2	Boost converters capacitors	5 μ F
Control Parameters		
f_{sw}	Switching frequency	80 kHz
k_p^{PI}	Proportional gain of PI (PV voltage control)	0.2
k_i^{PI}	Integral gain of PI (PV voltage control)	50
ξ	Damping ratio (Flatness-based control)	0.7
ω_n	Pulsation (Flatness-based control)	15000 rad/s
p	pole(Flatness-based control)	4000 rad/s

as expected through the previous analysis. The DC component is around 112.58 V, considering a boost factor of 1.2 in (3.2.13) of the linear control section. Then, the amplitude of AC component is half of the output voltage of the inverter ($110 \cdot \sqrt{2}/2$ V).

To observe the tracking of the capacitor voltages, the Fig. 3.32(a) and 3.32(b) present three periods of these signals for nominal power (216 W). The references and measurements of the capacitor voltages of each DC-DC boost converter are illustrated, where an accurate tracking is verified.

In addition, the inductor current waveforms for both power levels are shown in Fig. 3.28(b) and 3.30(b). The inductor currents present a negative part due to the circulating power. Also, the magnitudes of the DC and AC components are the same for each operation point. Note that, the mean positive amplitude is around 18 A for the nominal power (216 W), while this amplitude is around 13 A for 150 W of input power.

The results in the grid side for both power levels are illustrated in the Fig. 3.28(c) and 3.30(c). It is possible to see that the waveform of the grid current is very close to a sinusoidal, and in phase with the grid voltage. Please note that, the grid voltage does not change in any of the cases. However, the amplitude of the grid current in each operation point is different to keep the power balance. Therefore, the peak amplitude for nominal power and 150 W is 2.52 A and 1.77 A, respectively.

The frequency spectrum and THD of the grid current are shown in Fig. 3.31 and 3.29 for both operation points. To evaluate the power quality of the inverter, the IEEE standard in blue color is used and introduced in the spectrum figure, where it is possible to observe that the ranges of all harmonics are within the standard limits. Note that, the third and fifth harmonic are predominant in both cases. On the other hand, the total harmonic distortion

for two power levels are similar, i.e the THD is 2.59 % for nominal power and 2.36 % for 150 W of input power.

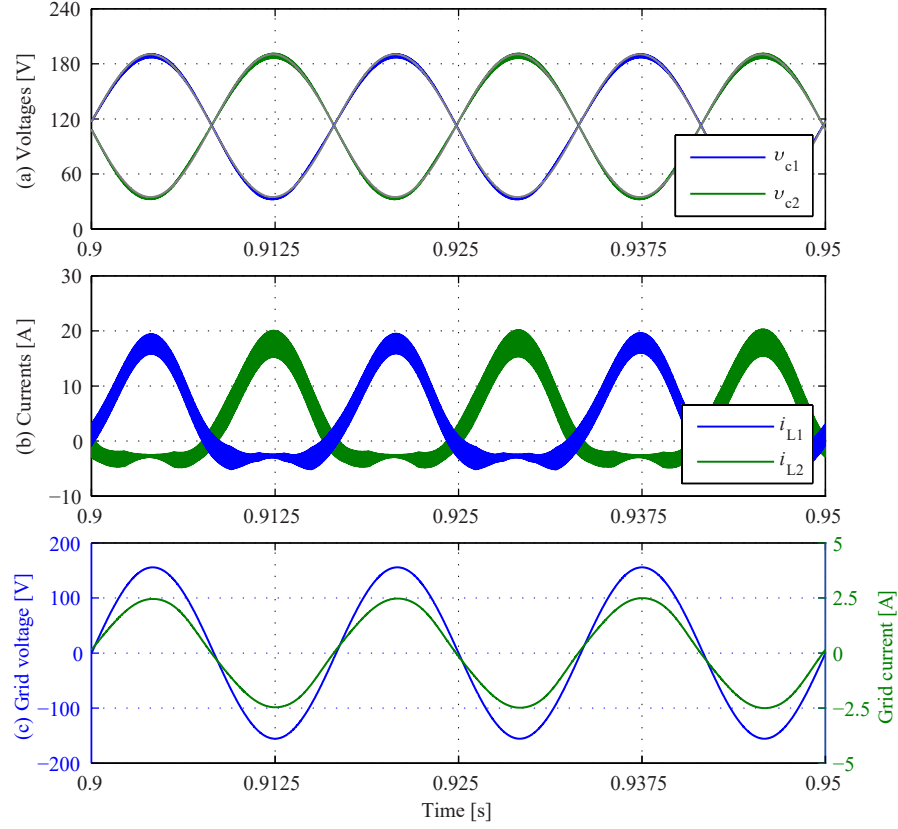


Figure 3.28. Steady-state results of flatness-based control for DBI at 216 W of PV power: (a) Capacitor voltage of each boost converter, (b) inductor current of each boost converter, and (c) grid voltage and current.

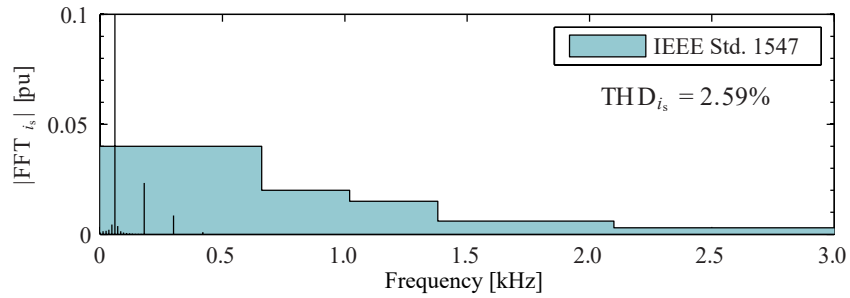


Figure 3.29. Grid current spectrum of DBI with flatness-based control at 216 W of PV power.

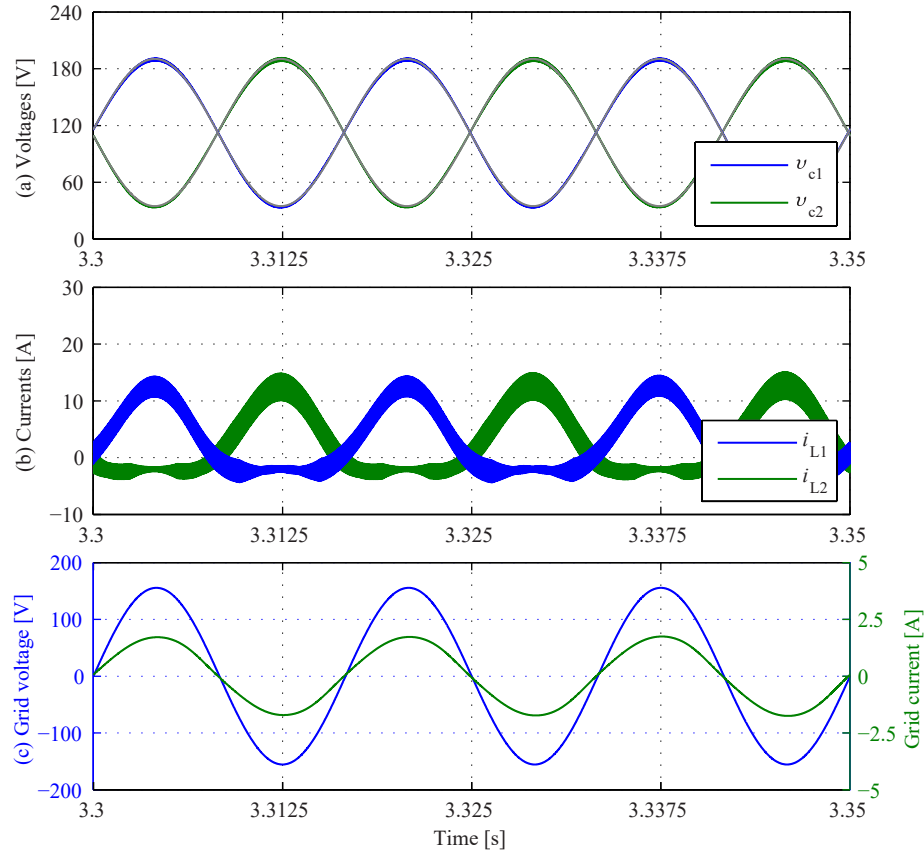


Figure 3.30. Steady-state results of flatness-based control for DBI at 150 W of PV power: (a) Capacitor voltage of each boost converter, (b) inductor current of each boost converter, and (c) grid voltage and current.

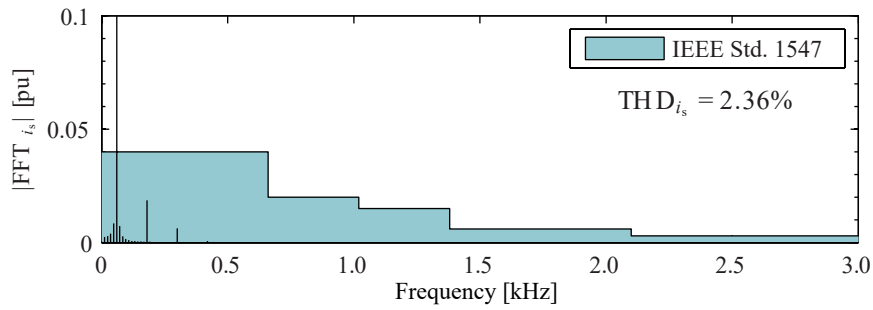


Figure 3.31. Grid current spectrum of DBI with flatness-based control at 150 W of PV power.

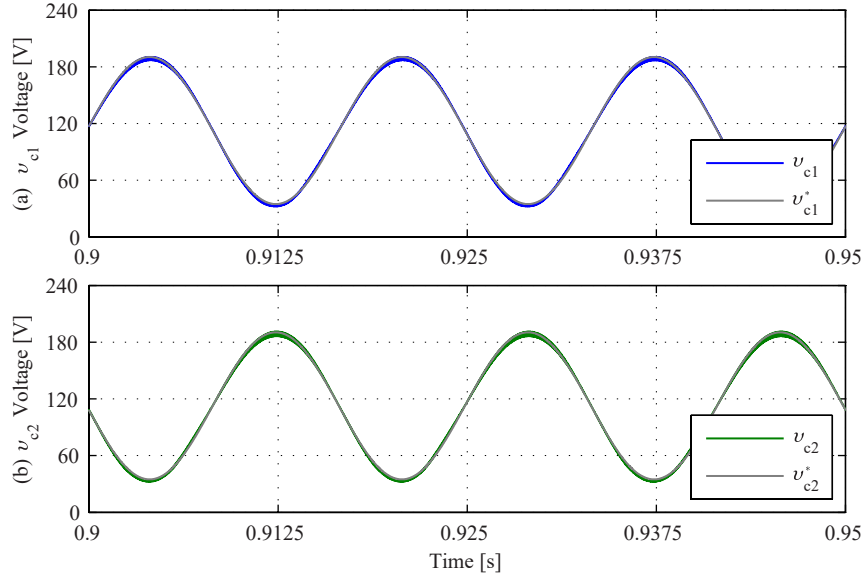


Figure 3.32. Simulations results of the tracking of the capacitor voltages with flatness-based control for DBI at 216 W of PV power: a) Capacitor voltage of the boost converter 1, and b) capacitor voltage of the boost converter 2.

To evaluate the dynamic performance of proposed control, the solar irradiance is reduced from 1000 W/m^2 to 700 W/m^2 at time $t=2.0 \text{ s}$. These values of solar irradiance correspond to the two power levels shown before (216 W and 150 W). In Fig. 3.33, the behavior of the PV side is shown. The PV voltage reference (v_{pv}^*) and the measurement (v_{pv}) are presented in Fig. 3.33(a). Note that, the three voltage levels around the MPP can be identified, when the PV module is operating under uniform solar irradiance.

When the solar irradiance step is made, the PV voltage decreases until it reaches the new maximum power point. On the other hand, the PV current also decreases, as shown in Fig. 3.33(b). And, the input power is reduced, as illustrated in Fig. 3.33(c).

The Fig. 3.34 illustrates the inverter behavior when the solar irradiance step is made. Six periods of the voltages and currents waveforms before and after this step are shown to identify the changes. The amplitude of the capacitor voltages is kept constant all the time, as observed in Fig. 3.34(a). Conversely, the variation of the input power is reflected in the inductor currents (See Fig. 3.34(b)) and in the grid current (See Fig. 3.34(c)). The amplitude of these currents is reduced when the input power is less than the nominal power.

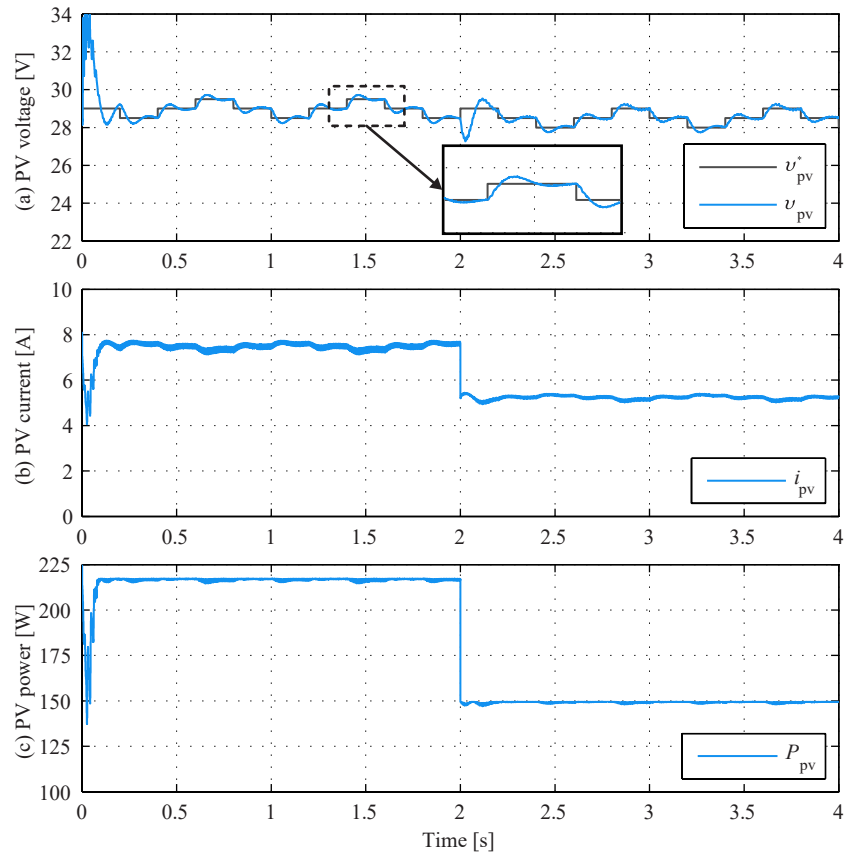


Figure 3.33. Dynamic results of flatness-based control for DBI: (a) PV voltage, (b) PV current, and (c) PV power.

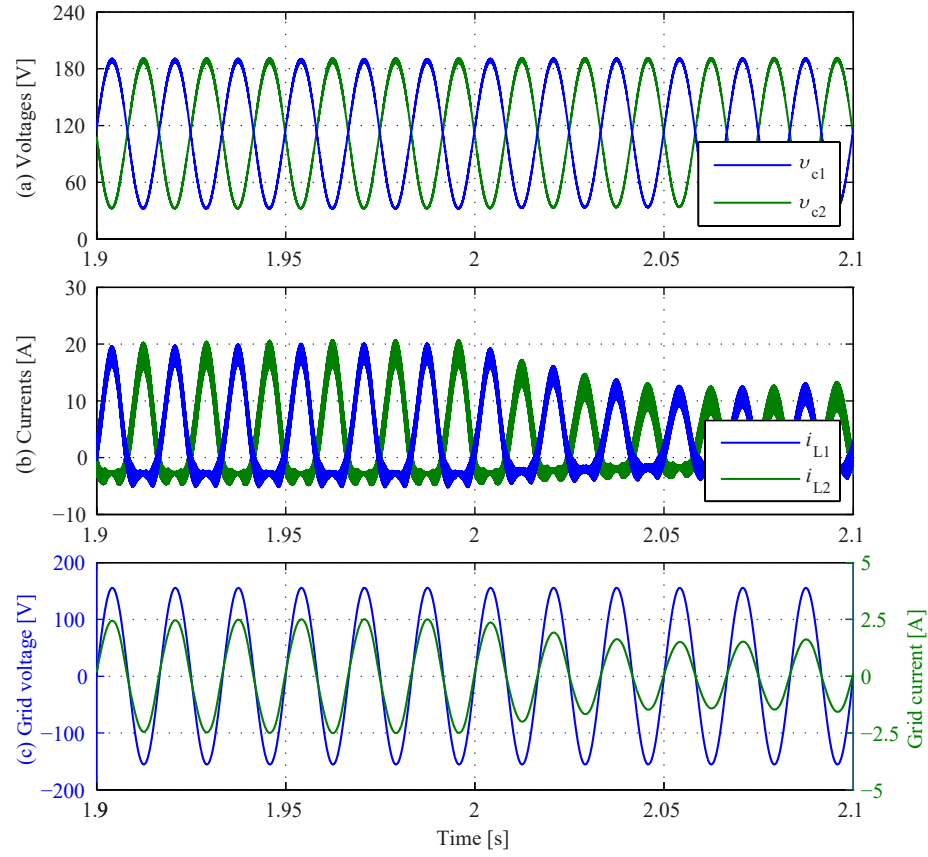


Figure 3.34. Dynamic results of flatness-based control for DBI: (a) Capacitor voltage of each boost converter, (b) inductor current of each boost converter, and (c) grid current and voltage.

3.4.4 Discussion

The flatness-based control strategy for the grid connection of the DBI is proposed and validated through simulations in this section. In this control strategy, each DC-DC converter is controlled individually. The differential flatness theory is used to regulate indirectly the capacitor voltage of each boost converter. The strategy is based on the stored energy control of the inductors and capacitors of the inverter. The control scheme is composed by: the outer control loop that regulates the energy through C_{pv} , the next block calculates the references of capacitor voltages based on the active and reactive power, and the inner control loop that regulates the stored energy of inductor and capacitor of each DC-DC converter.

The main advantage of the proposed control strategy is high dynamic behavior and robustness against parameter disturbances, such as the variation of the input power. Nevertheless, the implementation of the derivative action requires a high computation demand to obtain a good approximation.

3.5 Sliding mode based control for DBI

The sliding mode approach is a control strategy derived from the variable structure system theory, which extends the properties of hysteresis control to multivariable environments, guaranteeing stability and robustness against parameter variations and high regulation dynamics [80] and [81].

To understand the control strategy that has been proposed in this section, a simple example of a second order system is used to introduce the main notions of sliding mode. Hence, the second order system composed by two substructures is analyzed [80]. In Fig. 3.35(a), it can be observed that the eigenvalues of the first structure are complex with zero real part and therefore their phase trajectories are circles. In the second substructure, the eigenvalues are real with opposite sign, which leads to only one phase trajectory that converges toward the origin, as shown in Fig. 3.35(b). In this case, Fig. 3.35(c) presents the phase plane of global system, which is divided in two regions associated to each substructure, where two switching boundaries are identified, one of them is the switching line and the other is the x_2 axis. If a representative point enters in the region delimited by the switching boundaries and hits the switching line, the control law ensures that this point does not move away from the switching line. This motion of representative point along a trajectory is called sliding mode.

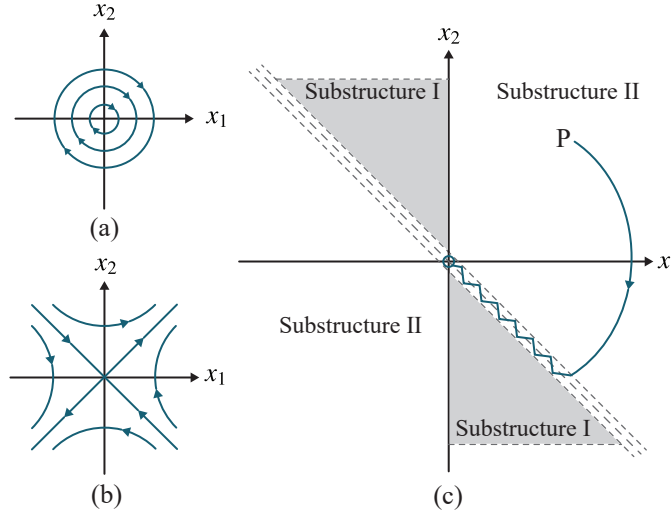


Figure 3.35. (a) Eigenvalues of substructure I, (b) eigenvalues of substructure II, and (c) sliding mode behaviour [80].

In general terms, a system with scalar control can be represented by

$$\dot{\mathbf{x}} = \mathbf{f}(\mathbf{x}, t, u) \quad (3.5.1)$$

where \mathbf{x} is a state vector, \mathbf{f} is a function vector, t is the time vector and u is the input vector. Given a sliding surface as $\sigma(\mathbf{x}, t) = 0$, the system can be rewritten as,

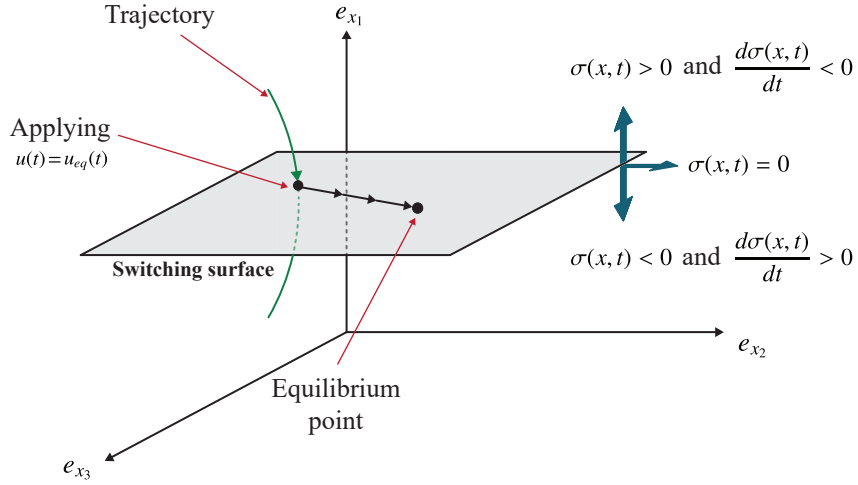


Figure 3.36. General diagram of sliding mode control [82].

$$\mathbf{f}(\mathbf{x}, t, u) = \begin{cases} \mathbf{f}^+(\mathbf{x}, t, u^+) & \text{for } \sigma \rightarrow 0^+ \\ \mathbf{f}^-(\mathbf{x}, t, u^-) & \text{for } \sigma \rightarrow 0^- \end{cases} \quad (3.5.2)$$

where the scalar input is defined as,

$$u = \begin{cases} u^+ & \text{for } \sigma > 0 \\ u^- & \text{for } \sigma < 0 \end{cases} \quad (3.5.3)$$

The system is said to be in sliding mode when a representative point of the system moves along the sliding surface $\sigma(\mathbf{x}, t) = 0$, as shown in Fig. 3.36. Consequently, the control design consists in developing a sliding surface and continuous functions u^+ and u^- , so that the closed loop system is maintained on sliding mode [82]. In this work, $u^+ = 1$ and $u^- = 0$ are the outputs of the hysteresis comparator.

For the implementation of the sliding mode control for DBI shown in Fig. 3.2, the diagonal power devices of the inverter (S_1 and S_4) are controlled with the same gating signals $u(t)$, while the other diagonal power devices (S_2 and S_3) are controlled with the complementary gating signals $1 - u(t)$. These two complementary control signals define the global operation of the system. This approach shows the difference regarding other control strategies, where the model of the inverter is obtained for each boost converter.

In this case, the output current is established as shown in Fig. 3.37 because the output voltage (v_o) of the DBI is defined as,

$$v_o(t) = v_{c2}(t) - v_{c1}(t) \quad (3.5.4)$$

Considering this definition and the signals $u(t) = S_1$ and $1 - u(t) = S_3$, the averaged

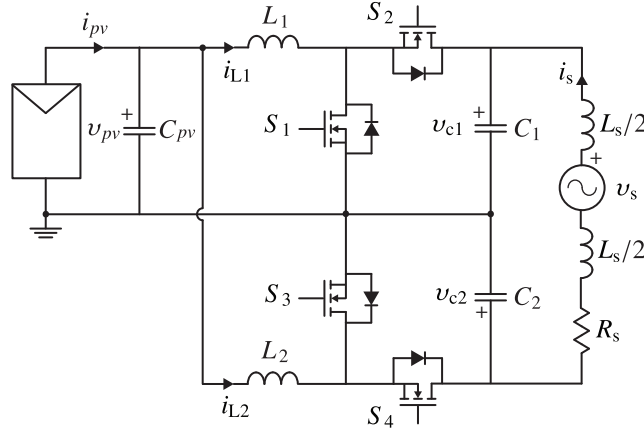


Figure 3.37. Dual boost inverter topology with other considerations.

switched model of the DBI is described by

$$L_1 \frac{di_{L1}(t)}{dt} = v_{pv} - v_{c1}(t) \cdot (1 - u(t)) \quad (3.5.5)$$

$$L_2 \frac{di_{L2}(t)}{dt} = v_{pv} - v_{c2}(t) \cdot u(t) \quad (3.5.6)$$

$$C_1 \frac{dv_{c1}(t)}{dt} = (1 - u(t)) \cdot i_{L1}(t) + i_s(t) \quad (3.5.7)$$

$$C_2 \frac{dv_{c2}(t)}{dt} = u(t) \cdot i_{L2}(t) - i_s(t) \quad (3.5.8)$$

where i_{L1} and i_{L2} are the currents through the inductors L_1 and L_2 , i_s is the grid current, v_{c1} and v_{c2} are the voltage of the capacitors, v_{pv} is the input voltage, $u(t)$ and $1 - u(t)$ are the duty cycles, and S_1 and S_3 are the switching signals.

The product between the state variables and control input (bilinear term) in equations (3.5.5)–(3.5.8) shows that the non-linearity of the inverter model is preserved.

On the other hand, the DBI is integrated to the grid through an inductive filter L_s (R_s represents the resistance of the inductive filter and grid), as illustrated in Fig. 3.38. In base on this equivalent circuit, the voltage equation can be determined by

$$L_s \frac{di_s(t)}{dt} = \underbrace{v_{c2}(t) - v_{c1}(t)}_{v_o(t)} - i_s(t)R_s - v_s(t) \quad (3.5.9)$$

The proposed control of the DBI is shown in Fig. 3.39, which consists of cascaded control loops. The fast non-linear inner control loop, based on sliding mode control, regulates the difference of the current in the inductors of boost converters, while the linear and slower control loop, manages through a PR the current injected to the grid. The last external control loop is designed to regulate the PV voltage indirectly through the control of the input capacitor voltage. Finally, in order to obtain the maximum power from the PV panel, the

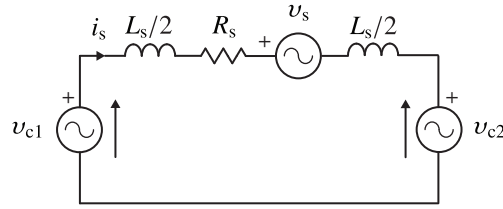


Figure 3.38. Equivalent model of the DBI with grid connection (global control).

perturb and observed P&O algorithm is implemented to generate the voltage reference v_{pv}^* , as mentioned in previous sections.

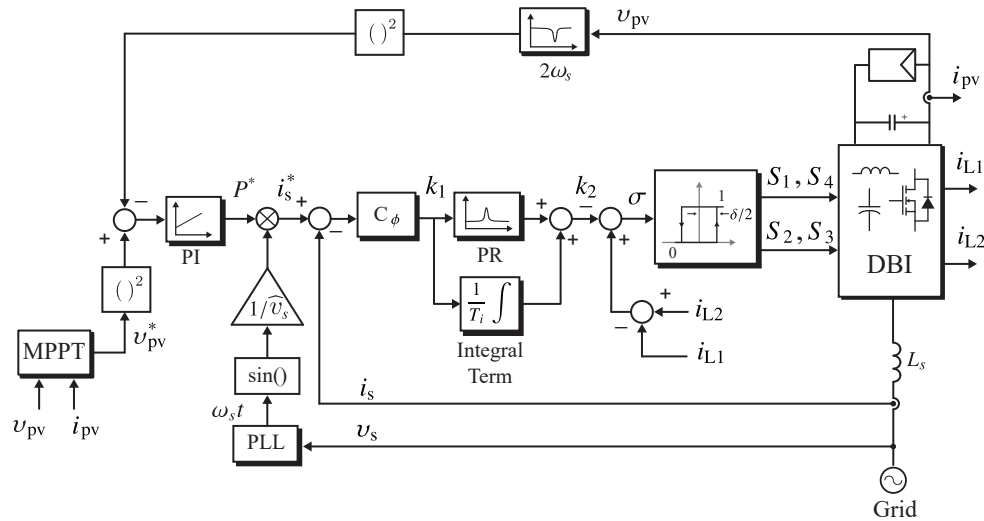


Figure 3.39. The cascaded control scheme of the grid-connected DBI, with external PR controller and internal sliding mode controller.

3.5.1 Control of the boost current

To control the output current of the DBI, the sliding mode approach is proposed for the non-linear inner control loop. The analysis here developed has its foundation in the behavior of the variables of the dual boost inverter under the presence of a sinusoidal reference introduced in [66]. However, this was solved in [66] to obtain a voltage control loop with a linear load, which cannot be directly extended for a current control in the grid-connected applications. This adds a new state variable to the system defined in (3.1.5). Thus, it is necessary to adapt the SMC law to fulfill this new control objective. To accomplish this, the analysis is based on the equivalent control approach.

3.5.1.1 Sliding surface selection

Considering that the output voltage of the inverter is obtained from subtracting the voltage of the capacitors (v_{c1} and v_{c2}), and that the capacitor voltage control is related to the inductor current, it is possible to establish that the difference between the current of the inductors indirectly controls the output voltage of the dual boost inverter [18]. Therefore, the sliding surface ($\sigma(t)$) can be defined by

$$\sigma(t) = -k_2(t) + i_{L2}(t) - i_{L1}(t) \quad (3.5.10)$$

where k_2 is the output of external control loop.

Please note that by considering the current derivatives of (3.5.5) and (3.5.6), the sliding surface can be rewritten as

$$\sigma(t) = -k_2(t) + \int_{t_0}^t \left[\frac{v_{pv}}{L_2} - \frac{v_{c2}(t)}{L_2} \cdot u(t) \right] dt - \int_{t_0}^t \left[\frac{v_{pv}}{L_1} - \frac{v_{c1}(t)}{L_1} \cdot (1 - u(t)) \right] dt \quad (3.5.11)$$

3.5.1.2 Equivalent control

In order to guarantee that the sliding mode is maintained on the selected surface, it is necessary to find the equivalent control (u_{eq}) through the invariance condition given by

$$\left. \frac{d\sigma}{dt} \right|_{\substack{\sigma=0 \\ u=u_{eq}}} = 0 \quad (3.5.12)$$

Hence, the derivative of the sliding surface evaluated in $\sigma = 0$ and $u = u_{eq}$ is

$$\frac{d\sigma}{dt} = -\frac{dk_2(t)}{dt} + \frac{v_{pv}}{L_2} - \frac{v_{c2}(t)}{L_2} \cdot u_{eq}(t) - \frac{v_{pv}}{L_1} + \frac{v_{c1}(t)}{L_1} \cdot (1 - u_{eq}(t)) = 0 \quad (3.5.13)$$

From (3.5.13) and due to the symmetry of the inverter ($L = L_1 = L_2$), the equivalent control is defined as

$$u_{eq}(t) = \left(-\frac{dk_2(t)}{dt} + \frac{v_{c1}(t)}{L} \right) \frac{L}{v_{c1}(t) + v_{c2}(t)} \quad (3.5.14)$$

3.5.1.3 Existence condition

With the expression of equivalent control in (3.5.14), the next step is to prove the existence condition, which can be determined by

$$\sigma(\mathbf{x}, t) \cdot \frac{d\sigma(\mathbf{x}, t)}{dt} < 0 \quad (3.5.15)$$

Thus, the derivative of the surface is replaced in (3.5.15), expressing the existence condition as

$$\sigma \left[-\frac{dk_2(t)}{dt} + \frac{v_{pv}}{L} - \frac{v_{c2}(t)}{L} \cdot u(t) - \frac{v_{pv}}{L} + \frac{v_{c1}(t)}{L} \cdot (1 - u(t)) \right] < 0 \quad (3.5.16)$$

To establish a relationship between $u(t)$ and $u_{\text{eq}}(t)$, the expression $-u_{\text{eq}}(t) + u_{\text{eq}}(t) = 0$ is added in (3.5.16), resulting in

$$\sigma \left[-\frac{dk_2(t)}{dt} + \frac{v_{\text{pv}}}{L} - \frac{v_{\text{c2}}(t)}{L} \cdot \left(\underbrace{u(t) - u_{\text{eq}}(t) + u_{\text{eq}}(t)}_{=0} \right) - \frac{v_{\text{pv}}}{L} + \frac{v_{\text{c1}}(t)}{L} \cdot \left(1 - \left(\underbrace{u(t) - u_{\text{eq}}(t) + u_{\text{eq}}(t)}_{=0} \right) \right) \right] < 0 \quad (3.5.17)$$

It is possible to reduce (3.5.17) by considering (3.5.13), which leads to

$$\sigma \left[\frac{v_{\text{c1}}(t) + v_{\text{c2}}(t)}{L} \cdot (-u(t) + u_{\text{eq}}(t)) \right] < 0 \quad (3.5.18)$$

Finally, evaluating (3.5.18), and considering that $v_{\text{c1}} > 0$, $v_{\text{c2}} > 0$ and $L > 0$, it can be determined that if the switching surface is positive, the term $(-u(t) + u_{\text{eq}}(t))$ should be negative to accomplish the existence condition, which implies $u = u^+ = 1$. Otherwise, if the switching surface is negative, the term $(-u(t) + u_{\text{eq}}(t))$ should be positive and the action control takes the minimum value ($u = u^- = 0$), which can be expressed as

$$\begin{cases} \sigma > 0 \text{ and } u > u_{\text{eq}} & \longrightarrow u = u^+ = 1 \\ \sigma < 0 \text{ and } u < u_{\text{eq}} & \longrightarrow u = u^- = 0 \end{cases} \quad (3.5.19)$$

The control action defined by (3.5.19) leads to the state trajectory to slide on the switching surface and eventually reach the intersection of the switching surface and the equilibrium point converging in a finite time, as demonstrated in [66].

3.5.2 Control of the grid current

The main goal of this loop is to regulate the grid current of the DBI. The angle of i_s^* is obtained from a PLL, which is used to reconstruct a sinusoidal waveform enabling synchronization with the grid [3,83]. The amplitude for the current reference is provided by the PI controller, which regulates the energy through C_{pv} . Since the current reference is sinusoidal, a proportional resonant controller is used, which is tuned to the grid frequency ω_s .

3.5.2.1 Linearization

To design the controller of the outer loop, it is necessary to find the transfer function between the grid current i_s and the output of the external control loop k_2 . The equivalent control approach (Equation (3.5.14)) is used to introduce the variable k_2 in the averaged switched model of the inverter. Therefore, the equivalent control of $u_{\text{eq}}(t)$ and its complement ($1 - u_{\text{eq}}(t)$) are redefined as

$$u_{\text{eq}}(t) = \frac{v_{\text{c1}}(t)}{v_{\text{c1}}(t) + v_{\text{c2}}(t)} - \frac{L}{v_{\text{c1}}(t) + v_{\text{c2}}(t)} \cdot \frac{dk_2(t)}{dt} \quad (3.5.20)$$

$$1 - u_{\text{eq}}(t) = \frac{v_{\text{c2}}(t)}{v_{\text{c1}}(t) + v_{\text{c2}}(t)} + \frac{L}{v_{\text{c1}}(t) + v_{\text{c2}}(t)} \cdot \frac{dk_2(t)}{dt} \quad (3.5.21)$$

The control signals $u(t)$ and $1 - u(t)$ are substituted by the equivalent control $u_{\text{eq}}(t)$ and $1 - u_{\text{eq}}(t)$ in equations (3.5.5)–(3.5.8), where it is possible to identify that the derivative of

current through L_1 presents the same behavior of the derivative of i_{L2} . For this reason, i_{L1} was omitted and the state variables of the non-linear model are defined by

$$\begin{aligned}\dot{\mathbf{x}}(t) &= \mathbf{f}[\mathbf{x}(t)] + \mathbf{B}\mathbf{u}(t) \\ \mathbf{y}(t) &= \mathbf{C}\mathbf{x}(t)\end{aligned}\tag{3.5.22}$$

where

$$\begin{aligned}\mathbf{f}(\mathbf{x}) &= \begin{bmatrix} f_1 \\ f_2 \\ f_3 \\ f_4 \end{bmatrix} = \begin{bmatrix} \dot{x}_1 \\ \dot{x}_2 \\ \dot{x}_3 \\ \dot{x}_4 \end{bmatrix} = \begin{bmatrix} \frac{di_{L2}(t)}{dt} \\ \frac{dv_{c1}(t)}{dt} \\ \frac{dv_{c2}(t)}{dt} \\ \frac{di_s(t)}{dt} \end{bmatrix} \\ \mathbf{y} &= \begin{bmatrix} i_s \end{bmatrix} = \begin{bmatrix} x_4 \end{bmatrix} \\ \mathbf{u} &= \begin{bmatrix} k_2 \end{bmatrix}\end{aligned}\tag{3.5.23}$$

Taking into account that $\sigma(t) = 0$, the current through inductor L_1 can be obtained as,

$$i_{L1}(t) = i_{L2}(t) - k_2(t)\tag{3.5.24}$$

Considering (3.5.24), $v_o = v_{c2} - v_{c1}$, and that the value of the capacitors are the same $C_1 = C_2 = C$, the linear model of the system can be expressed as

$$\Delta\dot{\mathbf{x}} = \begin{bmatrix} \Delta\dot{x}_1 \\ \Delta\dot{x}_2 \\ \Delta\dot{x}_3 \\ \Delta\dot{x}_4 \end{bmatrix} = \underbrace{\begin{bmatrix} 0 & -\frac{1}{4L} & -\frac{1}{4L} & 0 \\ \frac{1}{2C} & 0 & 0 & \frac{1}{C} \\ \frac{1}{2C} & 0 & 0 & -\frac{1}{C} \\ 0 & -\frac{1}{L_s} & \frac{1}{L_s} & \frac{R_s}{L_s} \end{bmatrix}}_{\mathbf{A}} \cdot \begin{bmatrix} \Delta x_1 \\ \Delta x_2 \\ \Delta x_3 \\ \Delta x_4 \end{bmatrix} + \underbrace{\begin{bmatrix} 0 \\ -\frac{1}{2C} \\ 0 \\ 0 \end{bmatrix}}_{\mathbf{B}} \cdot \Delta u + \underbrace{\begin{bmatrix} \frac{1}{L} \\ 0 \\ 0 \\ 0 \end{bmatrix}}_{\mathbf{E}} \cdot \Delta p\tag{3.5.25}$$

$$\Delta\mathbf{y} = \underbrace{\begin{bmatrix} 0 & 0 & 0 & 1 \end{bmatrix}}_{\mathbf{C}} \cdot \begin{bmatrix} \Delta x_1 \\ \Delta x_2 \\ \Delta x_3 \\ \Delta x_4 \end{bmatrix}\tag{3.5.26}$$

Please note that the same equilibrium point shown in [66] was used in this analysis, which is defined as $[x_{10}, x_{20}, x_{30}, x_{40}, k_{20}] = [0, 2 \cdot v_{pv}, 2 \cdot v_{pv}, 0, 0]$.

Considering the equations in Laplace domain, the transfer function can be defined as

$$G(s) = \frac{\Delta y(s)}{\Delta u(s)} = \mathbf{C} \cdot (s\mathbf{I} - \mathbf{A})^{-1} \cdot \mathbf{B}\tag{3.5.27}$$

Replacing the matrices and performing some algebraic operations, the relation between the grid current i_s and k_2 can be derived as

$$G(s) = \frac{\Delta y(s)}{\Delta u(s)} = \frac{i_s(s)}{k_2(s)} = \frac{1}{2CL_s} \cdot \frac{1}{s^2 + \frac{R_s}{L_s}s + \frac{2}{CL_s}} \quad (3.5.28)$$

Please note that the transfer function is of second order and depends only on the capacitor value, the grid filter, and the grid resistance.

3.5.2.2 Outer control design

The plant $G(s)$ is critically stable because it presents a complex conjugate pole pair in the left half-plane close to the imaginary axis. To better illustrate this issue, the frequency response of the plant is shown in Fig. 3.40, where a significant resonant peak located at 1 kHz can be appreciated. To compensate this peak, to assure a zero steady-state error at 60 Hz (grid frequency) and to regulate the grid current of the inverter, a PR controller is used. The transfer function of the PR controller in the Laplace domain is given by

$$C_{PR}(s) = k_p + \frac{2k_i\omega_c s}{s^2 + 2\omega_c s + \omega_o^2} \quad (3.5.29)$$

where k_p is the proportional gain, k_i is the resonant gain, ω_c is the cut-off frequency, and ω_o is the fundamental frequency.

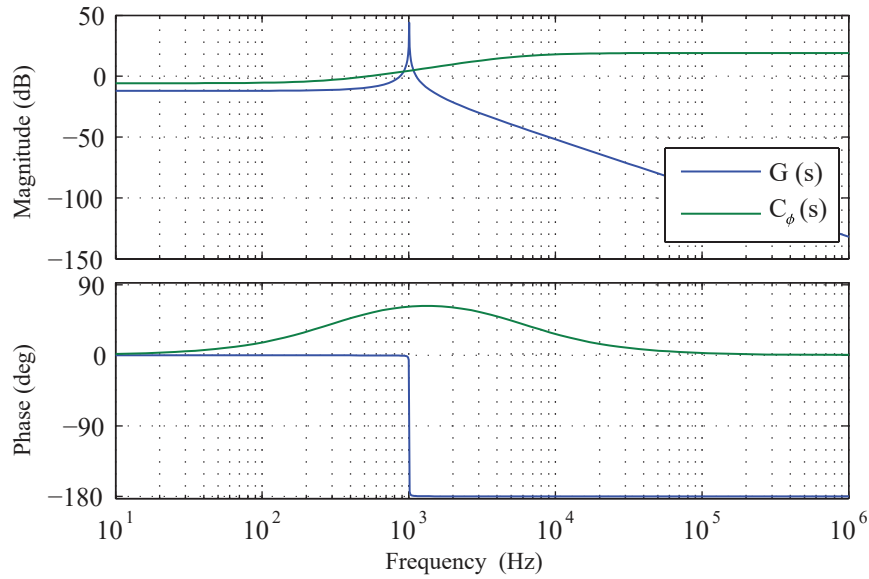


Figure 3.40. Bode diagrams of the plant and phase compensator.

Please note that to deal with the sensitivity issue of the ideal PR controller, a bandwidth around the resonant frequency of the controller is added through the cut-off frequency, obtaining a non-ideal PR controller with finite gain [84]. The parameters applied to calculate the PR controller are shown in Table 3.7.

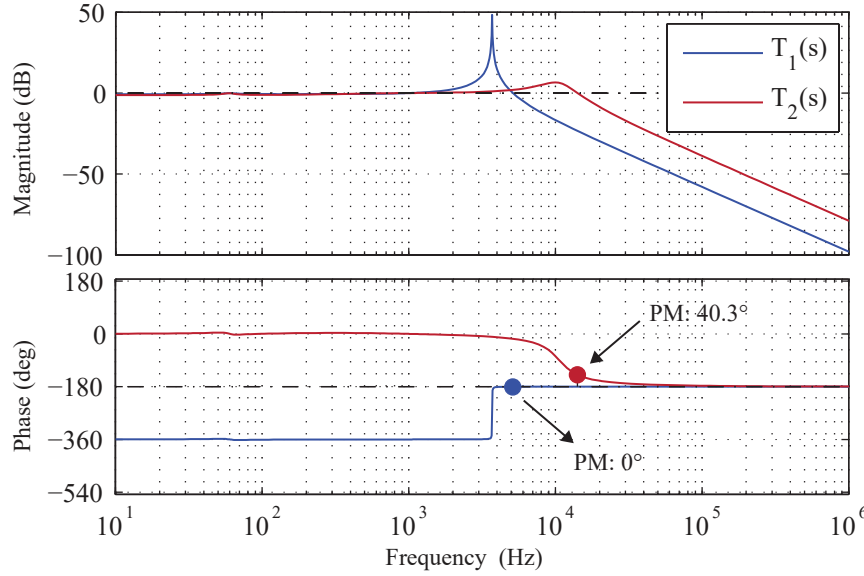


Figure 3.41. Bode diagrams of closed-loop without and with the phase compensator.

The closed-loop Bode diagram of the system (T_1) is shown in Fig. 3.41. Although a finite gain at grid frequency is introduced to obtain a zero-state error in the tracking of the grid current reference, a sufficient degree of the relative stability is not achieved, since the phase margin is equal to zero [85]. Therefore, a phase compensator C_ϕ is included to increase the phase margin. The transfer function of this compensator is given by

$$C_\phi(s) = k \cdot \frac{s + a}{s + b} \quad (3.5.30)$$

This compensator is composed of a pole and a zero to incorporate phase in the system [86]. As a result, the effect of the cascaded phase compensator is shown in the bode diagram of closed-loop $T_2(s)$ of Fig. 3.41, where a phase margin of 40.3° is achieved. The parameters of the phase compensator are shown in Table 3.7.

In addition, to avoid an offset in the grid current of the inverter, due to the fact that in a practical implementation both DC–DC converters will not be exactly the same, an integration term is incorporated in the control scheme, as shown in Fig. 3.39, to force the steady-state error to zero at $\omega = 0$.

3.5.3 Simulation results with sliding mode control for DBI

In order to analyze the behavior of the sliding mode strategy, the DBI with the PV panel as input source is implemented in the PLECs software. The main parameters of the PV panel together with the grid, inverter and control parameters are listed in Table 3.7.

The simulation results of the DBI under steady-state operation are presented in the first part of this section. Two operation points are chosen, which are the same used in the previous cases (linear control, FCS-MPC and flatness-based control), i.e two different level of the PV

Table 3.7. Simulation parameters of the sliding mode control for DBI.

Symbol	Parameter	Value
PV Parameters		
V_{mpp}	PV voltage at MPP	29 V
P_{pv}	PV power	216 W
V_{oc}	Open circuit voltage	36.1 V
I_{sc}	Short circuit current	8.13 A
Grid Parameters		
v_s	Grid voltage	110 V_{rms}
f_s	Grid frequency	60 Hz
L_s	Grid filter inductance	10 mH
Converter Parameters		
C_{pv}	Input capacitor	25 mF
L_1, L_2	Inverter inductors	55 μ H
C_1, C_2	Inverter capacitors	5 μ F
Control Parameters		
k_p^{PI}	Proportional gain of PI (PV voltage control)	4
k_i^{PI}	Integral gain of PI (PV voltage control)	50
k	Gain of C_ϕ	9
k_p	Proportional gain of PR	50
k_i	Resonant gain of PR	500
ω_c	Cut-off frequency of PR	5 rad/s
a	Zero of phase compensator	2000
b	Pole of phase compensator	35.000

power. The first input power is 216 W, which corresponds to the nominal condition, and the other input power is around 150 W. On the other hand, the second test is presented to evaluate the dynamic performance. This test consists of a step-down in the input power at time 2.0 s.

The first case of analysis of the steady-state operation is with 1000 W/m² of the solar irradiance, which corresponds to an input power of 216 W generated by the PV panel. The main results are shown in Fig. 3.42. The voltage of the capacitors (v_{C1} , v_{C2}) are shown in Fig. 3.42(a), where each voltage is composed by DC and AC components. In this case, the DC component is the same in each converter. It is 58 V, which is the double of the input voltage, as expected through the previous analysis, and the amplitude of AC component is half of the output voltage on the inverter, i.e 77.78 V $((110 \cdot \sqrt{2})/2)$. Please note that, the voltage of the capacitors is not sinusoidal. However, the difference of the voltages between these waveforms (output voltage) is sinusoidal.

In the Fig. 3.42(b), the currents in the inductors are illustrated. The peak amplitudes of the currents are the same in both inductors, as expected. Then, the phases between these waveform are shifted 180°, similar to the voltage of the capacitors.

For the second case of the steady-state operation, the input power chosen is 150 W, which is achieved when the solar irradiance in the PV panel is 700 W/m². In this case, the waveforms of the voltage capacitors are the same with regard to the previous case, as it can be seen in

Fig. 3.42(a). For the inductor currents, the peak amplitudes are different because the input power changes (see Fig. 3.44(b)).

For both cases, the grid current is a sinusoidal and always in phase with the grid voltage, as illustrated in Fig. 3.42(c) and 3.44(c). Then, the frequency spectrum of the output current is shown in Fig. 3.43 and 3.45. Also, the THD for each case is added in these figures. As it can be observed, the harmonics and THD for both power levels are within the standard limits.

The simulation results of the second test are illustrated in Fig. 3.46 and 3.47. A step-down in the solar irradiance from 1000 W/m^2 to 700 W/m^2 at time $t = 2.0 \text{ s}$ is used in the second test to evaluate the dynamic performance of the proposed control. Please notice that the solar irradiance values are equal to the steady-state tests.

The reference v_{pv}^* and measurement v_{pv} of the panel voltage are shown in Fig. 3.46(a). Note that, the three voltage levels due to the MPPT algorithm can be identified. When the solar irradiation is reduced, the PV current also decreases as shown in Fig. 3.46(b). As a result of this change, the PV power is reduced as it can be seen in Fig. 3.46(c). Therefore, the PV voltage changes the value to achieve the new power point.

The main waveforms of the DBI and its control for the second dynamic test are exposed in Fig. 3.47. When the PV power decreases at two seconds, the reference of the grid current is also reduced (see Fig. 3.47(d)), which is reflected in the reduction of the amplitude of the inductor currents, as expected. Please note that during this test, the capacitor voltages are kept constant.

The reduction effect is also seen in the control signal. For example, the reference (k_2) of the inner control loop and the difference between the inductor currents are decreased at 2.0 s, as observed in Fig. 3.47(c). Then, the tracking of the grid current reference is achieved in all the tests, as it can be seen in the Fig. 3.47(d).

On the other hand, the grid current is very close to a sinusoidal and always in phase with the grid voltage, as shown in Fig. 3.47(e).

3.5.4 Discussion

A global sliding mode current control scheme for a grid-connected DBI is presented in this section. Three control loops compose the proposed method: a PI control loop regulates the energy of the input capacitor, a linear PR control loop is designed to regulate the output current of the inverter (grid current), while the non-linear sliding mode inner control loop regulates the difference between the current of the inductors of the DBI, which allows control of the output voltages of the capacitors indirectly.

However, the experimental implementation of this strategy could become a disadvantage since an analogue circuit is used to implement the hysteresis stage in order to generate the switching signals at finite frequency (variable switching frequency). On the other hand, a digital implementation of the hysteresis requires a high computational demand.

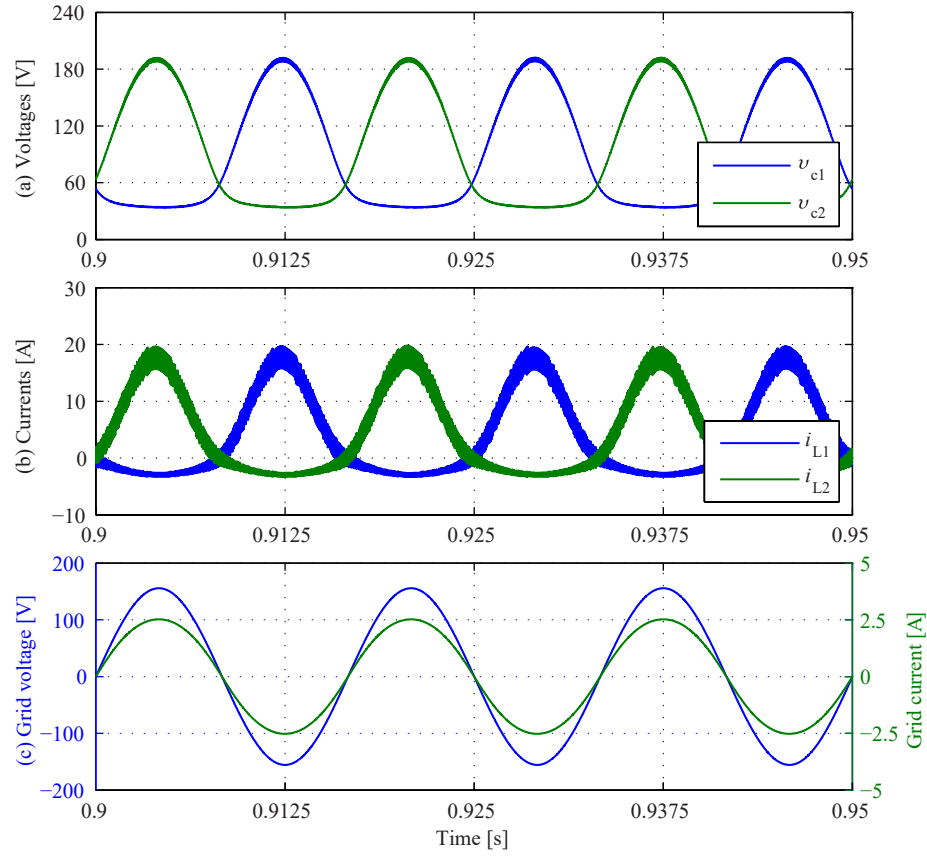


Figure 3.42. Steady-state results of sliding mode control for DBI at 216 W of PV power: (a) Capacitor voltage of each boost converter, (b) inductor current of each boost converter, and (c) grid voltage and current.

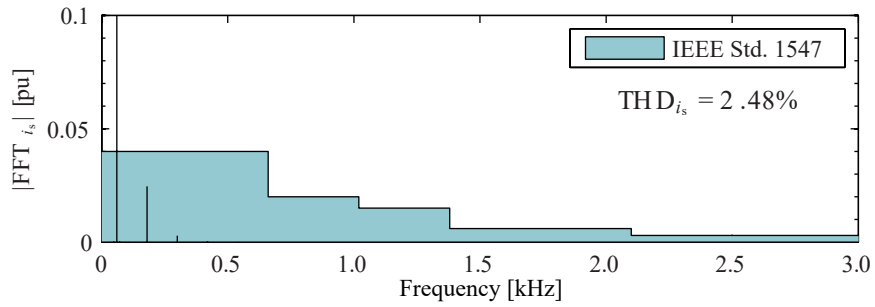


Figure 3.43. Grid current spectrum of DBI with sliding mode control at 216 W of PV power.

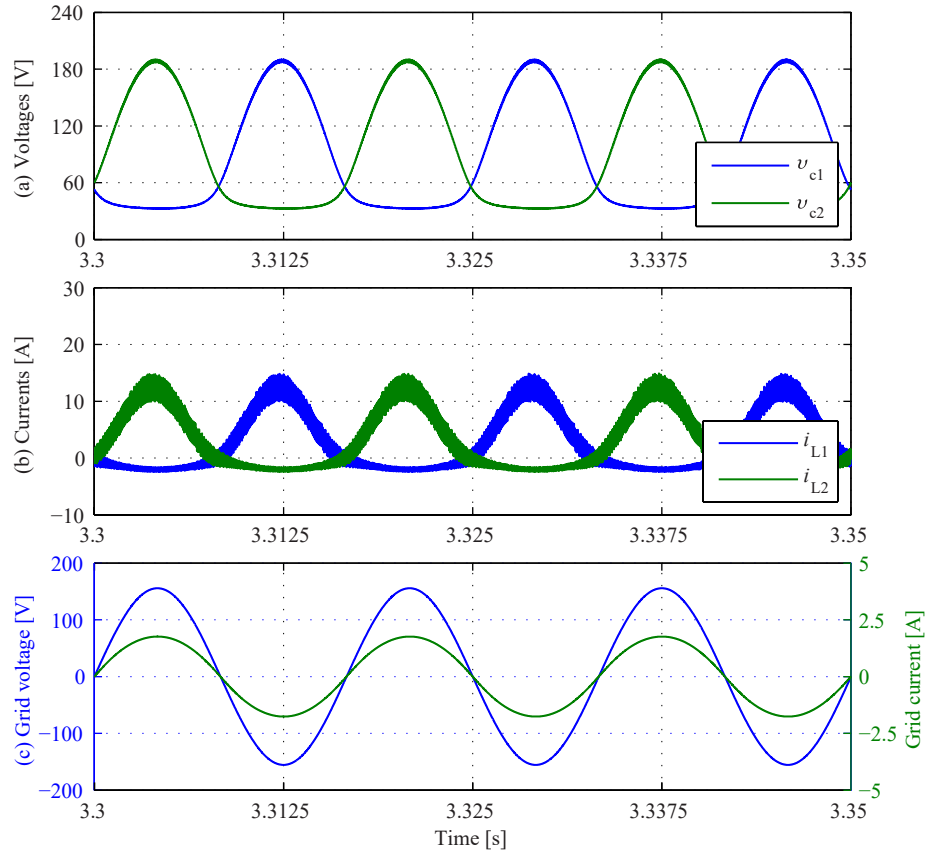


Figure 3.44. Steady-state results of sliding mode control for DBI at 150 W of PV power: (a) Capacitor voltage of each boost converter, (b) inductor current of each boost converter, and (c) grid voltage and current.

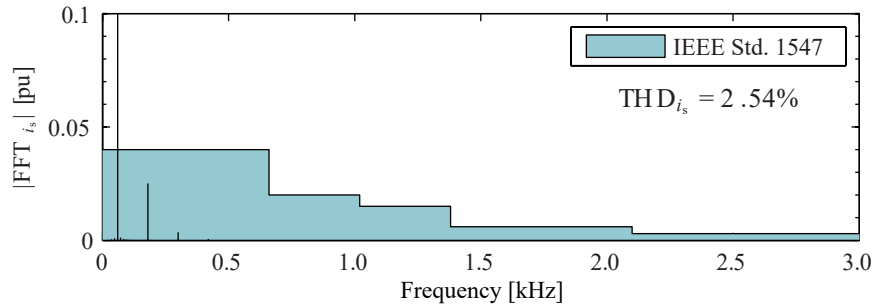


Figure 3.45. Grid current spectrum of DBI with sliding mode control at 150 W of PV power.

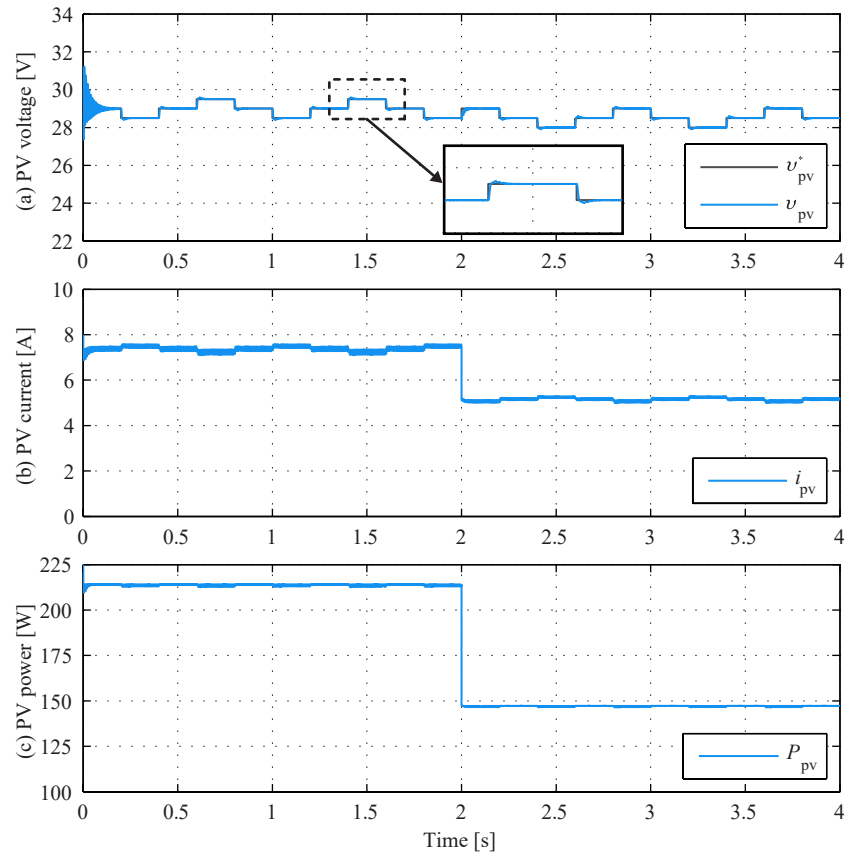


Figure 3.46. Dynamic results of sliding mode control for DBI: (a) PV voltage, (b) PV current, and (c) PV power.

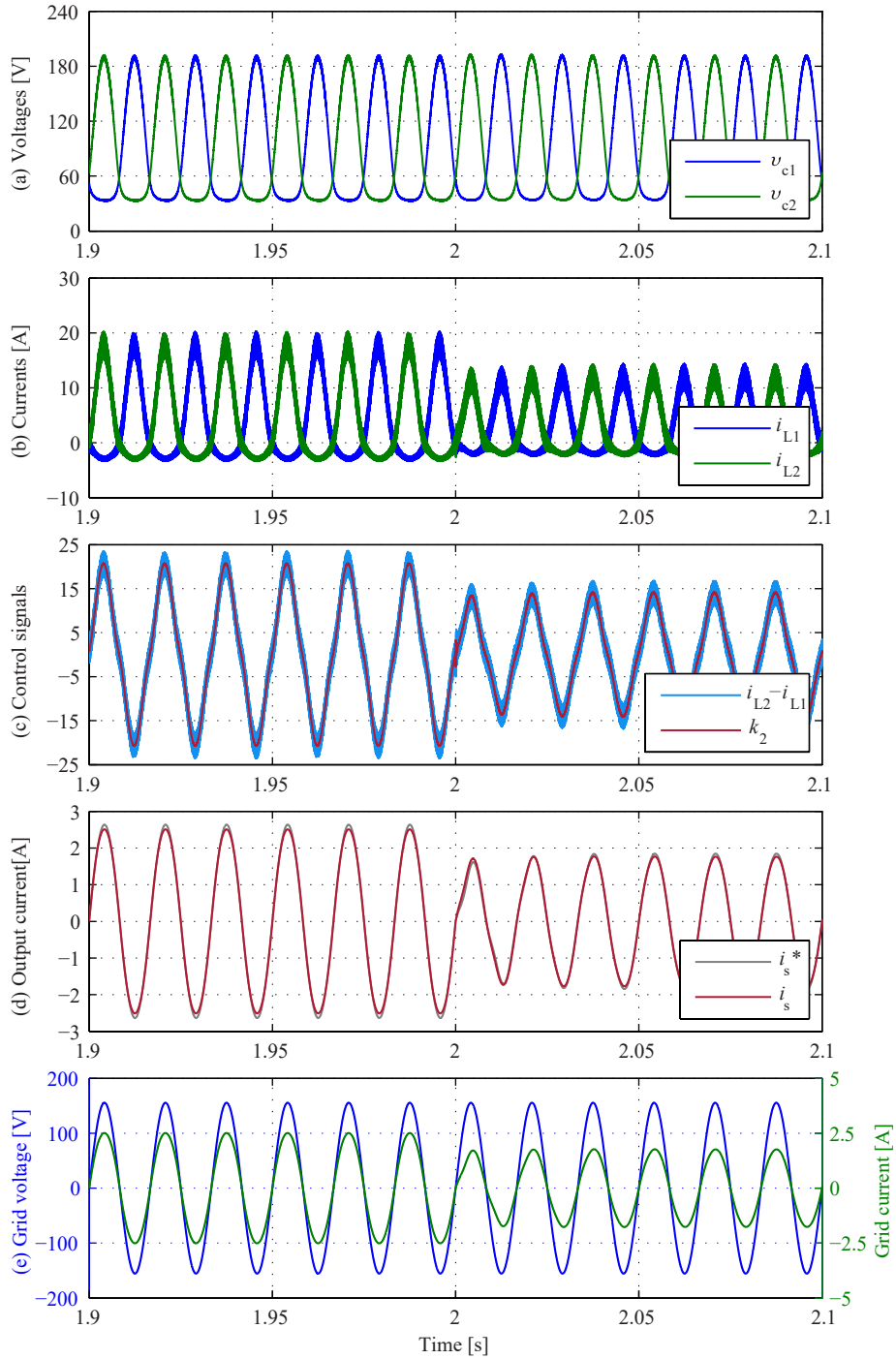


Figure 3.47. Dynamic results of sliding mode control for DBI: (a) Capacitor voltages, (b) inductor currents, (c) control signals, (d) measurement and reference of grid current, and (e) grid current and voltage.

3.6 Comparison

In this section, a comparison between the linear control and the three proposed non-linear control strategies is presented. In order to achieve a fair comparison, parameters of the simulated systems are uniformed. Dynamic behavior of each control techniques is performed under the same scenario considering a variation in the irradiation received by the PV source

The main parameters considered in the comparison are control targets, number of the cascaded control loops, and two performance metrics [87]: the total harmonic distortion (THD) and average switching frequency.

As previously mentioned in section 3.1, the control strategies for DBI can be classified in independent and global methods. In this work, linear control, FCS-Model Predictive Control and flatness-based control strategies are based on the independent control strategy, where each boost converter is regulated to obtain a sinusoidal output voltage. On the other hand, the sliding control strategy relies on a global control strategy.

Since the input source is a PV panel, the first control loop of the four control strategies presented in this work consists of a MPPT algorithm and an input capacitor energy control loop to regulate indirectly the PV voltage. For the linear control, the control targets are the input capacitor energy, the output capacitor voltage and the inductor current of each boost converter. The output of the first control loop is the power reference from which the output voltage references of the boost converters are calculated. Considering that the boost converters are identical, only the control scheme for one boost converter will be described. The control strategy for the second converter is similar. The output voltage of the capacitor is regulated through a PR controller, whose output is the current capacitor reference i_{c1}^* . This signal is used to calculate the reference of the inductor current i_{L1}^* . A second PR controller is employed to regulate the current through the inductor. The output of this controller is the inductor voltage v_{L1} , which is compensated in order to find the duty-cycle. The linear control scheme for the grid-connection of the DBI with PV panel is shown in Fig. 3.48(a).

In the case of FCS-MPC, the main goals of control are the energy of the input capacitor, the current through the inductor, and voltage in the capacitor for each boost converter. Therefore, a cascaded control loops scheme is used, where the first control loop regulates the energy of the input capacitor C_{pv} , followed by the FCS-Model Predictive Control stage, which regulates the output capacitor voltage, and inductor current in each boost converter, as shown in Fig. 3.48(b).

The flatness-based control scheme consists of two cascaded loops, as shown in Fig. 3.48(c). The targets of its first control loop are similar to the control scheme of the linear control, i.e. input capacitor energy regulation and indirect active power control. The second loop control regulates the energy stored in the output capacitors C_1 , C_2 , and inductors L_1 , L_2 of the DBI.

Considering the description of the control schemes mentioned before, five control loops in total are required to regulate the DBI with linear control. For FCS-Model Predictive Control and flatness based control, it is necessary two and three control loops in total, respectively. The summary of the total number of the control loops for each control strategy is shown in Table 3.8.

In a different way, the proposed control based on the sliding mode approach considers the global strategy, where the main control purpose is the output current of the DBI. To achieve this objective, the cascaded control scheme shown in Fig. 3.48(d) was employed. The target of the first loop, like the previous schemes, is the energy of the input capacitor. The output current of the DBI is the control objective of the second control loop. To continue, the inner

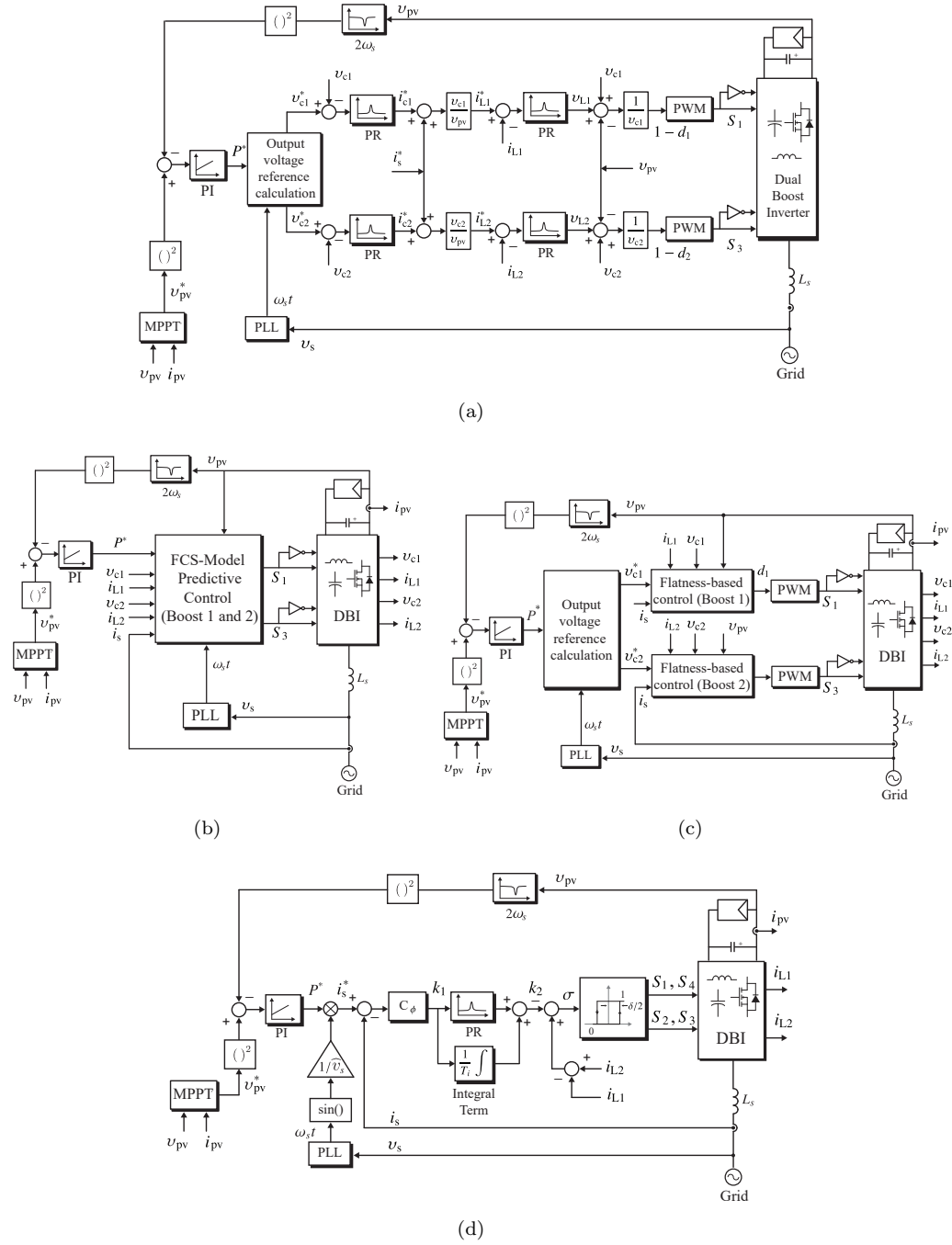


Figure 3.48. The four diagram control of the DBI: (a) Linear control, (b) FCS-MPC, (c) flatness-based control, and (d) sliding mode control.

control loop determines the switching surface based on the difference of the current in the inductors regulation. Since, the sliding mode control is based on a current regulation, fewer sensors are required since the output voltage is not directly controlled and does not need to be measured.

Another important point to consider is the behavior of the inverter operating in the nominal power at 216 W. In the four control schemes, the voltage of the capacitors (C_1 and C_2) is composed by DC and AC components, as shown in Fig. 3.49. The AC component of the capacitor voltages with the linear control, FCS-MPC and flatness-based strategies is a pure sinusoidal, in which the maximum amplitude is around 77 V. While, the DC voltage component is 112.7 V. On the other hand, the DC component is 58 V with the sliding mode control, which is the double of the input voltage, which is an effect of the sliding mode strategy.

The tracking of the output capacitor voltage references v_{c1}^* , v_{c2}^* is achieved by the linear control, the FCS-Model Predictive Control and the flatness-based control. However, high frequency oscillations are presented in the linear control case, which are reflected in the current waveforms. On the other hand, the output voltage capacitors obtained with FCS-MPC also have some oscillations influencing the performance on the output current.

The current through the inductors (i_{L1} and i_{L2}) with the four control proposed present a negative component due to the circulating power. The current ripple chosen in the design was 5 A, which is achieved with the linear control, flatness-based control and sliding mode control, as shown in Fig. 3.50(a), Fig. 3.50(c) and Fig. 3.50(d).

Also, the average switching frequency (\bar{f}_{sw}) is another point to analyze, because this parameter is directly influenced by the inductor current ripple. In the linear control, flatness-based and sliding mode controls, the average switching frequency obtained was around 80 kHz. On the other hand, the current ripple in the positive peak with FCS-MPC is 14.98 A, while the average switching frequency is 50 kHz. It is important to indicate that the switching frequency does not correspond to the current ripple value, since the switching frequency in FCS-MPC is variable, which is the main disadvantage of this control, as indicated in the previous section.

On the other hand, to achieve an average switching frequency of 80 kHz with FCS-MPC, it is necessary a very small sampling time. For example, the sampling time used in the simulation was 5×10^{-5} s, where the average switching frequency is 50 kHz. Therefore, the sampling time should be reduced at 3.3×10^{-6} s to obtain the 80 kHz as average switching frequency. The inductor currents with this sampling time are shown in the Fig. 3.51, which presents a zoom in the positive and negative peaks, where it is possible to identify that the switching frequency in the positive peak is 45 kHz ($1/\Delta_{t1}$), and the current ripple is 9.94 A. For this reason, the sampling time is selected to obtain a good trade-off between the average switching frequency and the ripple of the inductor. The design value of the inductor ripple can be achieved but the sampling time should be very small, and the platform to implement this control should be more advanced. Therefore, the sampling time used in the simulations is 5×10^{-5} s.

Moreover, it is important to evaluate the power quality obtained with each control proposed. For this, the total harmonic distortion and spectrum of the grid current are considered. The grid currents obtained with the four control methods comply with the IEEE standard 1547, as it can be observed in Fig. 3.52. However, the highest THD among the four controls was with the linear control strategy, because the output current of the DBI with the linear control contains more oscillations than with other controllers, as shown in Fig. 3.10(c)

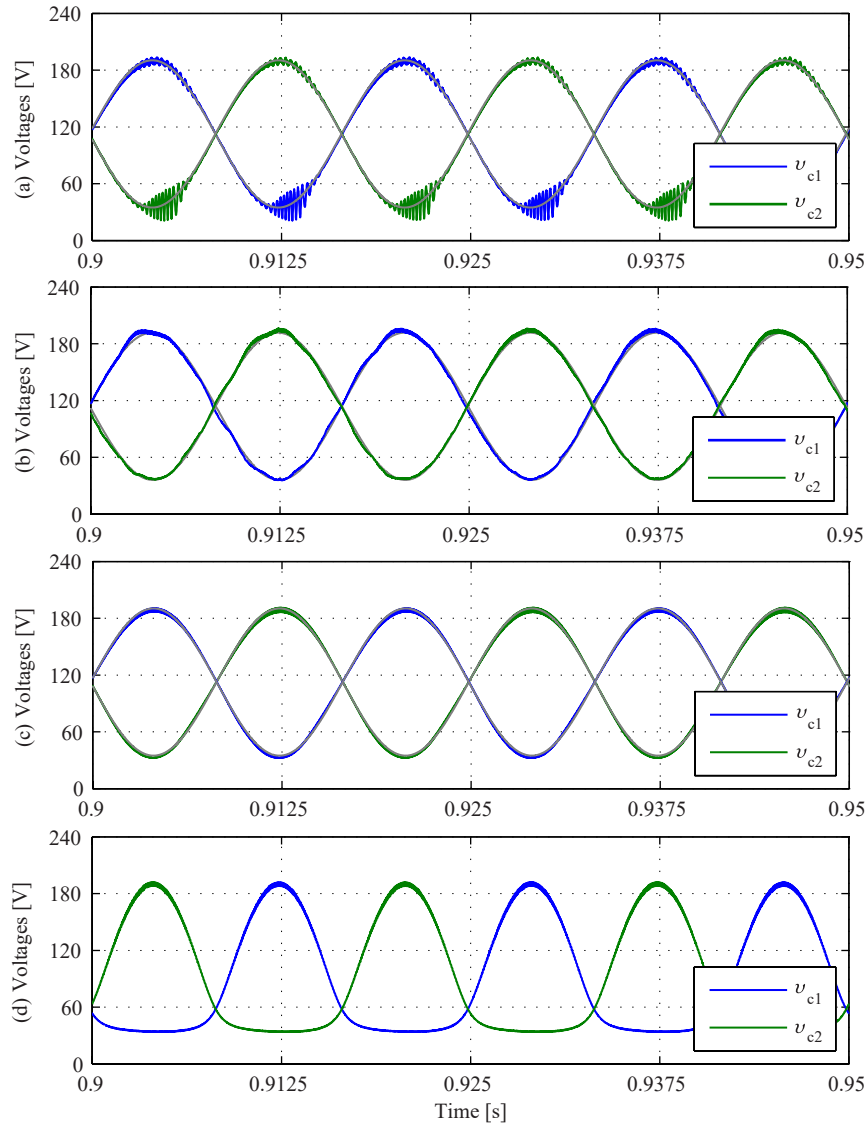


Figure 3.49. Capacitor voltages with: (a) Linear control, (b) FCS-Model Predictive Control, (c) flatness-based control, and (d) sliding mode control.

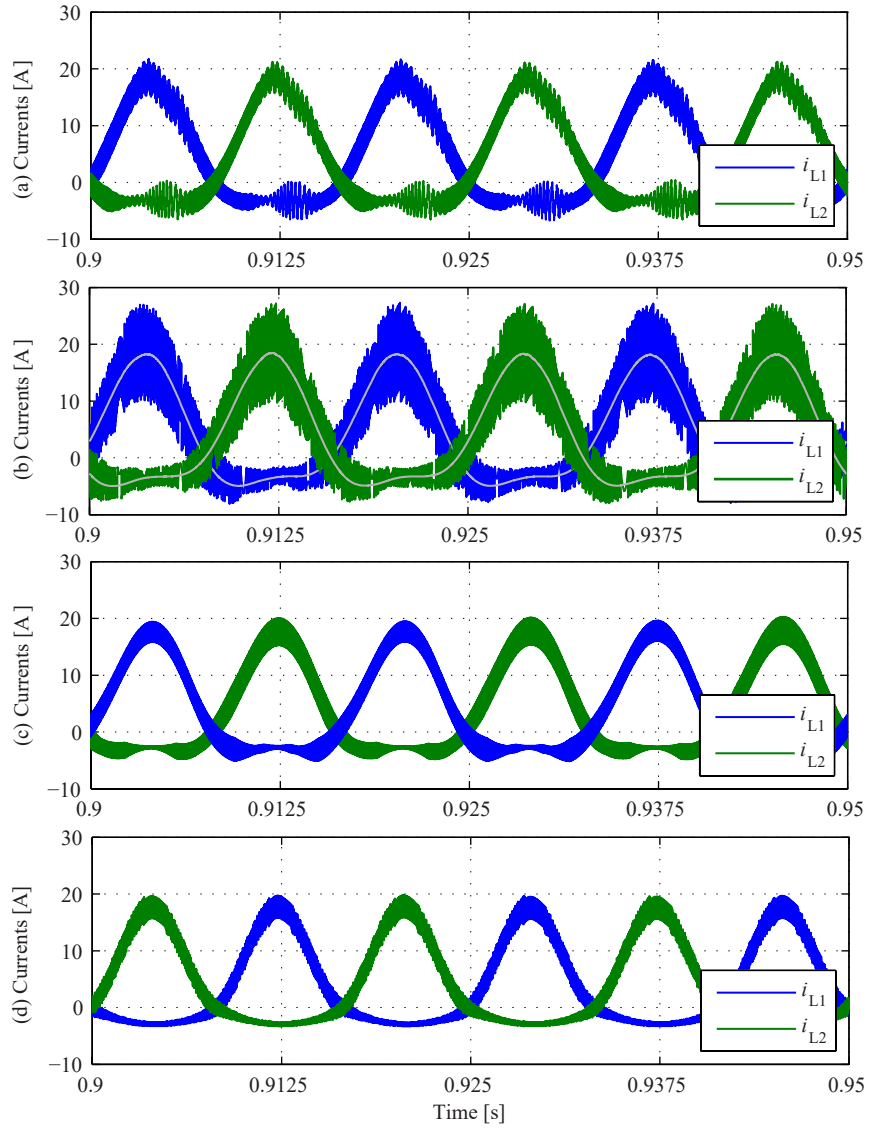


Figure 3.50. Inductor currents with: (a) Linear control, (b) FCS-Model Predictive Control, (c) flatness-based control, and (d) sliding mode control.

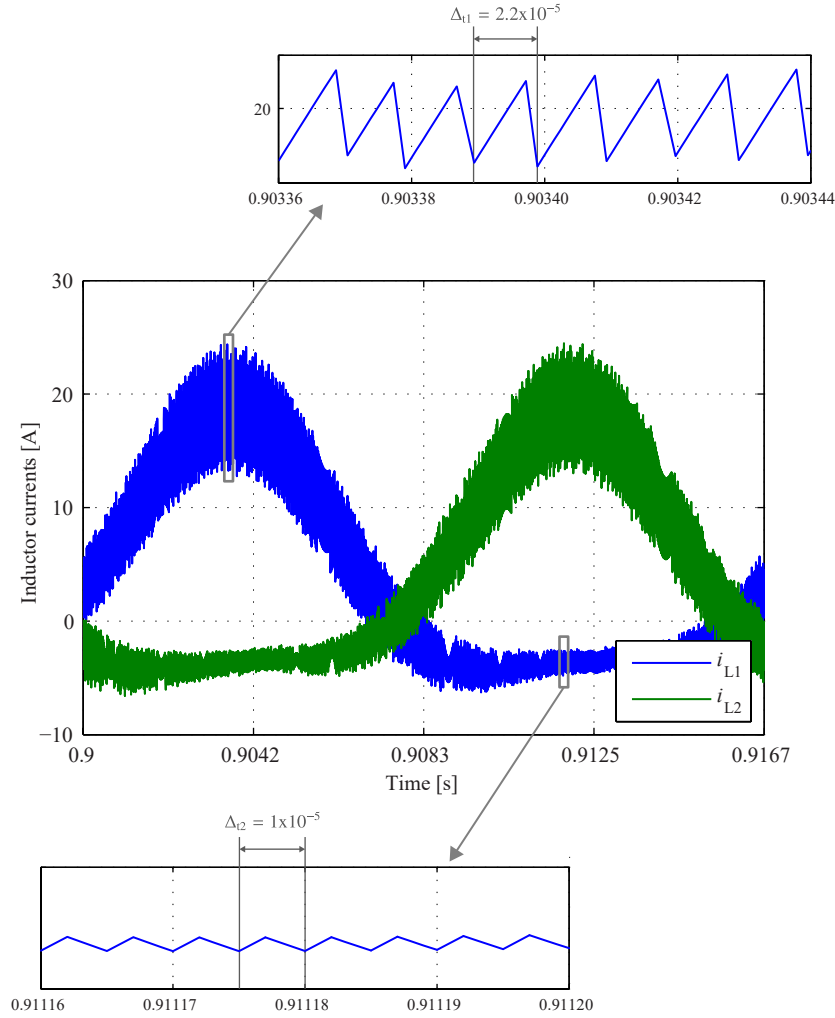


Figure 3.51. Zoom of the inductor currents of the DBI with FCS-Model Predictive Control.

Fig. 3.19(c), 3.28(c), and 3.42(c).

Finally, a summary with the main quantitative parameters of each control strategy is shown in Table 3.8. Also, the main features and waveforms with each control strategy are presented in Table 3.9. The output current of the inverter with the four control strategies complies with the IEEE standard. However, the linear control and the FCS-MPC present the highest THD in regards to the others control strategies. Also, the linear control have the highest number of the control loops to regulate the DBI, and the design and tuning the parameters of the PR controllers are difficult procedures. On the other hand, FCS-MPC presents a variable switching frequency complicating the grid filter design, and the tuning of the weight factor is a non-easy task due to the different dynamics of the control goals

in the cost function. For these reasons, the linear control and FCS-MPC present the worst performance of the four controls proposed. On the other hand, a fixed switching frequency is achieved with the flatness-based control. But, the difficult implementation of the derivatives is the main disadvantage of this control strategy.

Despite the fact that the switching frequency is also variable with the sliding mode control, this proposal presents the best THD of the grid current. Also, the control goals are based on the current regulation of the inverter, which means that fewer sensors are used, since the capacitor voltage v_{c1} , v_{c2} sensors are not required. Considering all the comparison parameters mentioned above, which are resumed in Table 3.8, the sliding mode control is the most attractive control strategy and will be used for experimental validation.

Table 3.8. Main parameters of comparison.

Parameters	Linear control	FCS-MPC	Flatness-based control	Sliding mode control
Total number of control loops	5	2	3	3
Capacitor voltages				
AC component	Sinusoidal	Sinusoidal	Sinusoidal	No sinusoidal
DC component	112.6 V	112.6 V	112.6 V	58 V
Average switching frequency	79060 Hz	79140 Hz	79980 Hz	85680 Hz
Ripple of inductor currents	5.2 A	9.94 A	5.23 A	5.10 A
THD_{i_s}	3.85 %	3.58 %	2.59 %	2.48 %

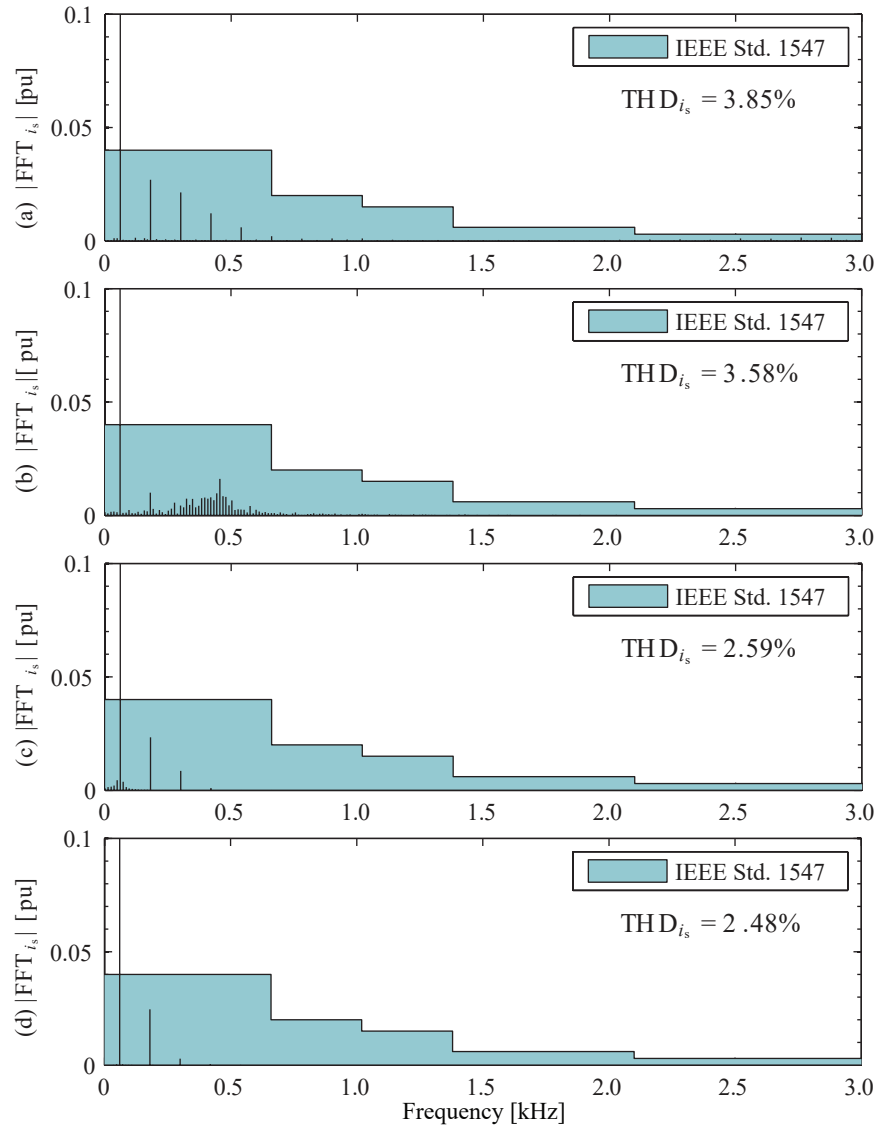


Figure 3.52. Grid current spectrum of DBI at nominal power with: (a) Linear control, (b) FCS-Model Predictive Control, (c) flatness-based control, and (d) sliding mode control.

Table 3.9. Summary of the control strategies for DBI.

	LINEAR CONTROL	FCS-MPC	FLATNESS-BASED CONTROL	SLIDING MODE CONTROL
Features	<ul style="list-style-type: none"> Independent control Control goals: <ul style="list-style-type: none"> Capacitor voltages (v_{c1}, v_{c2}) Inductor currents (i_{L1}, i_{L2}) Transfer function : $C_{PR}(s) = k_p + \frac{2k_i\omega_s s}{s^2 + 2\omega_s s + \omega_o^2}$ DC voltage reference: $V_{cl,dc} = k \times V_{in} + V_{ac} / 2$ 	<ul style="list-style-type: none"> Independent control Control goals: <ul style="list-style-type: none"> Capacitor voltages (v_{c1}, v_{c2}) Inductor currents (i_{L1}, i_{L2}) Cost function: $G = \lambda_1 (i_{L1}^* - i_{L1})^2 + \lambda_2 (u_{c1}^* - u_{c1})^2$ DC voltage reference: $V_{cl,dc} = k \times V_{in} + V_{ac} / 2$ 	<ul style="list-style-type: none"> Independent control Control goals: <ul style="list-style-type: none"> Capacitor voltage through stored energy in L_1 and C_1 Control law: $(\dot{y}_1^* - \dot{y}_1) + k_1 (y_1^* - y_1) + k_2 (y_1^* - y_1) + k_3 \int (y_1^* - y_1) dt = 0$ $u_1 = \phi(y_1, \dot{y}_1)$ $u_2 = \phi(y_2, \dot{y}_2)$ DC voltage reference: $V_{cl,dc} = k \times V_{in} + V_{ac} / 2$ 	<ul style="list-style-type: none"> Global control Control goals: <ul style="list-style-type: none"> Output current Difference between the inductor currents Sliding surface: $\sigma(t) = -k_2(t) + i_{L2}(t) - i_{L1}(t)$ DC voltage reference: $V_{cl,dc} = 2 \cdot V_{in}$
Control scheme				
Reference Tracking				
Grid voltage and current				
Grid current spectrum				

EXPERIMENTAL VALIDATION

Although four different controllers are analyzed and presented in the previous section, only one control strategy is selected to test in the laboratory. The criterias of selection were the simple implementation of the control scheme, the best THD of output current between linear control and the three non-linear strategies, and that the hardware was designed and developed in another project.

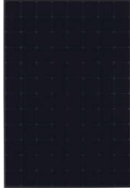


The hardware used for validation of this comparison was based on an experimental prototype developed for a sliding mode project (F82140010). Therefore, part of the hardware was specifically designed to implement the gate drives and pulse through the sliding mode strategy. This part is an analogical circuit, which is included in the designed control board and this item can not be bypass in order to use other control schemes. Hence, the sliding mode strategy was selected.

In addition to this, the components used in the design of the power converter were not originally planned for PV microinverter application. Therefore, the amount of the voltage ratio between the input and output is achievable with the existing parameters, but the spectrum and THD of the grid current obtained are not good. Thus, a new voltage set point was chosen from 70 V input, which is obtained with a fixed DC source. Because of this voltage difference, the results obtained in the previous chapters can not be used for comparisons with experimental results. Therefore, the new simulation results are introduced in the first section of this chapter in order to fully validate the simulation versus experimental part of the prototype.

Although this difference in input voltage might be interpreted as non-microinverter application. There are some PV microinverters with high voltage at input, where innovative technologies for the PV modules can be used. In table 4.1, three different technologies for the solar cell are shown, as the cell built on solid copper foundation of SunPower company [88], the cell based on ultra thin amorphous silicon layers of Panasonic company [89], and the cell with thin film of First solar [90]. Particularly the thin film technology in PV modules usually achieves high PV voltage, such as the PV panel of First Solar Series 4 (FS-4120A-3). Although this voltage operation is not for all types of PV microinverter, it still valid enough to perform a validation.

The purpose of this chapter is to show that the analysis and models used for simulation and comparisons are valid. Therefore, changing the input voltage parameter from 30 V to 70V does not affect the conclusion achieved in the previous chapter.

Table 4.1. PV modules with high voltage at maximum power.

		SunPower SPR-X21-335	Panasonic N330-HIT	First Solar FS-4120A-3
Electrical Data	Nominal Power (P_{MPP})	335 W	330 W	117.5 W
	Voltage at P_{MAX} (V_{MPP})	57.3 V	58.0 V	70.1V
	Current at P_{MAX} (I_{MPP})	5.85 A	5.70 A	1.68 A
	Open Circuit Voltage (V_{OC})	67.9 V	69.7 V	88.1 V
	Short Circuit Current (I_{sc})	6.23 A	6.07 A	1.83 A
	Module Efficiency	21 %	19.7 %	16.3 %
Cell type		Maxeon Solar cell (cell built on a solid copper foundation)	Bifacial cell uses ultra thin amorphous silicon layers	Thin film cell
Number of solar cells		96 monocrystalline Maxeon cells	96 heterojunction solar cells	Up to 216 cells
PV module photo				

4.1 Simulation results with fixed input source

Considering that the level of input voltage for the design of the DBI was 70 V. It is necessary to introduce a brief analysis of the DBI with this new operating point. Therefore, the inverter with a fixed input source shown in Fig. 4.1 is simulated.

The control strategy is exactly the same used in section 3.5. The only difference is that the control scheme does not present the PV voltage control loop, as illustrated in Fig. 4.2. The external control loop regulates the output current, this loop is based on the PR controller, in which an integral term is inserted into to avoid a DC component in the output current of the inverter. Also, a phase compensator is introduced in this control loop to add the phase margin, as it can be seen in Fig. 4.3. Then, the internal control loop regulates the difference of the inductor currents.

To evaluate the performance of the sliding mode control with this new condition, the DBI with a fixed input source is simulated in the PLECs software. The main parameters of the DBI and its control are listed in Table 4.2. First, the steady-state operation of the inverter is presented. Then, two dynamic tests are designed to show the effect of perturbations in each variable.

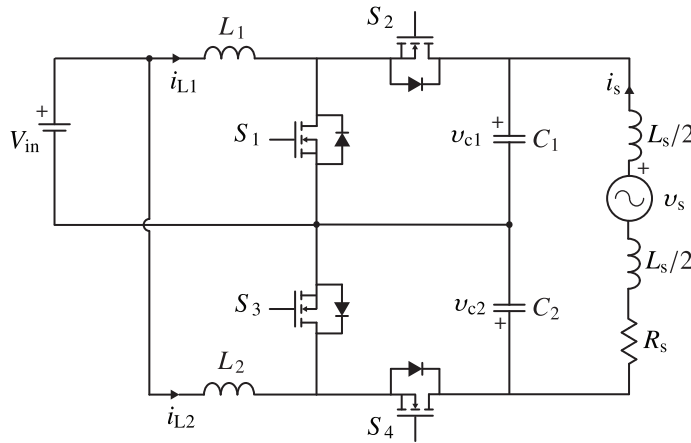


Figure 4.1. Dual boost inverter topology with 70 V input.

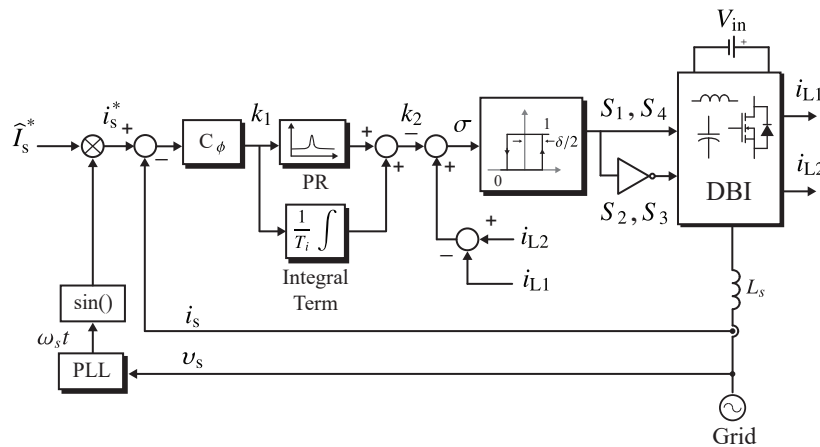


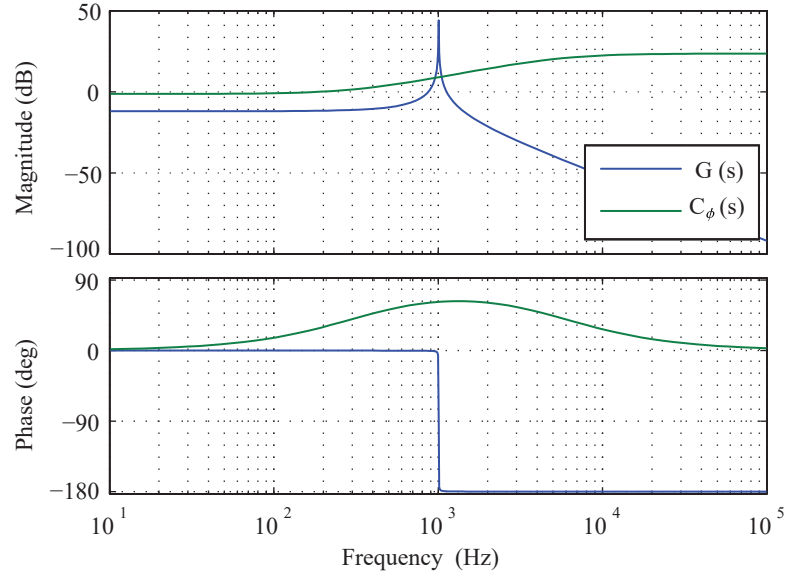
Figure 4.2. The cascaded control scheme of the grid-connected DBI with 70 V input.

4.1.1 Steady-state operation in simulation

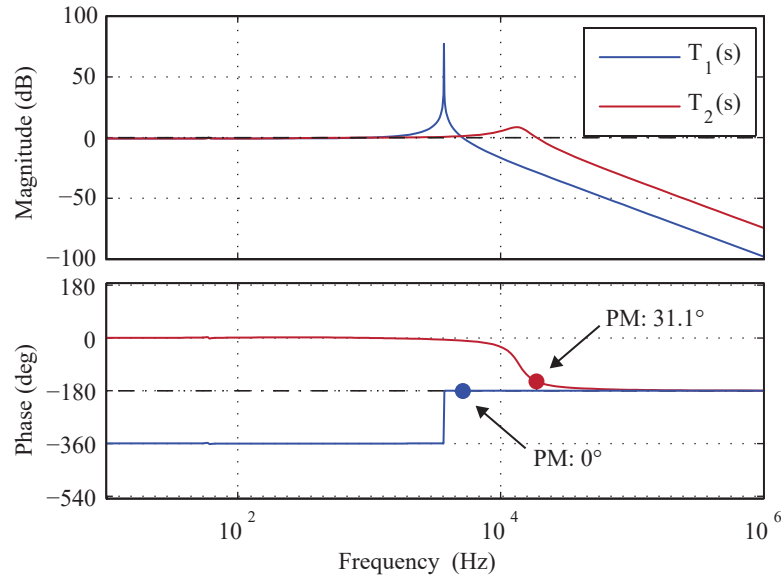
The first simulation results introduce the inverter operation under the steady-state, when the input power is 110 W and the grid current is 1 A. The waveforms of the main variables are presented in Fig. 4.5. Please recognize that, three periods of each variable are considered.

Fig. 4.5(a) shows the capacitor voltages v_{c1} and v_{c2} , which consist of DC and AC components. The DC voltage is the double of the input source as expected, i.e 140 V. The amplitudes of these voltages are equal and their phases are opposite. The waveforms of the capacitor voltages are not sinusoidal, but the difference between v_{c1} and v_{c2} is pure sinusoidal. On the other hand, the inductor currents i_{L1} and i_{L2} are presented in Fig. 4.5(b), where it can be seen that the amplitude of the currents is the same of each boost converter.

The tracking of the grid current reference (i_s^*) was achieved, as it can be observed in Fig. 4.5(d). Also, the grid current i_s is shown in Fig. 4.5(e) together with the grid voltage v_s ,



(a)



(b)

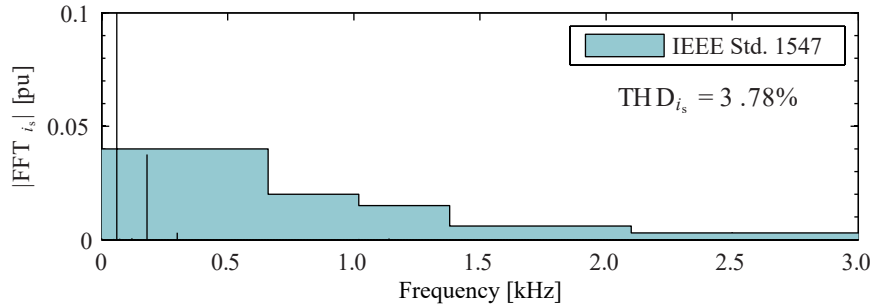
Figure 4.3. Bode diagrams: (a) plant and phase compensator, (b) closed-loop without and with the phase compensator of the DBI with 70 V input.

Table 4.2. Simulation parameters of the sliding mode control for DBI with 70 V input.

Symbol	Parameter	Value
Grid Parameters		
v_s	Grid voltage	110 V_{rms}
f_s	Grid frequency	60 Hz
L_s	Grid filter inductance	10 mH
Converter Parameters		
V_{in}	Input voltage	70 V
L_1, L_2	Inverter inductors	55 μ H
C_1, C_2	Inverter capacitors	5 μ F
Control Parameters		
k	Gain of C_ϕ	2
k_p	Proportional gain of PR	5
k_i	Resonant gain of PR	700
ω_c	Cut-off frequency of PR	5 rad/s
a	Zero of phase compensator	2000
b	Pole of phase compensator	35.000

where it is possible to identify that the two waveforms are in phase.

Finally, the power quality is analyzed by the spectrum and THD of the grid current. The harmonics of the grid current are exposed in Fig. 4.4, where the third harmonic is strongest. However, all harmonics are within limits of the IEEE standard 1547. Also, the grid current shows a THD of 3.78 %.

**Figure 4.4.** Simulation results: Grid current spectrum of sliding mode control for DBI with 70 V input.

4.1.2 Dynamic tests in simulation

To verify the effectiveness of the sliding mode control for DBI, two scenarios are introduced. The first scenario consists of the variations in the reference of the grid current. And the other scenario shows the performance of the inverter under a change of the grid voltage amplitude.

The Fig. 4.6 shows two variations in the reference of the grid current to analyze the dynamic response of the control under perturbations. At time $t = 0.1$ s, the first variation

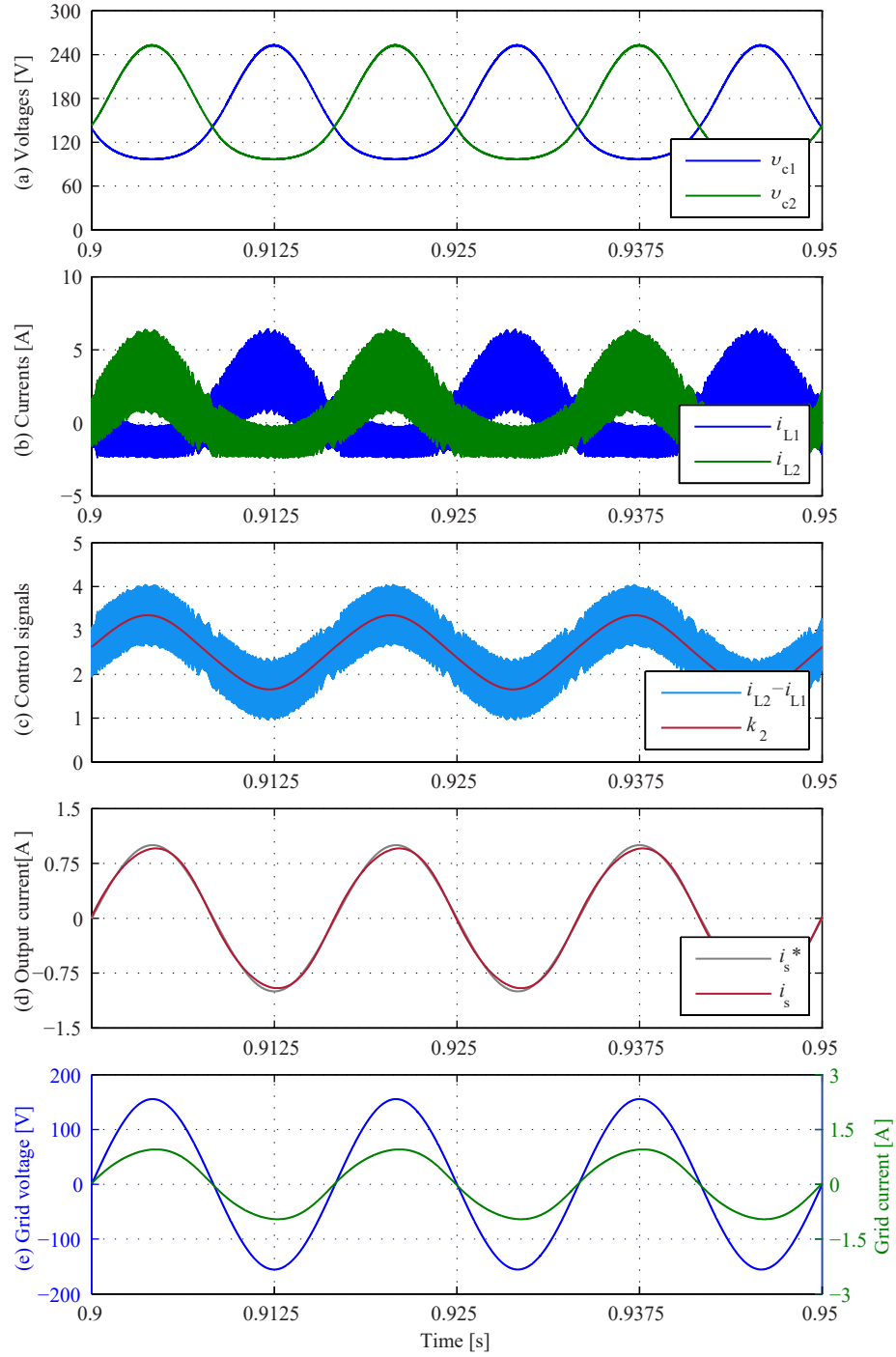


Figure 4.5. Simulations results of sliding mode control for DBI with 70 V input: a) Capacitor voltages, b) inductor currents, c) control signals, and d) grid current and voltage.

is introduced, where the amplitude of the grid current is reduced of 1 A to 0.8 A. While, the second variation is made at $t = 0.2$ s, in which the amplitude of the grid current is incremented of 0.8 A to 1 A. For both tests, the grid current follows its reference at any time, as shown in Fig. 4.6(d). Also, a fast response of the control proposed is identified (Please see Fig. 4.6(c)).

On the other hand, the main effect of these tests can be seen in the currents of the inductors, where the amplitudes of i_{L1} and i_{L2} change depending on the operating points, as illustrated in Fig. 4.6(b). Note that, the voltage of the capacitors shown in Fig.4.6(a) in both tests is kept constant.

The simulation results of the second scenario are presented in Fig. 4.7. The main goal of this test is to evaluate the robustness of the control proposed, for which a transition in the amplitude of the grid voltage is introduced at time $t = 1.5$ s. In the Fig. 4.7(e), it is possible to identify that the amplitude of grid voltage changes from $88 V_{\text{rms}}$ to $110 V_{\text{rms}}$. As expected, the amplitude of the capacitor voltages (see Fig. 4.7.(a)) also increments. However, the grid current is kept constant under this change. Thus, the robustness of the control is verified.

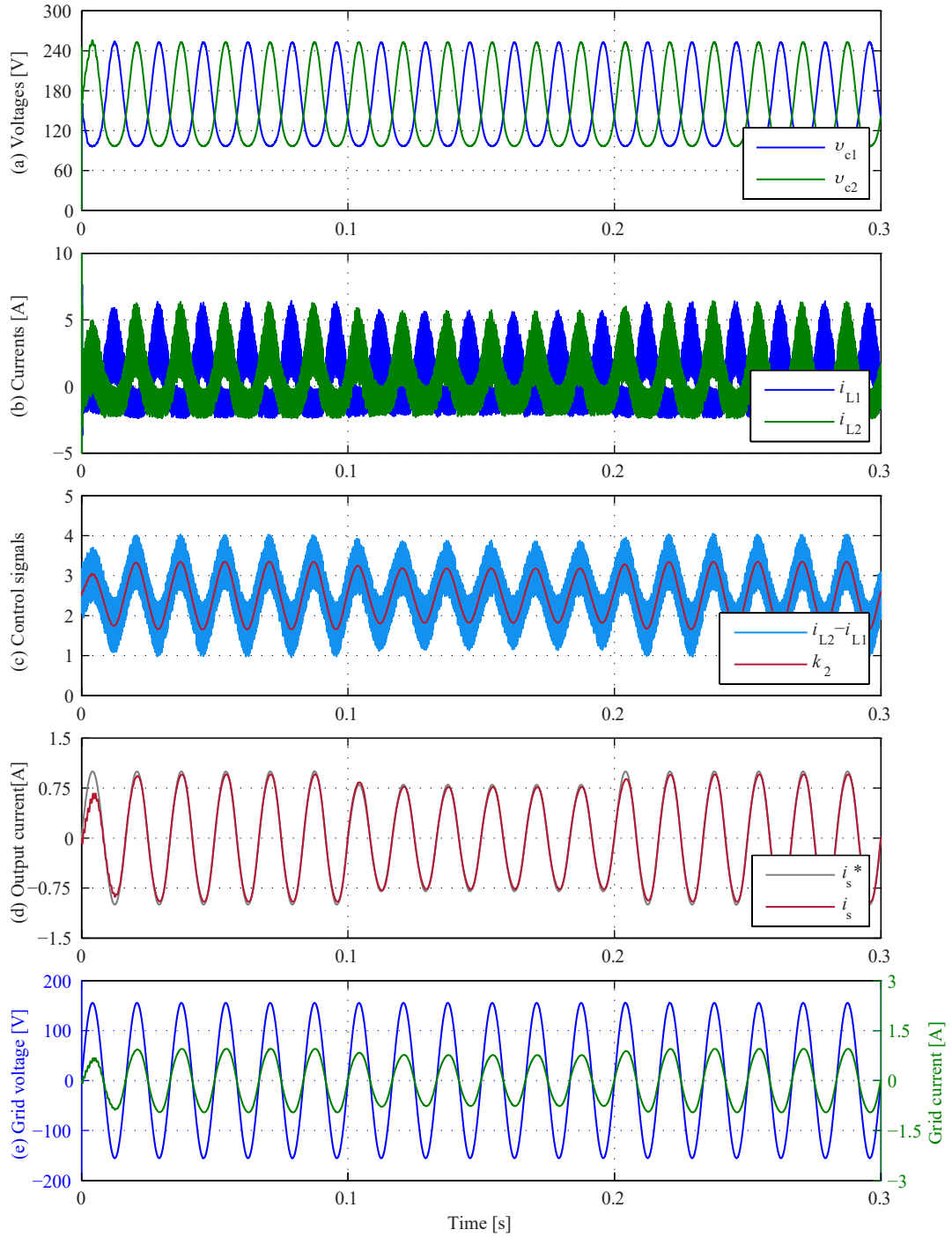


Figure 4.6. Dynamic simulation results of sliding mode control for DBI with 70 V input under variations in the grid current reference: a) Capacitor voltages, b) inductor currents, c) control signals, d) reference and measurement of grid current, and e) grid current and voltage.

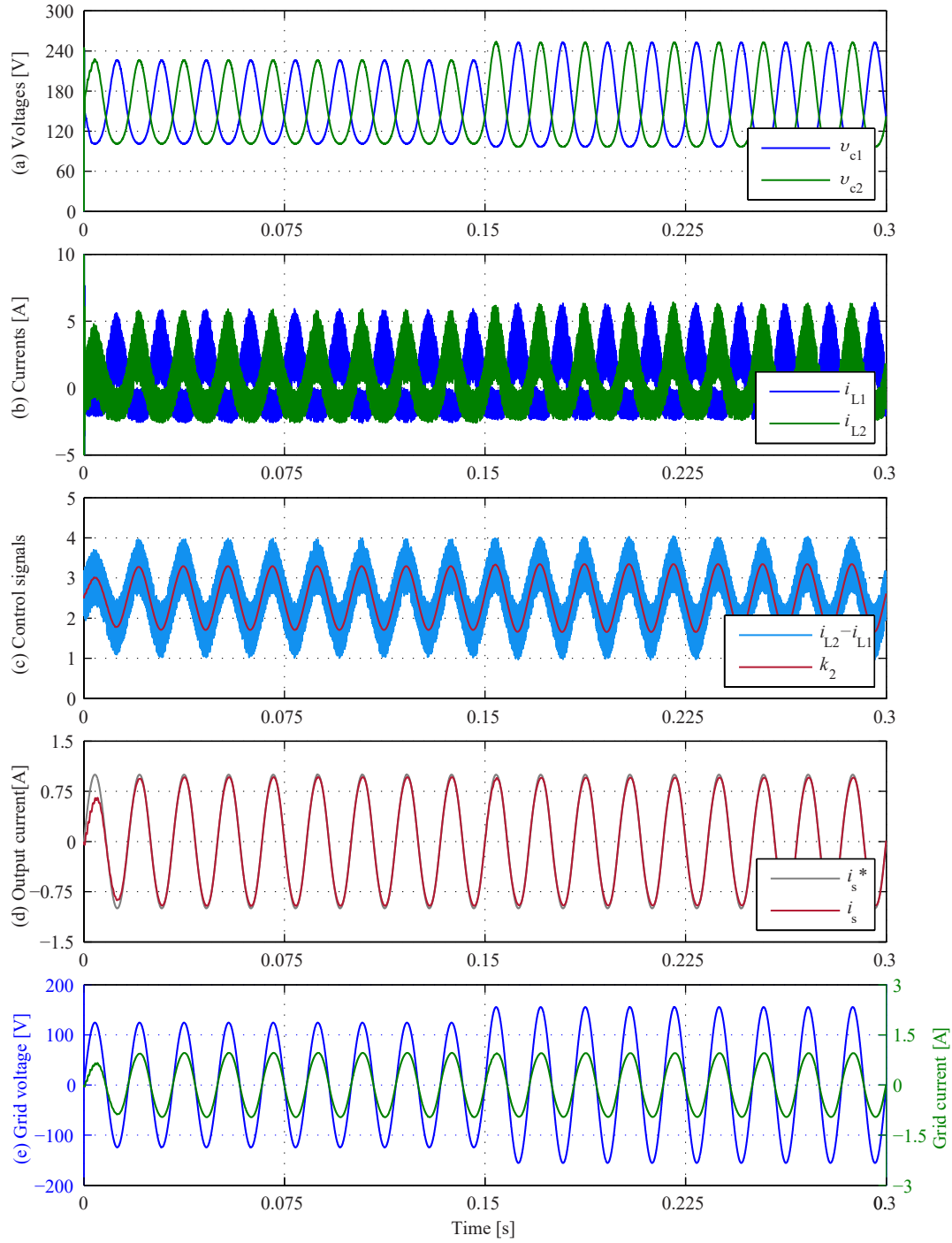


Figure 4.7. Dynamic simulation results of sliding mode control for DBI with 70 V input under grid perturbation: a) Capacitor voltages, b) inductor currents, c) control signals, d) reference and measurement of grid current, and e) grid current and voltage.

4.2 Experimental setup

The proposed control for the DBI is validated using the experimental setup shown in Fig. 4.8. The experimental prototype is composed of the power and control parts.

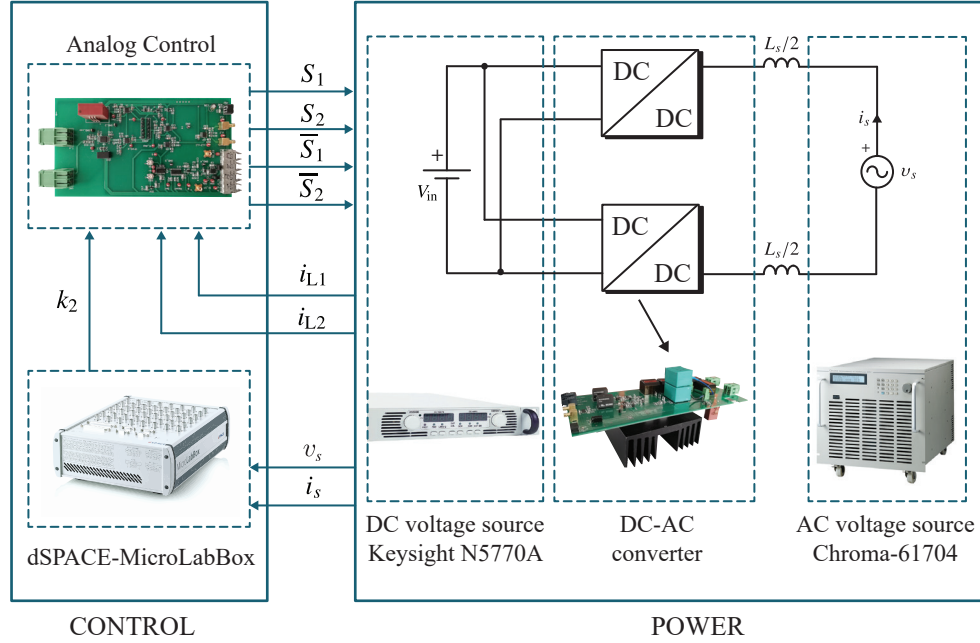


Figure 4.8. Experimental diagram of dual boost inverter.

4.2.1 Power stage

In the power part, two DC–DC boost converters have been connected in differential mode, the differential output is connected to the grid through a line filter.

The nominal power of each DC–DC converter is 1 kW. The bank of the inductors is composed by 5 inductors in series of 11 μH . The part number of the inductor is HA55-3023130LF. The main specifications are the rated and saturation currents, which are 37 A and 40 A, respectively. In addition, the output capacitor of each DC–DC converter is 5 μF with 900 V of rated voltage. Notice that, the phase leg SiC MOSFET power module (part number: APTMC120AM55CT1AG) of Microsemic is used. The nominal parameters of the setup are summarized in Table 4.3.

The used input voltage source is a DC voltage source (Keysight N5770A) operating at 70 V_{DC}, while the grid has been emulated using an AC source (Chroma 61704) operating at 110 V_{rms}/60 Hz. Also, a power resistor of 147 Ω is used in parallel in order to obtain the regenerative operation.

The electrical measurements for the control are composed by four signals: three currents and one voltage. Each power board has one circuit for the current measurement (inductor current), which is based on LEM sensor model T60404-N4646-X762 of the Vaccumschmelze

manufacture. The main parameters of this sensor are 15 A of the primary nominal current and ± 51 A of the maximum measuring range. The other two measurements are the grid side signals (current and voltage), which are adapted on the control board. The grid current measurement as the same of the others two inductor currents is based on a LEM sensor. The LEM sensor model for this measurement is T60404-N4646-X653 of the same manufacture as others. In this case, the primary nominal current is 6 A and the maximum measuring range is ± 20 A. While, the grid voltage measurement is based on low-noise operational amplifiers (OPA376) and isolation amplifiers (ACPL-C79A). All measurement signals are adjusted according to operation conditions through operational amplifiers. Then, the coaxial cables are used to connect the output sensors and operational amplification to the DSpace-MicroLabBox analog inputs.

Table 4.3. Main parameters of the experimental setup.

Symbol	Parameter	Experimental Value
Grid Parameters		
v_s	Grid voltage	110 V_{rms}
f_s	Grid frequency	60 Hz
L_s	Grid filter inductance	10 mH
Converter Parameters		
V_{in}	Input voltage	70 V
C_{in}	Input capacitor	12000 μF
L_1, L_2	Inverter inductors	55 μH
C_1, C_2	Inverter capacitors	5 μF

4.2.2 Control section

Conventional control systems for power converters are implemented using digital platforms such as DSP and FPGA, due to their fast computational times. On the other hand, sliding mode control is commonly implemented with analog circuits because a hysteresis comparator is used to achieve a finite switching frequency. In this work, a hybrid implementation is proposed taking the advantages of both types of implementation. The phase compensator and PR controller are implemented in a DSpace MicroLabBox platform using Matlab/Simulink, while an analog circuit is used to implement the sliding mode inner control loop, which controls the current in the boost converters. The parameters of the control strategy are shown in Table 4.4.

The main parameters of the MicroLabBox platform control [91] are presented in the Table 4.5. In this platform, the phase compensator is implemented through the *Discrete Transfer Fcn* block of Matlab/Simulink. Instead, the discrete model of the PR controller with anti-windup are programmed in C using the *S-Function Builder* block, due to the fact that the implementation with block of the PR controller is a difficult task. The Second-Order Generalized Integrator Phase-Locked-Loop (SOGI-PLL) used to synchronize the current reference with the grid is implemented with several blocks of the Matlab/Simulink. Furthermore, three I/O channels are used: the grid voltage measurement and grid current measurement are obtained with two ADC channels of the platform control and the one DAC channel is used to obtain the output of the PR regulator.

Table 4.4. Main parameters of the sliding mode control strategy.

Symbol	Parameter	Experimental Value
k	Gain of C_ϕ	1
k_p	Proportional gain of PR	50
k_i	Resonant gain of PR	700
ω_c	Cut-off frequency of PR	5 rad/s
a	Zero of phase compensator	2000
b	Pole of phase compensator	35,000

Additionally, an Human Machine Interface (HMI) implemented in the software ControlDesk is designed to adjust and operate different parts of the DBI. The HMI allows to charge the input capacitor, adjust some parameters of the control (Gain of C_ϕ , proportional gain of PR, resonant gain of PR and the amplitude of the grid current reference), and identify which protection is active through visual alarms in the panel.

Table 4.5. The main parameters of MicroLabBox.

Parameters	Description
Real-time processor	Freescall P5020 processor has dual-core with 2 GHz CPU clock
Input/Outputs	
Parallel ADCs	24 channels x 16-bit resolution, a sample rate of 1 MSPS 8 channels x 14-bit resolution, a fixed sample rate of 10 MSPS
DACs	16 channels x 16-bit resolution, a maximum settling time (to 1 LSB) of 1 μ s
Digital I/Os	48 bidirectional channels 12 bidirectional channels are used by some features of the electric motor control
Peripheral	
PWM Unit	48 bidirectional channels, adjustable voltage level for the output: 2.5 V, 3.3 V, 5.0 V

The control board is composed by the analog circuit to implement of the sliding mode controller, the dead time circuit of the power devices (SiC-MOSFETs) and the adaptation of the grid measurements. Fig. 4.9 shows the schematic diagram of the analog implementation of the sliding mode controller, where two operational amplifiers are used to generate the switching surface, while the hysteresis is achieved through a comparator LM319 and a J-K Flip-Flop (MC14027B integrated circuit). The hysteresis boundaries given by the voltage signals are regulated through variable resistors.

4.3 Experimental results

In this section, the operation of the sliding mode control for DBI connected to the grid is presented. The experimental tests are divided into two: steady-state operation and dynamic tests.

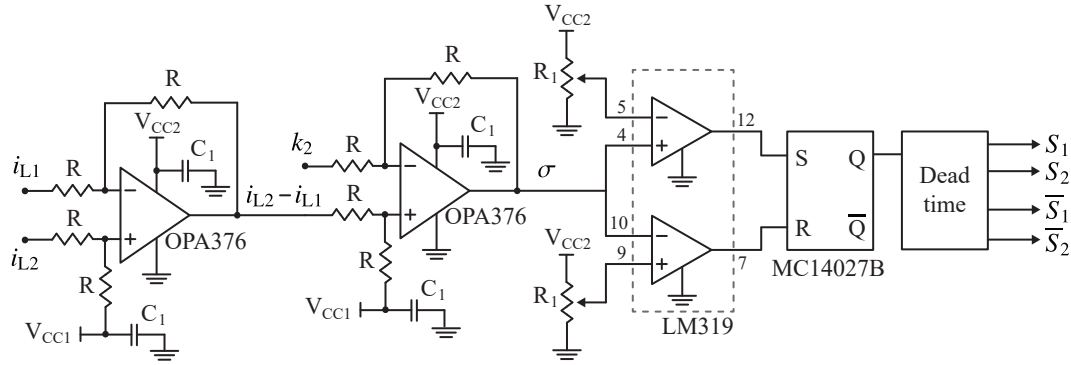


Figure 4.9. Analog circuit for control stage, where $R = 20 \text{ k}\Omega$, $R_1 = 10 \text{ k}\Omega$, $V_{CC1} = 2.5 \text{ V}$, $V_{CC2} = 5 \text{ V}$ and $C_1 = 0.1 \text{ }\mu\text{F}$.

4.3.1 Steady-state operation

To validate the behavior of the sliding mode control, the converter is tested when it is working on the selected operation point, consisting in 1 A in the grid current reference. The experimental results under steady-state operation are shown in Fig. 4.10.

The grid current reference i_s^* and current measurement i_s of the DBI are presented in Fig. 4.10(a), where it is possible to verify that accurate tracking of the current reference is achieved by the PR controller. The angle of the reference was extracted from the grid voltage v_s , which is shown in Fig. 4.10(d). The output of this external control loop k_2 is the reference for the difference between the inductor currents, which can be seen in Fig. 4.10(a).

Fig. 4.10(b) shows the voltage of the capacitors and currents in the inductors, which are balanced despite not being directly controlled. Please note that the magnitudes of the DC and AC components of the output voltage and inductor current of each DC–DC converter are the same. In the case of the voltages, the DC component of the capacitor voltage is 140 V, which is the double of the input voltage (V_{in}). The maximum value of the amplitude of AC component is around 110 V, and the phases of these voltages are shifted by 180° .

From Fig. 4.10(c) it can be seen that the output voltage of the inverter is sinusoidal, despite the voltage of each capacitor is not purely sinusoidal. Additionally, the condition of proper operation of the inverter ($v_o > v_s$) is fulfilled, because the output voltage of the inverter is around $111 \text{ V}_{ac,rms}$, which is higher than the grid voltage (110 V_{rms}).

Fig. 4.10(d) presents the grid current (i_s) and voltage (v_s), together with the output voltage and current through the inductance of one of the DC–DC converters. The grid current is very close to a sinusoidal waveform and is always in phase with the grid voltage to ensure the power factor close to unity.

The spectrum and total harmonic distortion (THD) of the grid current in the steady-state were obtained to analyze the power quality. These results are presented together with the limits of the IEEE standard 1547 in Fig. 4.11. Note how the harmonics present in the grid current comply with the standard. The total harmonic distortion obtained for the grid current is 4.47 %. This is a very good result, considering this is the first iteration of a laboratory prototype (stray inductances and other circuit components have not been optimized), and a simple inductive filter was used for grid connection. The harmonic content could be improved

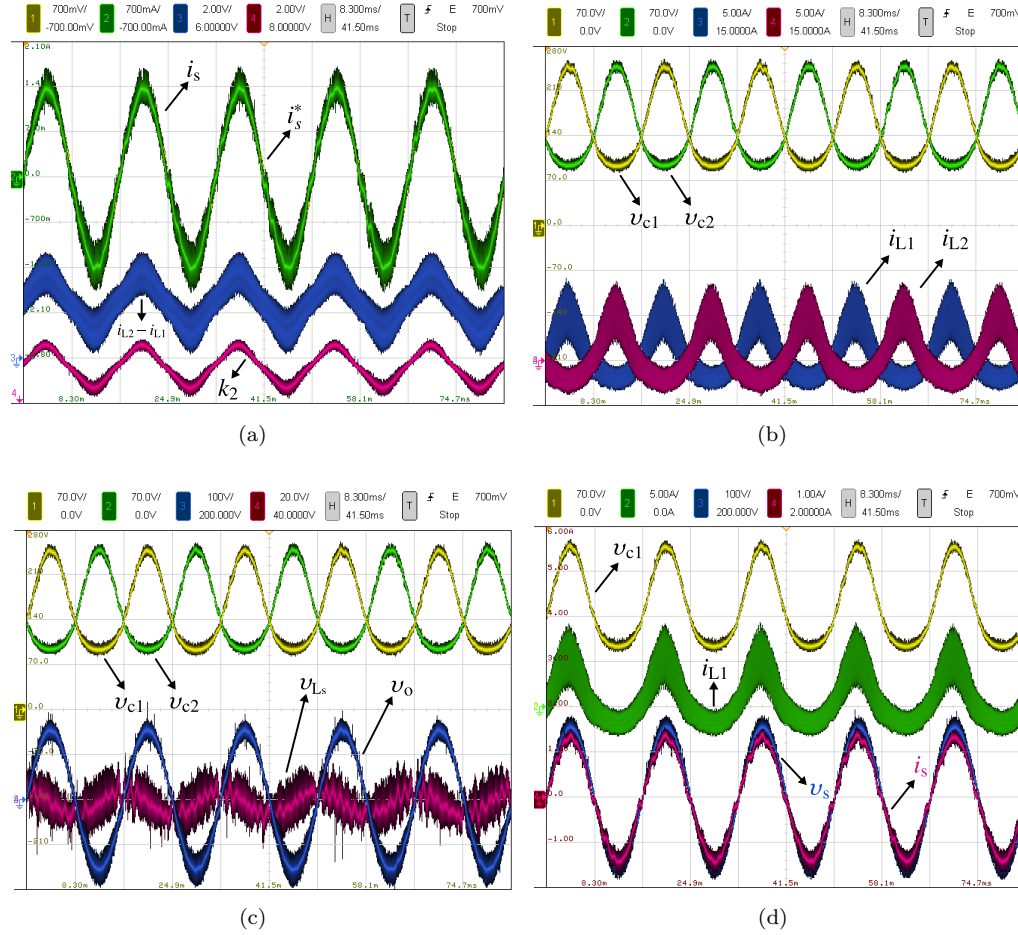


Figure 4.10. Experimental results with grid connection and input voltage of 70 V: (a) reference and measurement of grid current, difference of the inductor currents and output of outer control loop (k_2), (b) voltage of the capacitors (v_{c1} , v_{c2}) and current through the inductors (i_{L1} , i_{L2}), (c) voltage of the capacitors (v_{c1} , v_{c2}), voltage of the line filter, output voltage (v_o) and (d) v_{c1} , i_{L1} , grid voltage and current.

further with higher order filters (such as LC or LCL), typically used in such applications.

4.3.2 Dynamic tests

Two tests were performed to evaluate the dynamic performance of the proposed sliding mode control method. The first test consists of a step-down and a step-up in the output (grid) current reference (i_s^*) to assess the tracking performance. The second test consists on applying a voltage dip in the grid voltage (v_s) to assess the performance under system perturbations. Fig. 4.12(a) shows the experimental results associated with the step-down (1.0 to 0.8 A) in the grid current reference, while Fig. 4.12(b) presents the results obtained for the step-up (0.8 to

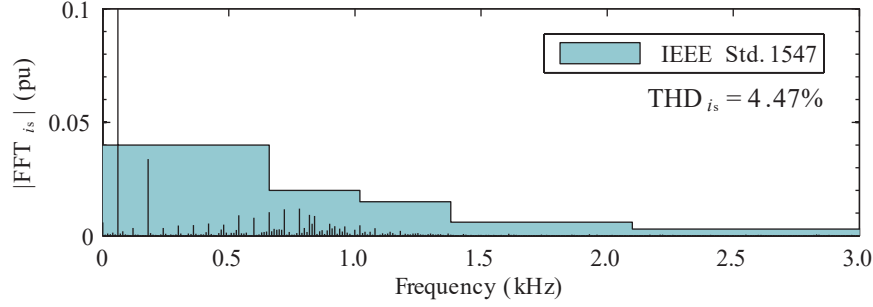


Figure 4.11. Grid current spectrum with 70 V of input voltage.

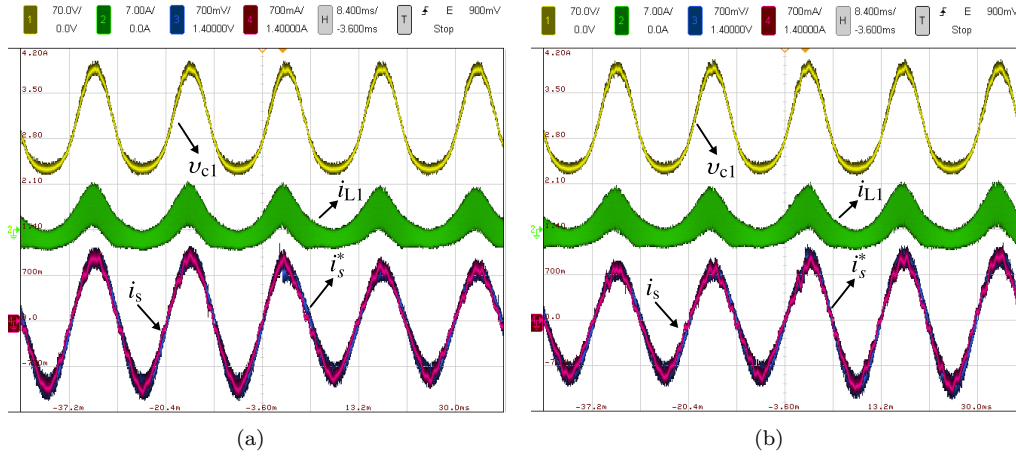


Figure 4.12. Experimental results under variations in the output current reference (voltage of the capacitor C_1 (v_{c1}), current through the inductor L_1 (i_{L1}), reference (i_s^*) and measurement (i_s) of grid current): (a) Step-down in the output current reference, and (b) Step-up in the output current reference.

1.0 A) in the grid current reference. As illustrated by both figures, a fast dynamic behavior is achieved by the proposed sliding mode control method, where the tracking of the grid current reference is promptly accomplished. As a result, the grid current variations are reflected in the amplitude of the current through the inductor i_{L1} (and i_{L2}); however the voltage of the capacitor v_{c1} (and v_{c2}) in both cases is kept constant. Both step changes were introduced at the peak value of the current reference, to evaluate the most demanding dynamic scenario for the controller.

For the second dynamic test, shown in Fig. 4.13, a voltage dip of 20 % was introduced in the grid voltage (only the transition from voltage dip to nominal voltage is shown). The grid voltage amplitude transitions from 88 to 110 V_{rms}. This generates an increase of the AC component in the voltage of both output capacitors (v_{c1} and v_{c2}), while the grid current i_s remains controlled without reflecting any change caused by this perturbation, highlighting the robustness of the proposed control method. However, since the inductor current i_{L1} (and

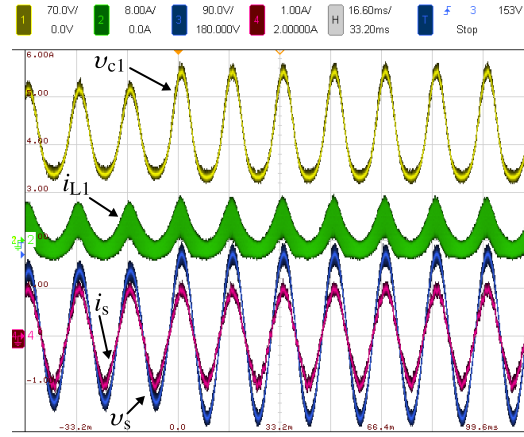


Figure 4.13. Experimental dynamic performance under grid perturbation (from 20 % voltage dip to nominal voltage): voltage of the capacitor C_1 (v_{c1}), current through the inductor L_1 (i_{L1}), measurement of grid current (i_s), and grid voltage (v_s).

i_{L2}) depends on the difference between the input voltage v_{in} and the voltage in each output capacitor, a small variation is experienced by i_{L1} and i_{L2} . Please note that during this test the output (grid) current reference was kept constant.

4.3.3 Discussion

In this chapter the simulation and experimental results of the sliding mode control for the DBI with 70 V input were presented.

The experimental results show the performance of the sliding mode control method for a grid-connected DBI. The capacitor voltage and inductor current of each DC-DC converter are balanced despite not having a direct control of them, confirming the results obtained in the simulations.

The capacitor voltages are composed by the DC and AC components, where the DC component is twice the input voltage, as expected. The waveforms of the inductor currents present a negative part due to the power circulating generated by the differential connection.

On the one hand, the good reference tracking demonstrated the effectiveness of the sliding control approach. On the other hand, the power quality showed good performance despite using only an inductive filter for grid connection. The THD of the output current obtained in the experimental validation was 4.47 %, which is higher than the value obtained in simulations (3.78 %) due to the parasitic elements present in the experimental prototype. However, this parameter is within the limit of the AC grid requirements.

In addition, the sliding mode control method was also tested under dynamic conditions in the current reference and under grid voltage perturbations, achieving good performance in both cases, where the robustness of the control strategy is verified, as presented in simulations, i.e., when the amplitude of the grid voltage increased from 88 to 110 V_{rms} , the capacitor voltages also increased, but the grid current is not changed. On the other hand, the capacitor voltages remain fixed despite a change in the reference of the output current occurs.

CONCLUSIONS

After having analyzing all the items developed in this research, a classification of PV microinverters topologies found in the academic and industrial field is proposed. In this categorization, four architectures were identified and analyzed, where the unfolding inverter is the most used in the industry since it presents some advantages as high efficiency and easy control. Also, the single-stage topologies for PV microinverter have been widely studied in the literature, because to elevate the PV voltage and inject AC power into the grid, only one stage of the power conversion is used. And the efficiency could be increased. However, one challenge of this single-stage topologies is their control.

Moreover, the typical topology found in the single-stage architecture is the dual boost inverter (DBI), which the outputs of the DC-DC converters are connected in differential mode. Although the efficiency is low, this converter was used to study different control schemes.

Therefore, in this theses three non-linear control strategies for the dual boost inverter were analyzed, developed and validated with simulations. Also, these proposed controls could be implemented in other single-stage topologies, as dual boost inverter with coupled inductors, because some issues and constraints of the control are originated from the differential connection.

A review of the controls techniques used to regulate the DBI was presented, noticing that the design of the linear control is a difficult task, because all the variables of the converter are composed by DC and AC component, making the operation point to present large variations. Also, few works with experimental validations of linear control schemes for grid-connection of the inverter are found in literature. For these reasons, three non-linear strategies were proposed for the DBI in this thesis and were compared with the linear control. From this investigation, the main conclusions of each control strategies obtained from theoretical analysis, simulations and experimental tests are:

- *Finite Control Set-Model Predictive Control*: Although, the total harmonic distortion and harmonics presented on the output current of the DBI with FCS-MPC comply with the standard, several disadvantages of this control strategy limit its implementation. One drawback is that the switching frequency is variable due to the absence of a modulator stage. Also, to achieve the average switching frequency selected in the design for the comparison, the sampling time required is very small. Therefore, a trade-off between the switching frequency and THD is required. On the other hand, the selection of the weighting factors is a non-trivial task, because the cost function is composed by two control objectives with different dynamics and variation ranges.

- *Flatness-based control*: The non-linear control based on the stored energy regulation of capacitors and inductors was achieved because each DC-DC converter is a flat system. The analytic expression of the system variables in function of the flat output and its derivatives was obtained in order to control the inverter. The simulation results showed that during transients and steady-state, the current and voltage regulation are attained. On the other hand, an advantage founded, is that the total harmonic distortion of the grid current with flatness-based control was 2.59 %. Thus, another advantage of this control strategy is that the switching frequency is fixed. However, the main challenge is its implementation since it is difficult to obtain an appropriate derivative action.
- *Sliding mode control*: The control strategy proposed is based on the current regulation of the inverter. The sliding surface proposed for this strategy was the difference between the inductor currents that regulates indirectly the output voltage of the dual boost inverter. Although the switching frequency is also variable, the performance of the output current obtained with sliding mode control is better than the behavior obtained with FCS-MPC, as shown in Chapter 3. Nevertheless, finding a model based on the sliding surface was a difficult process.

From the analysis obtained of each non-linear control method and the linear control, two strategies present a better performance; these are flatness-based control and sliding mode control. The main parameters used for selecting an appropriate control for the inverter are the averaged switching frequency, the harmonic spectrum of the output current of the DBI and the number of control loops. The THD obtained for both controls complies with the standard and the percent values are very similar. For flatness-based control, the THD was 2.59 % in the nominal conditions, and this value was 2.48 % with sliding mode control. The implementation was the feature that made the difference. Each control strategy has some advantages and disadvantages for the regulation of the DBI. However, the feature that made the difference was the control objectives, because fewer sensors are used in sliding mode control due to the fact that the voltage of the capacitors is indirectly regulated. Therefore, sliding mode control is the most promising alternative for the single-stage topologies.

As a consequence of the non-linear control analysis for the DBI, the sliding mode control proposed has been implemented experimentally. The THD of the grid current obtained was 4.47 %, which complied with the IEEE Standard 1547. However, the implementation and tuning of the parameters of this control strategy was complex because it was necessary to use a hybrid platform. The hysteresis comparator was implemented through analog circuits, while the PR controller with the phase compensator was executed in a digital platform. Therefore, the next step in the design of this type of control is to integrate all parts in a digital platform.

5.1 Future work

Three non-linear control strategies were developed in this thesis for the dual boost inverter. However, the main disadvantage of this inverter is its low efficiency. For this reason, the next step of this research is to use and adapt the non-linear control proposals in another single-stage inverter topology, such as topologies with bypass connection or coupled inductors, since the main issues solved by the control proposals for the dual boost inverter are particular to the single-stage topologies and not specifically of the DBI.

Another important approach derived from this work is to integrate the single-stage boost inverter in the architecture composed by two-stage power converters. In this case, the effort

of elevation could be distributed between two converters, which could improve the efficiency. A brief analysis about this idea was published in a conference paper by the author, where the elevation range distribution between the two set-up stages improved the global efficiency of the topology. However, this analysis was made with the DBI. Therefore, it is necessary to do a more detailed study based on this idea with other step-up inverter topologies.

Finally, from the experience obtained of the control implementation, another open work is to develop and build a digital platform to validate the different control strategies for the single-stage topologies.

PUBLICATIONS DERIVED FROM THIS RESEARCH

The following publications have been partially or completely derived from the research of this thesis.

A.1 Journal publications

1. Lopez-Caiza, D.; Flores-Bahamonde, F.; Kouro, S.; Santana, V.; Müller, N.; Chub, A., "Sliding Mode Based Control of Dual Boost Inverter for Grid Connection", *Energies* 2019, 12, 4241.

A.2 Part of book

1. Luis Martinez-Salamero (Ed.), "Sliding Mode Control of Power Converters in Renewable Energy Systems", June 2020, Pages: 344.

A.3 International conference publications

1. D. L. Caiza, S. Kouro, F. Flores-Bahamonde and R. Hernandez, "Unfolding PV Microinverter Current Control: Rectified Sinusoidal vs Sinusoidal Reference Waveform," 2018 IEEE Energy Conversion Congress and Exposition (ECCE), Portland, OR, 2018, pp. 7094-7100.
2. D. Lopez, H. Renaudineau, F. Flores-Bahamonde and S. Kouro, "Evaluation of photovoltaic microinverter configurations based on different converter stages and step-up voltage ratios," 2017 19th European Conference on Power Electronics and Applications (EPE'17 ECCE Europe), Warsaw, 2017, pp. P.1-P.8.
3. D. Lopez, F. Flores-Bahamonde, H. Renaudineau and S. Kouro, "Double voltage step-up photovoltaic microinverter," 2017 IEEE International Conference on Industrial Technology (ICIT), Toronto, ON, 2017, pp. 406-411.
4. H. Renaudineau, D. Lopez, F. Flores-Bahamonde and S. Kouro, "Flatness-based control of a boost inverter for PV microinverter application," 2017 IEEE 8th International

Symposium on Power Electronics for Distributed Generation Systems (PEDG), Florianopolis, 2017, pp. 1-6.

5. D. Lopez, F. Flores-Bahamonde, S. Kouro, M. A. Perez, A. Llor and L. Martínez-Salamero, "Predictive control of a single-stage boost DC-AC photovoltaic microinverter," IECON 2016 - 42nd Annual Conference of the IEEE Industrial Electronics Society, Florence, 2016, pp. 6746-6751.

REFERENCES

- [1] Renewable Energy Policy Network for the 21st Century, “Renewables 2020 global status report,” 2020. [Online]. Available: <https://www.ren21.net/gsr-2020/>
- [2] —, “Renewables 2019 global status report,” 2019. [Online]. Available: <https://www.ren21.net/gsr-2019/>
- [3] R. Teodorescu, M. Liserre *et al.*, “Grid converters for photovoltaic and wind power systems,” vol. 29, 2011.
- [4] S. B. Kjaer, J. K. Pedersen, and F. Blaabjerg, “A review of single-phase grid-connected inverters for photovoltaic modules,” *IEEE Transactions on Industry Applications*, vol. 41, no. 5, pp. 1292–1306, Sep 2005.
- [5] S. Kouro, J. I. Leon, D. Vinnikov, and L. G. Franquelo, “Grid-connected photovoltaic systems: An overview of recent research and emerging pv converter technology,” *IEEE Industrial Electronics Magazine*, vol. 9, no. 1, pp. 47–61, March 2015.
- [6] A. Gupta and A. S. Bais, “Solar microinverter and power optimizer market size by connectivity (standalone, on-grid), by application (residential, commercial, utility), industry analysis report, regional outlook, growth potential, price trends, competitive market share and forecast, 2016 – 2024,” 2017. [Online]. Available: <https://www.gminsights.com/industry-analysis/solar-microinverter-and-power-optimizer-market>
- [7] G. Zhu, S. Tan, Y. Chen, and C. K. Tse, “Mitigation of low-frequency current ripple in fuel-cell inverter systems through waveform control,” *IEEE Transactions on Power Electronics*, vol. 28, no. 2, pp. 779–792, Feb 2013.
- [8] M. Coppola, P. Guerriero, F. D. Napoli, S. Daliento, D. Lauria, and A. D. Pizzo, “A pv ac-module based on coupled-inductors boost dc/ac converter,” in *Power Electronics, Electrical Drives, Automation and Motion (SPEEDAM), 2014 International Symposium on*, June 2014, pp. 1015–1020.
- [9] Y. Fang and X. Ma, “A novel pv microinverter with coupled inductors and double-boost topology,” *IEEE Transactions on Power Electronics*, vol. 25, no. 12, pp. 3139–3147, Dec 2010.
- [10] S. Jain and V. Agarwal, “A single-stage grid connected inverter topology for solar pv systems with maximum power point tracking,” *IEEE Transactions on Power Electronics*, vol. 22, no. 5, pp. 1928–1940, Sept 2007.
- [11] C. N. M. Ho and K. K. M. Siu, “Manitoba inverter—single-phase single-stage buck-boost vsi topology,” *IEEE Transactions on Power Electronics*, vol. 34, no. 4, pp. 3445–3456, April 2019.
- [12] N. Kasa, T. Iida, and L. Chen, “Flyback inverter controlled by sensorless current mppt for photovoltaic power system,” *IEEE Transactions on Industrial Electronics*, vol. 52, no. 4, pp. 1145–1152, Aug 2005.
- [13] M. Jang and V. G. Agelidis, “A minimum power-processing-stage fuel-cell energy system based on a boost-inverter with a bidirectional backup battery storage,” *IEEE Transactions on Power Electronics*, vol. 26, no. 5, pp. 1568–1577, May 2011.

- [14] P. Sanchis, A. Ursaea, E. Gubia, and L. Marroyo, "Boost dc-ac inverter: a new control strategy," *IEEE Transactions on Power Electronics*, vol. 20, no. 2, pp. 343–353, March 2005.
- [15] D. B. W. Abeywardana, B. Hredzak, and V. G. Agelidis, "A rule-based controller to mitigate dc-side second-order harmonic current in a single-phase boost inverter," *IEEE Transactions on Power Electronics*, vol. 31, no. 2, pp. 1665–1679, Feb 2016.
- [16] D. B. W. Abeywardana, B. Hredzak, and V. G. Agelidis, "An input current feedback method to mitigate the dc-side low-frequency ripple current in a single-phase boost inverter," *IEEE Transactions on Power Electronics*, vol. 31, no. 6, pp. 4594–4603, 2016.
- [17] R. Caceres and I. Barbi, "A boost dc-ac converter: operation, analysis, control and experimentation," in *Proceedings of IECON '95 - 21st Annual Conference on IEEE Industrial Electronics*, vol. 1, Nov 1995, pp. 546–551 vol.1.
- [18] D. Cortes, N. Vazquez, and J. Alvarez-Gallegos, "Dynamical sliding-mode control of the boost inverter," *IEEE Transactions on Industrial Electronics*, vol. 56, no. 9, pp. 3467–3476, Sept 2009.
- [19] M. Jang, M. Ciobotaru, and V. G. Agelidis, "A single-phase grid-connected fuel cell system based on a boost-inverter," *IEEE Transactions on Power Electronics*, vol. 28, no. 1, pp. 279–288, Jan 2013.
- [20] Y. Liu, M. Huang, J. Sun, and X. Zha, "Active power decoupling method for isolated micro-inverters," in *2014 International Power Electronics and Application Conference and Exposition*, Nov 2014, pp. 1222–1225.
- [21] S. B. Kjaer and F. Blaabjerg, "A novel single-stage inverter for the ac-module with reduced low-frequency ripple penetration," *Proceed. of Epe'2003, Toulouse, France, 2-4 September*, 2003.
- [22] S. K. Mazumder and S. Mehrnami, "A low-device-count single-stage direct-power-conversion solar microinverter for microgrid," in *2012 3rd IEEE International Symposium on Power Electronics for Distributed Generation Systems (PEDG)*, June 2012, pp. 725–730.
- [23] S. Mehrnami and S. K. Mazumder, "Modulation scheme of the differential-mode Ćuk inverter for loss mitigation," in *2013 IEEE Energy Conversion Congress and Exposition*, 2013, pp. 3419–3425.
- [24] —, "Discontinuous modulation scheme for a differential-mode Ćuk inverter," *IEEE Transactions on Power Electronics*, vol. 30, no. 3, pp. 1242–1254, March 2015.
- [25] A. C. Nanakos, G. C. Christidis, and E. C. Tatakis, "Weighted efficiency optimization of flyback microinverter under improved boundary conduction mode (i-bcm)," *IEEE Transactions on Power Electronics*, vol. 30, no. 10, pp. 5548–5564, Oct 2015.
- [26] G. C. Christidis, A. C. Nanakos, and E. C. Tatakis, "Hybrid discontinuous/boundary conduction mode of flyback microinverter for ac -pv modules," *IEEE Transactions on Power Electronics*, vol. 31, no. 6, pp. 4195–4205, June 2016.
- [27] Feel-Soon Kang, Cheul-U Kim, Sung-Jun Park, and Han-Woong Park, "Interface circuit for photovoltaic system based on buck-boost current-source pwm inverter," in *IEEE 2002 28th Annual Conference of the Industrial Electronics Society. IECON 02*, vol. 4, Nov 2002, pp. 3257–3261 vol.4.
- [28] O. Abdel-Rahim, M. Orabi, and M. E. Ahmed, "High gain single-stage inverter for photovoltaic ac modules," in *Applied Power Electronics Conference and Exposition (APEC), 2011 Twenty-Sixth Annual IEEE*, March 2011, pp. 1961–1967.
- [29] Z. Zhao, M. Xu, Q. Chen, J. Lai, and Y. Cho, "Derivation of boost-buck converter based high-efficiency robust pv inverter," in *2010 IEEE Energy Conversion Congress and Exposition*, Sep. 2010, pp. 1479–1484.
- [30] —, "Derivation, analysis, and implementation of a boost-buck converter-based high-efficiency pv inverter," *IEEE Transactions on Power Electronics*, vol. 27, no. 3, pp. 1304–1313, March 2012.

- [31] P. K. Peter and V. Agarwal, "Photovoltaic module integrated standalone single stage switched capacitor inverter with maximum power point tracking," *IEEE Transactions on Power Electronics*, vol. PP, no. 99, pp. 1–1, 2016.
- [32] S. H. Lee, W. J. Cha, J. M. Kwon, and B. H. Kwon, "Control strategy of flyback microinverter with hybrid mode for pv ac modules," *IEEE Transactions on Industrial Electronics*, vol. 63, no. 2, pp. 995–1002, Feb 2016.
- [33] F. F. Edwin, W. Xiao, and V. Khadkikar, "Dynamic modeling and control of interleaved flyback module-integrated converter for pv power applications," *IEEE Transactions on Industrial Electronics*, vol. 61, no. 3, pp. 1377–1388, March 2014.
- [34] Y. Noh, B. Choi, S. Lee, J. Eom, and C. Won, "An optimal method to design a trap-cl filter for a pv ac-module based on flyback inverter," *IEEE Transactions on Industry Applications*, vol. 52, no. 2, pp. 1632–1641, March 2016.
- [35] Z. Zhang, X. F. He, and Y. F. Liu, "An optimal control method for photovoltaic grid-tied-interleaved flyback microinverters to achieve high efficiency in wide load range," *IEEE Transactions on Power Electronics*, vol. 28, no. 11, pp. 5074–5087, Nov 2013.
- [36] J. R. Gazoli, M. G. Villalva, T. G. Siqueira, and E. Ruppert, "Micro-inverter for integrated grid-tie pv module using resonant controller," in *2012 IEEE Power and Energy Society General Meeting*, July 2012, pp. 1–8.
- [37] M. Joshi, E. Shoubaki, R. Amarín, B. Modick, and J. Enslin, "A high-efficiency resonant solar micro-inverter," in *Proceedings of the 2011 14th European Conference on Power Electronics and Applications*, Aug 2011, pp. 1–10.
- [38] C. Prapanavarat, M. Barnes, and N. Jenkins, "Investigation of the performance of a photovoltaic ac module," *IEE Proceedings - Generation, Transmission and Distribution*, vol. 149, no. 4, pp. 472–478, July 2002.
- [39] D. Meneses, O. García, P. Alou, J. A. Oliver, and J. A. Cobos, "Grid-connected forward microinverter with primary-parallel secondary-series transformer," *IEEE Transactions on Power Electronics*, vol. 30, no. 9, pp. 4819–4830, Sept 2015.
- [40] H. G. Cabral, P. F. S. R. de Faria, I. L. Guisso, C. E. B. Rambo, B. L. Vigna, M. S. Santos, V. A. Vieira, R. C. Viero, and F. S. dos Reis, "A pv module-integrated inverter using a cuk converter in dcm with island detection scheme," in *2015 IEEE 13th Brazilian Power Electronics Conference and 1st Southern Power Electronics Conference (COBEP/SPEC)*, Nov 2015, pp. 1–6.
- [41] I. L. Guisso, H. F. M. Lopez, G. R. Pedrollo, and F. S. dos Reis, "Anti-islanding applied on a single-stage microinverter based on zeta converter for distributed microgeneration," in *IECON 2014 - 40th Annual Conference of the IEEE Industrial Electronics Society*, Oct 2014, pp. 5475–5481.
- [42] W. Li and X. He, "Review of nonisolated high-step-up dc/dc converters in photovoltaic grid-connected applications," *IEEE Transactions on Industrial Electronics*, vol. 58, no. 4, pp. 1239–1250, April 2011.
- [43] H. Liu, H. Hu, H. Wu, Y. Xing, and I. Batarseh, "Overview of high-step-up coupled-inductor boost converters," *IEEE Journal of Emerging and Selected Topics in Power Electronics*, vol. 4, no. 2, pp. 689–704, June 2016.
- [44] S. Chen, T. Liang, L. Yang, and J. Chen, "A safety enhanced, high step-up dc–dc converter for ac photovoltaic module application," *IEEE Transactions on Power Electronics*, vol. 27, no. 4, pp. 1809–1817, April 2012.
- [45] M. Das and V. Agarwal, "Design and analysis of a high-efficiency dc–dc converter with soft switching capability for renewable energy applications requiring high voltage gain," *IEEE Transactions on Industrial Electronics*, vol. 63, no. 5, pp. 2936–2944, May 2016.

- [46] W. Lai, S. Chen, T. Liang, K. Lee, and A. Ioinovici, "Design and implementation of grid connection photovoltaic micro inverter," in *2012 IEEE Energy Conversion Congress and Exposition (ECCE)*, Sep. 2012, pp. 2426–2432.
- [47] D. C. Martins and R. Demonti, "Photovoltaic energy processing for utility connected system," in *IECON'01. 27th Annual Conference of the IEEE Industrial Electronics Society (Cat. No.37243)*, vol. 2, Nov 2001, pp. 1292–1296 vol.2.
- [48] W.-J. Cha, J.-M. Kwon, and B.-H. Kwon, "Highly efficient step-up dc–dc converter for photovoltaic micro-inverter," *Solar Energy*, vol. 135, pp. 14–21, 2016.
- [49] J.-M. Kwon, B.-H. Kwon, and K.-H. Nam, "High-efficiency module-integrated photovoltaic power conditioning system," *IET Power Electronics*, vol. 2, no. 4, pp. 410–420, 2009.
- [50] W.-Y. Choi and J.-S. J. Lai, "High-efficiency grid-connected photovoltaic module integrated converter system with high-speed communication interfaces for small-scale distribution power generation," *Solar Energy*, vol. 84, no. 4, pp. 636 – 649, 2010, international Conference {CISBAT} 2007. [Online]. Available: <http://www.sciencedirect.com/science/article/pii/S0038092X10000162>
- [51] D. Cao, S. Jiang, F. Z. Peng, and Y. Li, "Low cost transformer isolated boost half-bridge micro-inverter for single-phase grid-connected photovoltaic system," in *2012 Twenty-Seventh Annual IEEE Applied Power Electronics Conference and Exposition (APEC)*, Feb 2012, pp. 71–78.
- [52] S. Jiang, D. Cao, Y. Li, and F. Z. Peng, "Grid-connected boost-half-bridge photovoltaic microinverter system using repetitive current control and maximum power point tracking," *IEEE Transactions on Power Electronics*, vol. 27, no. 11, pp. 4711–4722, Nov 2012.
- [53] L. A. Garcia-Rodriguez, C. Deng, J. C. Balda, and A. Escobar-Mejía, "Analysis, modeling and control of an interleaved isolated boost series resonant converter for microinverter applications," in *2016 IEEE Applied Power Electronics Conference and Exposition (APEC)*, March 2016, pp. 362–369.
- [54] C. Li, C. Yang, Y. Chang, H. Chiu, Y. Lo, C. Chuang, S. Cheng, M. Kuo, Y. Huang, Y. Jean, and Y. Huang, "A module-integrated isolated solar micro-inverter without electrolytic capacitors," in *2012 International Conference on Audio, Language and Image Processing*, July 2012, pp. 247–253.
- [55] Q. Zhang, C. Hu, L. Chen, A. Amirahmadi, N. Kutkut, Z. J. Shen, and I. Batarseh, "A center point iteration mppt method with application on the frequency-modulated llc microinverter," *IEEE Transactions on Power Electronics*, vol. 29, no. 3, pp. 1262–1274, March 2014.
- [56] T. LaBella, W. Yu, J. S. . Lai, M. Senesky, and D. Anderson, "A bidirectional-switch-based wide-input range high-efficiency isolated resonant converter for photovoltaic applications," *IEEE Transactions on Power Electronics*, vol. 29, no. 7, pp. 3473–3484, July 2014.
- [57] Y. H. Kim, S. C. Shin, J. H. Lee, Y. C. Jung, and C. Y. Won, "Soft-switching current-fed push-pull converter for 250-w ac module applications," *IEEE Transactions on Power Electronics*, vol. 29, no. 2, pp. 863–872, Feb 2014.
- [58] D. Vinnikov, A. Chub, E. Liivik, and I. Roasto, "High-performance quasi-z-source series resonant dc–dc converter for photovoltaic module-level power electronics applications," *IEEE Transactions on Power Electronics*, vol. 32, no. 5, pp. 3634–3650, May 2017.
- [59] D. Vinnikov, A. Chub, E. Liivik, R. Kosenko, and O. Korkh, "Solar optiverter—a novel hybrid approach to the photovoltaic module level power electronics," *IEEE Transactions on Industrial Electronics*, vol. 66, no. 5, pp. 3869–3880, May 2019.
- [60] C. Rodriguez and G. A. J. Amaratunga, "Long-lifetime power inverter for photovoltaic ac modules," *IEEE Transactions on Industrial Electronics*, vol. 55, no. 7, pp. 2593–2601, July 2008.
- [61] D. C. Martins and R. Demonti, "Interconnection of a photovoltaic panels array to a single-phase utility line from a static conversion system," in *2000 IEEE 31st Annual Power Electronics*

- Specialists Conference. Conference Proceedings (Cat. No.00CH37018)*, vol. 3, June 2000, pp. 1207–1211 vol.3.
- [62] R. O. Caceres and I. Barbi, “A boost dc-ac converter: analysis, design, and experimentation,” *IEEE Transactions on Power Electronics*, vol. 14, no. 1, pp. 134–141, Jan 1999.
 - [63] K. Jha, S. Mishra, and A. Joshi, “High-quality sine wave generation using a differential boost inverter at higher operating frequency,” *IEEE Transactions on Industry Applications*, vol. 51, no. 1, pp. 373–384, Jan 2015.
 - [64] H. Renaudineau, D. Lopez, F. Flores-Bahamonde, and S. Kouro, “Flatness-based control of a boost inverter for pv microinverter application,” in *2017 IEEE 8th International Symposium on Power Electronics for Distributed Generation Systems (PEDG)*, April 2017, pp. 1–6.
 - [65] D. Lopez, F. Flores-Bahamonde, S. Kouro, M. A. Perez, A. Llor, and L. Martínez-Salamero, “Predictive control of a single-stage boost dc-ac photovoltaic microinverter,” in *IECON 2016 - 42nd Annual Conference of the IEEE Industrial Electronics Society*, Oct 2016, pp. 6746–6751.
 - [66] F. Flores-Bahamonde, H. Valderrama-Blavi, J. M. Bosque-Moncusi, G. García, and L. Martínez-Salamero, “Using the sliding-mode control approach for analysis and design of the boost inverter,” *IET Power Electronics*, vol. 9, no. 8, pp. 1625–1634, 2016.
 - [67] R. P. Aguilera, P. Acuna, G. Konstantinou, S. Vazquez, and J. I. Leon, “Basic control principles in power electronics: Analog and digital control design,” in *Control of Power Electronic Converters and Systems*. Elsevier, 2018, pp. 31–68.
 - [68] S. Kouro, B. Wu, H. Abu-Rub, and F. Blaabjerg, “Photovoltaic energy conversion systems,” *Power Electronics for Renewable Energy Systems, Transportation and Industrial Applications*, pp. 160–198, 2014.
 - [69] B. Bouneb, D. M. Grant, A. Cruden, and J. R. McDonald, “Grid connected inverter suitable for economic residential fuel cell operation,” in *2005 European Conference on Power Electronics and Applications*, 2005, pp. 10 pp.–P.10.
 - [70] P. Sanchis Gorpide, O. Alonso Sadaba, L. Marroyo Palomo, T. Meynard, and E. Lefeuvre, “A new control strategy for the boost dc-ac inverter,” in *2001 IEEE 32nd Annual Power Electronics Specialists Conference (IEEE Cat. No.01CH37230)*, vol. 2, 2001, pp. 974–979 vol.2.
 - [71] S. Kouro, P. Cortes, R. Vargas, U. Ammann, and J. Rodriguez, “Model predictive control; a simple and powerful method to control power converters,” *IEEE Transactions on Industrial Electronics*, vol. 56, no. 6, pp. 1826–1838, June 2009.
 - [72] P. Cortes, S. Kouro, B. L. Rocca, R. Vargas, J. Rodriguez, J. I. Leon, S. Vazquez, and L. G. Franquelo, “Guidelines for weighting factors design in model predictive control of power converters and drives,” in *Industrial Technology, 2009. ICIT 2009. IEEE International Conference on*, Feb 2009, pp. 1–7.
 - [73] M. Fliess, J. Lévine, P. Martin, F. Ollivier, and P. Rouchon, “Controlling nonlinear systems by flatness,” in *Systems and Control in the Twenty-first Century*. Springer, 1997, pp. 137–154.
 - [74] H. Renaudineau, “Hybrid renewable energy sourced system: Energy management & self-diagnosis,” Ph.D. dissertation, Université de Lorraine, 2013.
 - [75] M. Soheil-Hamedani, M. Zandi, R. Gavagsaz-Ghoachani, B. Nahid-Mobarakeh, and S. Pierfederici, “Flatness-based control method: A review of its applications to power systems,” in *2016 7th Power Electronics and Drive Systems Technologies Conference (PEDSTC)*, Feb 2016, pp. 547–552.
 - [76] J. Levine, *Analysis and control of nonlinear systems: A flatness-based approach*. Springer Science & Business Media, 2009.
 - [77] M. Fliess, J. Lévine, P. Martin, and P. Rouchon, “Flatness and defect of non-linear systems: introductory theory and examples,” *International journal of control*, vol. 61, no. 6, pp. 1327–1361, 1995.

- [78] A. Gensior, O. Woywode, J. Rudolph, and H. Guldner, "On differential flatness, trajectory planning, observers, and stabilization for dc-dc converters," *IEEE Transactions on Circuits and Systems I: Regular Papers*, vol. 53, no. 9, pp. 2000–2010, Sep. 2006.
- [79] G. C. Goodwin, S. F. Graebe, M. E. Salgado *et al.*, *Control system design*. Upper Saddle River, NJ: Prentice Hall,, 2001.
- [80] T. L. Skvarenina, *The power electronics handbook*. CRC press, 2002.
- [81] C. Vecchio *et al.*, "Sliding mode control: theoretical developments and applications to uncertain mechanical systems." 2008.
- [82] L. Martinez Salamero, A. Cid-Pastor, A. El Aroudi, R. Giral, and J. Calvente, "Modelado y control de convertidores conmutados continua-continua: Una perspectiva tutorial," *Revista Iberoamericana de Automática e Informática Industrial RIAI*, vol. 6, no. 4, pp. 5–20, 2009.
- [83] P. Rodríguez, A. Luna, R. S. Muñoz-Aguilar, I. Etxeberria-Otadui, R. Teodorescu, and F. Blaabjerg, "A stationary reference frame grid synchronization system for three-phase grid-connected power converters under adverse grid conditions," *IEEE Transactions on Power Electronics*, vol. 27, no. 1, pp. 99–112, Jan 2012.
- [84] R. Teodorescu, F. Blaabjerg, M. Liserre, and P. C. Loh, "Proportional-resonant controllers and filters for grid-connected voltage-source converters," *IEE Proceedings - Electric Power Applications*, vol. 153, no. 5, pp. 750–762, Sep. 2006.
- [85] M. Kazimierczuk, *Pulse-width Modulated DC-DC Power Converters*. Wiley, 2008. [Online]. Available: https://books.google.cl/books?id=H_FwBkSpYY0C
- [86] L. Corradini, D. Maksimovic, P. Mattavelli, and R. Zane, *Digital Control of High-Frequency Switched-Mode Power Converters*, ser. IEEE Press Series on Power Engineering. Wiley, 2015. [Online]. Available: <https://books.google.cl/books?id=FMfCCQAAQBAJ>
- [87] P. Karamanakos and T. Geyer, "Guidelines for the design of finite control set model predictive controllers," *IEEE Transactions on Power Electronics*, vol. 35, no. 7, pp. 7434–7450, 2020.
- [88] SunPower, "Datasheet of spr-x21-335," 2016. [Online]. Available: <https://us.sunpower.com/products/solar-panels>
- [89] Panasonic, "Datasheet of n330," 2020. [Online]. Available: <https://na.panasonic.com/us/energy-solutions/solar/hit-panels>
- [90] F. Solar, "Datasheet of fs-41020a-3," 2018. [Online]. Available: <http://www.firstsolar.com/Resources/Technical-Documents>
- [91] dSPACE, "Datasheet of microlabbox." [Online]. Available: <https://www.dspace.com/en/inc/home/products/hw/microlabbox.cfm>